Passive and Active two-dimensional Photonic Crystal Components

Iwan Lukas Märki

Université de Neuchâtel

Institut de Microtechnique

Passive and active two-dimensional photonic crystal components

Thèse

Présentée à la faculté des sciences
pour obtenir le grade de docteur ès science
par

Iwan Märki

Neuchâtel, 30 juin 2006

Université de Neuchâtel unine

FACULTE DES SCIENCES
Secrétariat-Décanat de la faculté
- Rue Emile-Argand 11
- CP 158
- CH-2009 Neuchâtel

IMPRIMATUR POUR LA THESE

Passive and active two dimensional photonic crystal components

Iwan MAERKI

UNIVERSITE DE NEUCHATEL

FACULTE DES SCIENCES

La Faculté des sciences de l'Université de Neuchâtel,
sur le rapport des membres du jury

MM. H.P. Herzig (directeur de thèse, IMT-UniNE), U. Staufer (IMT-UniNE),
R. Houdré (EPF-Lausanne), Th. Krauss (University-St-Andrews, UK)
et M. Salt (Heptagon-Rüschlikon)

autorise l'impression de la présente thèse.

Neuchâtel, le 30 novembre 2006

Le doyen :
J.-P. Derendinger

UNIVERSITE DE NEUCHATEL
FACULTE DES SCIENCES
Secrétariat-décanat de la faculté
Rue Emile-Argand 11 - CP 158
CH-2009 Neuchâtel

The finest thing we can experience is the mysterious. It is the fundamental emotion which stands at the cradle of true art and true science. He who does not know it and can no longer wonder, no longer feel amazement, is as good as dead, a snuffed-out candle.

Albert Einstein

Abstract

Photonic crystals are periodic dielectric structures having periodicity of the order of the wavelength. Consequently, they offer the ability to control the propagation of electromagnetic waves in a similar way as the periodic potential affects the electron motion in a semiconductor crystal. By choosing the parameters of the photonic crystal, desired dispersion characteristics such as band gaps for light can be implemented, providing the possibility of creating miniaturized photonic components for integrated optical circuits. In this thesis, two-dimensional photonic crystal components with passive and active functionalities are designed, realized and investigated.

The passive components, including photonic crystal cavities, waveguides and tight waveguide bends, are studied by means of far-field and near-field (heterodyne SNOM) measurement techniques addressing loss, quality factors and transmission efficiencies. The ability to tune or modulate the optical properties of photonic crystal devices increases their functionality and opens up new possibilities for applications. We present two ways of perturbing the optical environment near a photonic crystal cavity, enabling tuning and modulation of the in-plane transmission. Optical switching and wavelength tuning is obtained by means of induced thermal and plasma dispersion effects when focusing a laser onto a photonic crystal cavity structure, demonstrating the feasibility of high-speed optical integrated circuits based on silicon structures. On the other hand, tuning of the resonant wavelength and on-off switching of the transmission signal is achieved by probing the optical field confined within the resonant cavity by means of an atomic force microscope (AFM) tip, suggesting an integrated on-off switch or tunable filter.

This thesis combines design, fabrication and measurement, thus bringing a better understanding of the fundamental properties of these types of photonic crystals, and helping to pave the way to practical integrated optical circuits.

Contents

Part I

Overview

1 Introduction

During the 20^{th} century, the development of semiconductor technology has brought about enormous changes to our society and the life of people. The constant trend towards smaller, faster integrated electronic circuits is derived from the development of technologies that allows us to control the flow of electrons in a semiconductor. During the 21^{st} century, there is a possibility that photonic devices may take over the role of electronic devices. Through the use of surprisingly similar theoretical and fabrication approaches, photonic crystals promise to give us control over the flow of photons, and with their ability to interact with light on a wavelength scale they have the potential to provide the means for true photonic integration. By designing and controlling the optical properties of materials, photonic crystals may become key components for devices with functionalities such as all-optical switching, extracting light to useful radiation, boosting the efficiency and brightness of LEDs, preventing photon emission into certain optical modes for low threshold microcavity lasers, and waveguiding beyond the limits of total internal reflection for highly compact systems containing tight bends and splitters for light signal transfer. In order to realize these devices, we need to understand the fundamental properties of photonic crystals with their limiting factors such as propagation losses and we need to be capable of fabricating them with today's technology.

Photonic crystals arise from the cooperation of periodic scatterers, therefore they are called "crystals" because of their periodicity and "photonic" because they interact with light. Electromagnetic waves propagating in one-dimensional periodic structures, such as a multilayer film, were first studied by Lord Rayleigh in 1887. He showed that any such periodic system has a narrow band gap prohibiting light propagation through the planes [1]. This band gap is angle-dependent, producing a reflected colour that varies with angle. A similar effect is often responsible for the many iridescent colours found in nature, such as the wings of certain butterflies and moths that are covered with periodic microscopic structures [2]. Only at the end of the 1980's, when both Yablonovitch and John suggested that three-dimensional structures with periodic variations in dielectric constant could influence the nature of photonic modes in a material, did the concept of photonic crystals start to emerge. Yablonovitch's main aim was to control the radiative properties of materials [3], while John's was to affect photonic localization by introducing a random refractive-index variation in a periodic medium [4]. John also predicted many interesting quantum optical phenomena that can be realized in photonic crystals such as the bound state of photons [5] and non-exponential decay of spontaneous emission [6]. The first three-dimensional photonic crystal exhibiting a photonic band gap in the microwave range was fabricated in the beginning of the 90's [7]. This structure, consisting of a dielectric medium drilled along three of the axes of the diamond lattice, has been named Yablonovite. At the end of the 1990's, the first three-dimensional photonic band gap structure in the infrared (optical communication wavelengths) was realized with the woodpile structure, consisting of tiny rods of silicon built up in a layer by layer manner [8, 9]. At the present time, three main fabrication methods are used to create three-dimensional photonic crystal structures. First, layer-by-layer fabrication where individual crystal layers are deposited one-by-one and etched with a two-dimensional pattern via lithographic methods [10]. Second, colloidal self-assembly, in which small dielectric spheres in a fluid arrange themselves into crystals by surface forces [11]. Third, holographic lithography, in which three-dimensional crystals can be formed by the interference pattern of four to six coherent laser beams hardening a light-sensitive resin [12]. Even though several different fabrication technologies are available, they all share some undesirable properties: all are highly sensitive to the fabrication environment, all tend to be somewhat slow and all require significant investment in equipment and resources. The accurate, rapid and reliable fabrication of three-dimensional periodic structures with submicrometer sized features has remained a difficult challenge. In terms of structure types, there is a stage between the one-dimensional multilayer film and the full three-dimensional photonic crystal. Many research groups, including ours, have concentrated their efforts on two-dimensional photonic crystals, which has led to considerable progress in both design and fabrication [13–15]. The fabrication of such planar structures is based on well-known lithographic techniques used to manufacture integrated electronic circuits. A summary of early studies can be found in Refs. [16, 17]. These two-dimensional photonic crystals have many things in common with both the one- and three-dimensional versions, but with the bonus of surprising flexibility of design and (compared to the three-dimensional version) easier fabrication. It is therefore not surprising that a great many of the practical advances in photonic crystal research have been made using the two-dimensional approach.

In this thesis, two-dimensional photonic crystal components with passive and active functionalities are designed, realized and investigated. This thesis combines design, fabrication and measurement, thus bringing a better understanding of the fundamental properties of these types of photonic crystals, and helping to pave the way to practical integrated optical circuits.

Chapter 2 gives a theoretical introduction to the properties of photonic crystals starting with Maxwell's equations. These equations are cast as a linear Hermitian eigenvalue problem, a form in which many useful properties become apparent. The photonic crystal properties are then described by the characteristic photonic band structure or dispersion diagram representing the eigensolutions of the eigenvalue problem for a periodic dielectric structure. In addition, the formation of different types of localized modes by introducing defects into the photonic crystal are discussed. The theoretical overview mainly focuses on two-dimensional photonic crystals in anticipation of the results presented thereafter.

Chapter 3 presents the basic concepts of the two numerical simulation techniques used for the design of the photonic crystal waveguides and microcavities: a frequency domain method based on planewave expansion computing fully-vectorial eigenmodes of Maxwell's equations and a time domain method based on the finite integration time domain algorithm.

The photonic crystal structures presented in this work have been fabricated by the two most commonly used lithography techniques, which are described in Chapter 4. On the one hand, e-beam lithography with its high resolution and flexibility is a powerful fabrication tool for realizing structure with submicrometer features. On the other hand, deep UV-lithography is resolution limited but provides a fabrication process more suited for large-scale production.

Chapter 5 gives a brief survey of published research on passive and active two-dimensional photonic crystal components.

Chapter 6 contains the results of this work, which are presented in eight publications. The first three publications (I-III) present the experimental and theoretical characterization of silicon photonic crystal waveguides and microcavities fabricated by e-beam lithography and deep UV-lithography. Based on a stage-by-stage analysis using an incremented series of different samples, coupling efficiencies between a conventional ridge waveguide and a photonic crystal waveguide as well as the bending efficiency around a 90° corner and the quality factor and losses in a microcavity are investigated and quantified. In addition to these far-field measurements, publications IV and V present some of the first observations of the amplitude and phase of the optical field propagating in straight and 90° bend photonic crystal waveguides by means of heterodyne scanning near-field optical microscopy (SNOM). These first publications contribute to a better understanding of the fundamental properties and limitations of passive two-dimensional photonic crystals and illustrate the usefulness of the different measurement techniques. Publications VI and VII report two tuning and switching methods of microcavities in silicon photonic crystal waveguides. All-optical tuning and switching is achieved by focusing a laser on the microcavity region, generating both a thermal and a plasma dispersion effect, which allow the tuning and fast modulation of the in-plane transmission. Tuning and on-off switching of the transmission signal are likewise achieved by means of a silicon AFM tip, probing the highly localized field in the vicinity of the microcavity. These two publications on active photonic crystal components contribute most strongly to the steps towards practical applications suggesting miniaturized integrated devices with active functionalities. Although publication VIII addresses a different subject, being part of the author's work during his PhD thesis, it is included here for completeness. It presents results on a different topic discussing optical phase singularities at subwavelength resolution generated by subwavelength structures, such as gratings and microlenses. These measurements were performed by means of a heterodyne scanning probe microscope and a high resolution interference microscope.

Finally, a short conclusion is given in chapter 7.

2 Photonic crystals

Advances in semiconductor physics have allowed the control of the conducting properties of materials, thereby initiating the transistor revolution in electronics. This led to the great impact that semiconductor materials have had on every sector of society. Today, photonic crystals promise to give us similar control over the optical properties of materials. In order to introduce the basic concept of photonic crystals, it is useful to draw analogies with semiconductor physics.

In a semiconductor, the atoms are arranged in a periodic crystal lattice, and electrons moving through this crystal experience a periodic potential as they interact with the atoms. This interaction results in the formation of allowed and forbidden energy states (allowed bands and band gaps). If the periodicity of the lattice is broken by a missing atom or by an impurity atom, or if the material contains interstitial impurities, an electron can have an energy state within the electronic band gap [18].

In a photonic crystal, the periodic potential is due to a periodic arrangement of macroscopic dielectric media instead of atoms. The scale of the alternating regions with different dielectric constants is on the order of the wavelength of light. As light propagates within the periodic material the contrast in the dielectric constant acts as the periodic potential. This interaction results in the formation of allowed and forbidden energy states (light modes) as in electronic materials. If the periodicity of the photonic crystal is broken by introducing defects in the periodic structure, light can have energy states (defect modes) within the photonic band gap (frequency range where light cannot propagate within the photonic crystal) . Photonic crystals can be differentiated between one-dimensional (1D), two-dimensional (2D), and three-dimensional (3D) crystals according to the dimensionality of their periodic structure (schematically depicted in Fig.1). In addition, two-dimensional structures with a finite thickness combine photonic-crystal effects in the plane of periodicity with conventional index guiding in the third dimension.

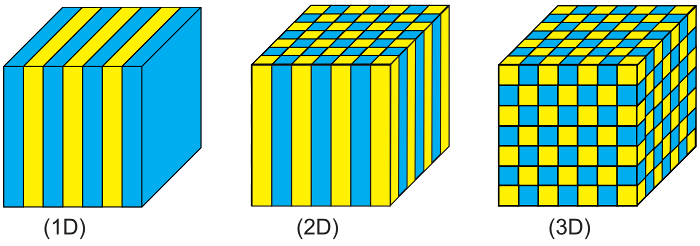

Figure 1: Schematic illustration of one-dimensional (1D), two-dimensional (2D), and three-dimensional (3D) photonic crystals. The different grays represent materials with different dielectric constants.

The exciting potential of photonic crystals lies in the ability to control the optical properties of materials and to mould the flow of light. The concept of photonic crystals has led to many subsequent developments in fabrication, theory, and application, from integrated optics to negative refraction to optical fibers that guide light in air.

2.1 Wave equations and eigenvalue problem

The understanding of the interaction of light with periodic dielectric materials allows the design of the optical properties of photonic crystals. For this purpose, we must turn to the Maxwell equations, which describe the interaction of light with matter:

$$\nabla \mathbf{B}(\mathbf{r},t) = 0 \qquad \nabla \times \mathbf{E}(\mathbf{r},t) + \frac{1}{c}\frac{\partial \mathbf{B}(\mathbf{r},t)}{\partial t} = 0$$

$$\nabla \mathbf{E}(\mathbf{r},t) = 4\pi\rho(\mathbf{r},t) \qquad \nabla \times \mathbf{B}(\mathbf{r},t) - \frac{1}{c}\frac{\partial \mathbf{E}(\mathbf{r},t)}{\partial t} = \frac{4\pi}{c}\mathbf{J}(\mathbf{r},t). \tag{1}$$

E and **H** are the macroscopic electric and magnetic fields, **D** and **B** are the displacement and magnetic induction fields, and ρ and **J** are the free charge and current densities. In order to simplify the Maxwell equations (Eq. 1), we will restrict ourselves to propagation within a composite of regions of different homogenous dielectric materials with no free electric charges and no electric currents. Therefore, we can set $\rho = 0$, $\mathbf{J} = 0$. Further, in order to relate **D** to **E** and **B** to **H** we make the following assumptions: we consider only small field strengths so that we are in the linear regime; we ignore the frequency dependence of the dielectric constant; we assume the dielectric material to be macroscopic, isotropic and lossless. Thus, the Maxwell equations are reduced to

$$\nabla \mathbf{H}(\mathbf{r},t) = 0 \qquad \nabla \times \mathbf{E}(\mathbf{r},t) + \frac{1}{c}\frac{\partial \mathbf{H}(\mathbf{r},t)}{\partial t} = 0$$

$$\nabla \varepsilon(\mathbf{r},t)\mathbf{E}(\mathbf{r},t) = 0 \qquad \nabla \times \mathbf{H}(\mathbf{r},t) - \frac{1}{c}\frac{\varepsilon(\mathbf{r},t)\partial \mathbf{E}(\mathbf{r},t)}{\partial t} = 0. \tag{2}$$

By expanding the fields E and H into harmonic (sinusoidal) modes, the time dependence can be separated out and the two curl equations relating E and H can be combined into an equation entirely in H(r) [17]:

$$\nabla \times \left(\frac{1}{\varepsilon(\mathbf{r})}\nabla \times \mathbf{H}(\mathbf{r})\right) = \left(\frac{\omega}{c}\right)^2 \mathbf{H}(\mathbf{r}). \tag{3}$$

The content of equation (3) states that if $\mathbf{H}(\mathbf{r})$ is an allowable electromagnetic mode, the result after the operations of the equation will just be a constant times the original function $\mathbf{H}(\mathbf{r})$. This is an eigenvalue problem, of which $\mathbf{H}(\mathbf{r})$ is the eigenvector and $(\omega/c)^2$ is the eigenvalue with ω as the angular frequency. The eigenvectors $\mathbf{H}(\mathbf{r})$ are the field patterns of the harmonic modes in the dielectric material, and the eigenvalues $(\omega/c)^2$ are proportional to the squared frequencies of these modes. Further, it can be shown that the operator $\Pi = \nabla \times \left(\frac{1}{\varepsilon(\mathbf{r})} \nabla \times\right)$ is linear and Hermitian [17]. A Hermitian operator implies that the eigenfunctions (modes of different energies) are orthogonal and have real eigenvalues. If two harmonic modes have equal frequencies ($\omega_1 = \omega_2$), then we say they are degenerate and not necessarily orthogonal. An important property of the electromagnetic modes is that there is no specified length scale involved. Once the eigenvalues and eigenfunctions of equation (3) are solved, they can be scaled to any physical size or wavelength range as long as the dielectric constant is fixed. Due to the scalability, photonic crystal components can be designed without specifying the dimensions and subsequently scaled to the selected frequency regime. In reality, some slight adjustment might be needed to compensate for differences in the dielectric constant at different frequencies.

2.2 Periodic dielectric structures

A photonic crystal has a discrete translational symmetry and is described by a periodic dielectric function $\varepsilon(\mathbf{r}) = \varepsilon(\mathbf{r} + \mathbf{R})$ where $\mathbf{R}$ is an integer multiple of the photonic crystal primitive lattice vector in each direction. Because ε is a periodic function of the spatial coordinate $\mathbf{r}$, the Bloch-Floquet theorem for periodic eigenproblems can be applied, which states that the solutions to Eq. (3) is of the form

$$\mathbf{H}(\mathbf{r}) = \mathbf{u}_{\mathbf{k}}(\mathbf{r}) e^{i(\mathbf{kr})}, \tag{4}$$

with eigenvalues of $\omega_n(\mathbf{k})$, where $\mathbf{u}_{\mathbf{k}}$ is a periodic envelope function on the lattice: $\mathbf{u}_{\mathbf{k}}(\mathbf{r}) = \mathbf{u}_{\mathbf{k}}(\mathbf{r} + \mathbf{R})$ for all lattice vectors $\mathbf{R}$. When Eq. (4) is substituted into Eq. (3), one gets

$$(i\mathbf{k} + \nabla) \times \left(\frac{1}{\varepsilon(\mathbf{r})} (i\mathbf{k} + \nabla) \times \mathbf{u}_{n,\mathbf{k}}(\mathbf{r}) \right) = \left(\frac{\omega(n, \mathbf{k})}{c} \right)^2 \mathbf{u}_{n,\mathbf{k}}(\mathbf{r}) \tag{5}$$

yielding a different Hermitian eigenproblem which is subject to the periodic boundary condition leading to eigenvectors $\mathbf{u}_{n,\mathbf{k}}(\mathbf{r})$ and eigenvalues $(\omega_n(\mathbf{k})/c)^2$. These eigenvalues are continuous functions of each Bloch wavevector $\mathbf{k}$, forming discrete bands, where n denotes the discrete eigenvalues. There are n solutions with frequencies $\omega_n(\mathbf{k})$ for every predetermined value of $\mathbf{k}$. The relations $\omega_n(\mathbf{k})$ as a function of $\mathbf{k}$ constitute the photonic band structure, mapping out all interactions between the modes in a photonic crystal. In other words, the photonic band structure or dispersion diagram supplies us with most of the information that we need to predict the optical properties of a photonic crystal.

Because of the periodic boundary condition, the eigensolutions (Bloch states) $\mathbf{u}_{\mathbf{k}}(\mathbf{r})$ are periodic functions of $\mathbf{k}$ as well, such as the solution $\mathbf{u}_{\mathbf{k}}(\mathbf{r})$ is the same as $\mathbf{u}_{\mathbf{k}+\mathbf{G}}(\mathbf{r})$, where $\mathbf{G}$ is a primitive reciprocal lattice vector defined by $\mathbf{R}i \cdot \mathbf{G}j = 2\pi\delta_{i,j}$. As a consequence, the eigenvalue problem can be regarded as being restricted to a single unit cell of the photonic crystal and we only need to compute the Bloch states for $\mathbf{k}$ within the primitive cell of the reciprocal lattice, which is called the Brillouin zone [18]. In addition, the Brillouin zone may itself have rotational symmetries in the lattice, which results in additional redundancies in the solutions within the Brillouin zone corresponding to the lattice symmetries. By eliminating the redundant regions within the Brillouin zone, we obtain a zone for which the $\omega_n(\mathbf{k})$ are not related by symmetry, namely the irreducible Brillouin zone.

In this thesis we primarily work with photonic crystals that are based on a square or triangular lattice. We show therefore a square and triangular lattice with its Brillouin and irreducible Brillouin zones in Fig.2. According to the rotational symmetries of the two lattice configurations, the irreducible zones are fractions of the area of the full Brillouin zone.

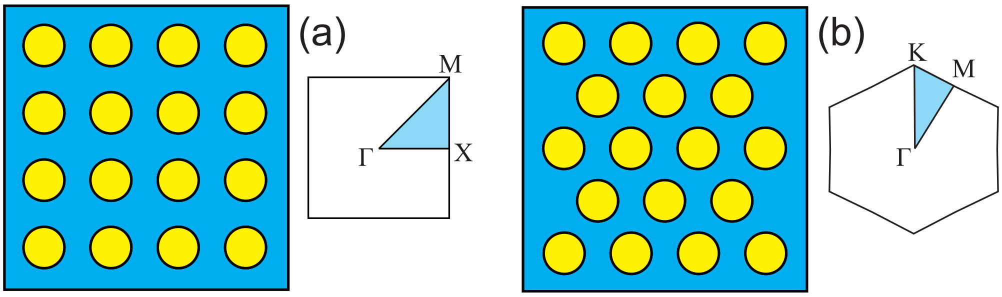

Figure 2: Square (a) and triangular (b) lattices with their respective Brillouin zones as well as their irreducible Brillouin zones of a two-dimensional photonic crystal. The special points at the center, corner, and face are conventionally known as Γ, M and X or Γ, M and K, respectively.

2.3 Photonic band structures

In this section we study the band structure of two-dimensional photonic crystals since this work is mainly focused on two-dimensional structures. A two-dimensional photonic crystal is periodic along two of its axes and homogeneous along the third. Two-dimensional systems exhibit most of the important characteristics of photonic crystals for light propagating in the plane of periodicity. The optical fields interacting with the photonic crystal structure can be divided into two polarizations: TM (transverse magnetic), in which the magnetic field is in the plane of periodicity and the electric field is perpendicular; and TE (transverse electric), in which the electric field is in the plane of periodicity and the magnetic field is perpendicular.

Figure 3 shows the photonic band structure or dispersion diagram with the eigensolutions for a triangular lattice of holes in a high refractive-index material. The hole radius is chosen to be $0.35a$, where a is the lattice constant and the high/low ε ratio is 12/1. Both the TE and the TM band structures are shown. The in-plane wavevector $\mathbf{k}_{//}$ goes along the edge of the irreducible Brillouin zone, from Γ to M to K as shown in the inset in Fig. 3. It is conventional to plot the frequency bands only along the boundaries of the irreducible Brillouin zone since the band extrema almost always occur along these boundaries [17]. With Maxwell's equations being scale-invariant, the frequencies ω are given in units of $2\pi c/a$, which is equivalent to a/λ (λ being the vacuum wavelength), so that the same solutions can be applied to any wavelength range by adapting the lattice constant a.

A first characteristic optical property of a photonic crystal is the photonic band gap. In a one-dimensional photonic crystal, such as a multilayer film, the photonic band gap prohibiting light propagation through the planes is the frequency range where Bragg reflection occurs. A two-dimensional triangular lattice with a hexagonal Brillouin zone exhibits a very high symmetry in the plane. Therefore, this structure is convenient for the formation of forbidden bands in all directions within the plane of periodicity. For TE modes (light gray lines in Fig.3) we observe a complete photonic band gap (light gray shaded region) between the first and the second bands, whereas for TM modes (dark gray lines in Fig.3) no photonic band gap exists. In order to understand in more detail the formation of a photonic band gap for TE modes, we look at the field patterns (magnetic field) at the lower and upper band edges corresponding to the high symmetry points K and M of the irreducible Brillouin zone. At the lower band edge, the field associated with the lowest TE mode at K is strongly concentrated in the high index material (Fig.3(c)) giving it a lower frequency. In contrast, the field pattern of the second mode at M, the upper band edge, has a nodal plane cutting through the high index material and therefore its energy is more concentrated in the air

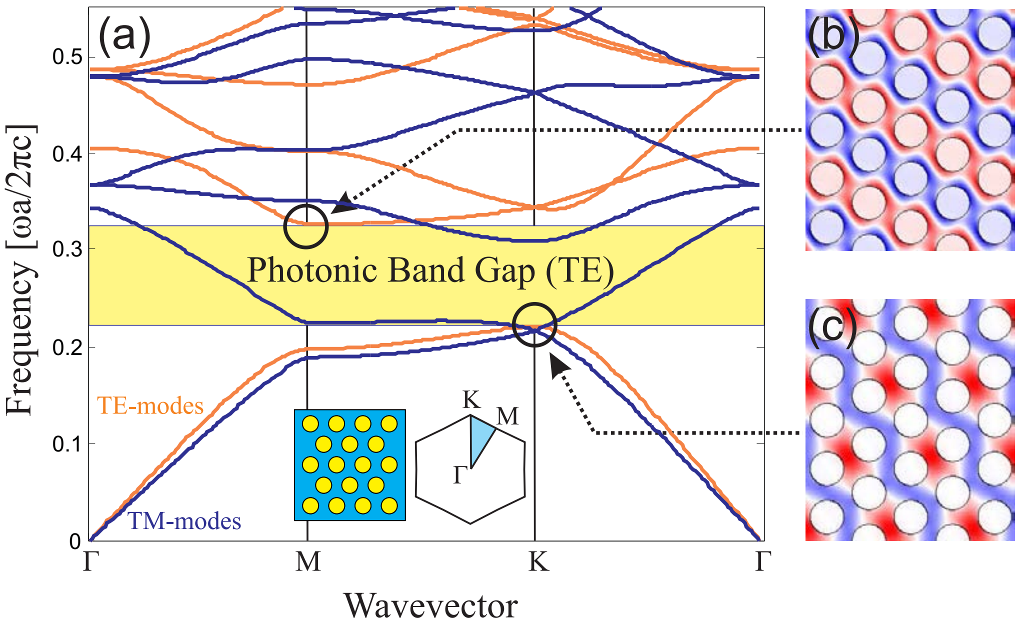

Figure 3: (a) The photonic band structure for a triangular lattice of air holes ($r/a = 0.35$) in a high index material ($\varepsilon = 12.0$), where a is the lattice constant (see inset). The frequencies for the two polarizations (TE-modes in light gray, TM-modes in dark gray) are plotted around the boundary of the irreducible Brillouin zone (shaded triangle in the inset). (b) The magnetic field pattern of the TE mode corresponding to the second band at the M point. (c) The magnetic field pattern of the TE mode corresponding to the first band at the K point. The gray levels indicates the amplitude of the magnetic field (dark = negative, light = positive). There is a band gap for the TE guided modes only.

holes (Fig.3(b)) giving it a higher frequency. For this reason, the bands above and below a photonic band gap are also referred to "air band" and "dielectric band", respectively. The photonic band gap arises from this difference in field energy distribution. The higher the dielectric contrast in the periodic structure the larger is the photonic band gap. Therefore, high index materials are essential for the realization of photonic crystal structures.

Besides the photonic band gap, we observe other optical properties specific to photonic crystals in the dispersion diagram. The dispersion properties of light propagating within the photonic crystal are described by the allowed bands (light gray and dark gray lines) for the TE and TM polarization. Light with an angular frequency centered at ω and a wavevector $\mathbf{k}_0$ travels with a group velocity $\nu_g = \mathbf{grad}_{\mathbf{k}=\mathbf{k_0}}\omega$ in the direction of $\mathbf{k}_0$. The group velocity is given by the slope $d\omega/dk$ at the corresponding point of the dispersion band. In Fig. 3

we observe regions where the bands are flat, have a strong curvature or have a negative slope. Modes propagating in a flat band region have a very small group velocity. Therefore, they are of particular interest for the investigation of “slow light” [19]. In the strong curvature regions the group velocity is highly dispersive. As a consequence, only a slight variation in the angular frequency ω induces drastic changes in the direction ($\mathbf{k}$) leading to the so-called superprism effect [20]. The bands of negative dispersion open the door to the observation of negative refraction phenomena [21, 22]. At first, research on photonic crystals has mainly been focused on the photonic band gap property. However, more recently the dispersion properties of the allowed bands have become a topic of great interest where much can be explored.

Previously we described two-dimensional photonic crystals with allowed and forbidden bands for in-plane propagation. Modes with frequencies inside the photonic band gap are forbidden to exist within the interior of the crystal, unless there is a defect in the photonic crystal. A defect, or perturbation in the periodicity enables localized photonic states in the gap, whose formation and properties depend on the nature of the defect. For example, a properly designed point defect acts like a microcavity and a line defect like a waveguide for frequencies within the band gap. Introducing defects into a photonic crystal opens up a new dimension in the ability to control the propagation of light.

We will illustrate the formation of different types of localized modes within the photonic band gap by introducing a line defect into a two-dimensional photonic crystal with a square lattice of air holes in silicon. By modifying a line of holes in the otherwise perfect crystal, an allowed defect mode can be created within the photonic band gap. Light that propagates in the line defect (photonic crystal waveguide) with a frequency within the band gap of the crystal is confined to, and can be directed along this waveguide. In Fig.4 the formation of the defect modes are shown in the projected band structure, which projects all photonic crystal states onto the direction of propagation of light, along the ΓX direction in the reciprocal space. In Fig.4(a) the diameter of the holes is reduced as illustrated in the inset. This induces two defect modes that are allowed within the band gap. First, the steeper mode has guiding properties similar to a conventional waveguide mode. In fact, this "refractive-like" [23] mode does not "see" the photonic crystal so much as a periodic structure, but rather as material with an effective refractive index. Since the effective refractive index of the line defect is higher than the effective index of the surrounding crystal, the mode fulfils the total internal reflection condition (index guiding). Second, the flatter mode is a photonic crystal effect guided mode, meaning light is confined laterally because it is forbidden from entering the surrounding crystal. When reducing the diameter of the holes, this so-called donor mode is pulled down from the air band into

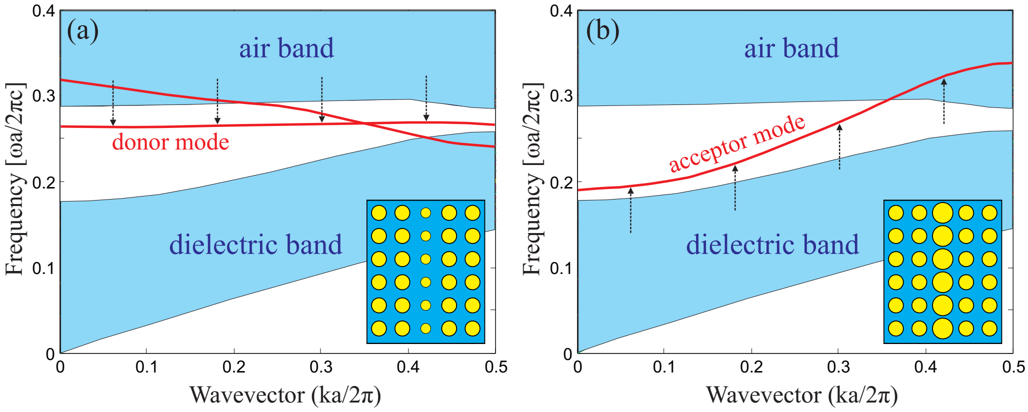

Figure 4: The projected band structure of TE modes for a waveguide in a square lattice of air holes in silicon. The direction of propagation of light is along the ΓX direction in the reciprocal space (wavevector between 0 and π/a). The gray shaded regions correspond to modes of the photonic crystal, which are states that can propagate through the crystal corresponding to the TE- and TM-modes in Fig.3. The defect modes are represented by dark solid lines. The arrows indicate how the defect modes have been pulled into the band gap. (a) Donor mode is pulled down from the air band when reducing the diameter of the air holes. A second "refractive-like" defect mode is index guided. (b) Acceptor mode is pushed up from the dielectric band when increasing the diameter of the air holes.

the photonic band gap as indicated by the arrows. A simple way to understand this is to examine the effects that a small variation in $\varepsilon(\mathbf{r})$ has on the frequency of a mode analogous to the formation of the photonic band gap. Increasing the dielectric constant ε in the line defect, by reducing the diameter of the holes, induces a negative frequency shift and therefore a defect state is pushed down from the air band into the gap. The donor mode has a flat dispersion relation which results in a small group velocity. One of the most common donor-type waveguide is a photonic crystal with a single row of missing holes, called W1 waveguide.

In Fig.4(b) the diameter of the holes is increased as illustrated in the inset. In this case, only one defect mode (acceptor mode) is created, which is governed by a purely photonic crystal mechanism of light confinement. By removing some more silicon (increasing the diameter of the holes) the corresponding frequency shift is positive and a defect state can be pushed up from the dielectric band into the gap as indicated by the arrows. This mode has the properties of the dielectric band. Again, we can recognize an analogy between defects in photonic crystals and impurities in a semiconductor.

The above discussion looked at photonic crystals that are periodic in the plane and of infinite extent orthogonal to the plane. Clearly, real structures cannot be this way. In order to realize two-dimensional photonic crystal phenomena in real three-dimensional structures, the most straightforward design is to fabricate a two-dimensional periodic crystal with a finite height: a photonic crystal slab, as shown in Fig.5. Such structures usually consist of a semiconductor core (high refractive index material) and a surrounding cladding of lower refractive index such as air or silicon dioxide (see Fig.5(b)). Therefore, this structure can confine light vertically within the slab via index guiding whereas the photonic crystal properties can be exploited in the plane of the periodicity. After fixing the materials for the slab and the surrounding cladding the critical design parameters for the photonic crystal properties are the lattice constant a, the slab thickness t and the hole diameter d. In Figure 5(a), a slab thickness of $0.5a$ and a hole diameter of $0.8a$ is used for a photonic crystal slab with a triangular lattice of air holes in silicon. The photonic band structure is more complicated than for the ideal two-dimensional photonic crystal. For symmetric slabs (same cladding above and below) the optical field can be divided into even or odd modes with respect to the mid-plane of the photonic crystal core layer. Although it is no longer possible to distinguish TE or TM modes, because the fields are also a function of the vertical coordinate, it is still useful to call them TM-like or TE-like modes.

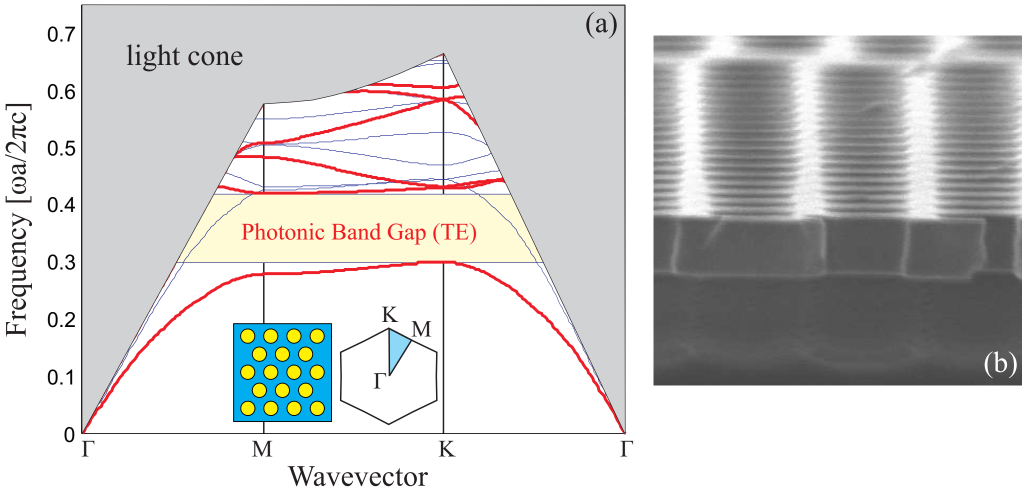

Figure 5: (a) Band diagram for a triangular lattice of air holes ($r/a = 0.35$) in silicon (ε=12.0), where a is the lattice constant. The frequencies for the two polarizations (TE-like modes in red, TM-like modes in blue) are plotted around the boundary of the irreducible Brillouin zone (shaded triangle). The thickness of the slab is chosen to be $t = 0.5a$ and the hole diameter is $d = 0.7a$. The light cone (grey region) contains the continuum of states that radiate into the air. There is an incomplete band gap region for TE-like guided modes. (b) SEM micrograph of the fabricated photonic crystal slab.

The index guiding property for the vertical confinement is described by the continuous light cone in the band diagram. Modes with frequencies above the light line $\omega = c\mathbf{k}_{//}$, shown as the shaded region in Fig.5, will radiate vertically and therefore leak energy into the cladding. The modes beneath the light cone cannot couple to any vertically radiating modes and so are confined to the slab. The presence of these radiating modes means that no complete photonic band gap is possible because there are radiating modes at every frequency (ω). Furthermore, if translational symmetry is broken, for example by a waveguide bend or a resonant cavity, then light can couple to the radiating modes and losses are inevitable. Various methods have been developed in order to minimize such coupling losses.

3 Numerical simulation methods

In order to predict and design the desirable optical properties of photonic crystals we need access to the appropriate theoretical tools. For numerical calculations, the continuous Maxwell equations must be discretized leading to a finite number of points that have to be solved. Here we will give a short introduction to two common computational approaches that have been used in this thesis for the simulation of photonic crystals, namely the frequency domain method and the time domain method. Respectively, frequency and time are discretized in addition to discretizing space. Frequency domain methods, based on the introduced eigenvalue equation (Eq. 3), are well-suited to calculating band structures and eigenstates. Time domain methods are better for computing the response of more complex geometries especially for the evolution of fields and transmission and resonance calculations.

3.1 Frequency domain method

The frequency domain method used in this thesis is a fully-vectorial, three-dimensional algorithm in a planewave basis computing eigenmodes of Maxwell's equations with periodic boundary conditions, also called MPB (MIT-Photonic-Bands). This method has been implemented by the MIT Ab Initio-physics group and is freely available under the GNU General Public License [24]. The goal of the frequency domain method is to solve the eigenvalue equation for the magnetic modes of periodic dielectric structures such as photonic crystals:

$$\nabla \times \left(\frac{1}{\varepsilon(\mathbf{r})} \nabla \times \mathbf{H}_{\omega}(\mathbf{r}) \right) = \left(\frac{\omega}{c} \right)^2 \mathbf{H}_{\omega}(\mathbf{r}). \tag{6}$$

This equation allows the determination of the allowed mode frequencies for a given crystal, and which wave-vectors k are associated with each of those modes. This leads to the characteristic photonic band structure. The subscript "ω" in equation (6) emphasizes that each field pattern corresponds to a specific frequency. As a next step, the field patterns are expanded into a basis of plane waves:

$$\mathbf{H}_{\omega}^{\mathbf{k}}(\mathbf{r}) = \sum_{\mathbf{G}\lambda} \mathbf{h}_{\mathbf{G}\lambda} \hat{\mathbf{e}}_{\lambda} e^{[i(\mathbf{k}+\mathbf{G})\cdot\mathbf{r}]}, \tag{7}$$

with $\hat{e}_{\lambda}$ as the unit vector designating the polarization and $\mathbf{G}$ as the reciprocal lattice vector of the photonic crystal. With the plane wave expansion the differential equation (6) converts into a system of linear equations that can be solved on a computer. The MPB method uses an iterative eigensolver, which iteratively improves approximate eigenstates, in order to calculate all of the eigenvalues $(\omega/c)^2$ for a given value of $\mathbf{k}$. For photonic crystal structures with defects the computational unit cell of the periodic crystal has to be replaced by a supercell, which contains the defect and is repeated periodically in order to allow the plane wave expansion. The supercell unit must be large enough to eliminate significant coupling between the periodic defects (such as cavities, waveguides and slabs). Furthermore, the lower modes in a large supercell are folded many times in the Brillouin zone, therefore the resulting modes must be inspected carefully. With large supercells the frequency domain methods incur large computational requirements both in time and in storage.

3.2 Time domain method

The time domain method used in this work is based on the finite integration technique, which rewrites Maxwell's equations in their integral form into a discrete formulation solving the electric and magnetic fields explicitly as a function of time. The implementation of this method is commercialized by CST GmbH (Computer Simulation Technology) under the product Microwave Studio using a code named MAFIA (Maxwell's finite integration algorithm) [25]. The finite integration time domain (FITD) is computationally similar to the well-known finite difference time-domain (FDTD) scheme. The only difference is related to the fact that the Maxwell equations are solved in integral form:

$$\oint_{\partial A} \mathbf{E}\cdot\mathbf{dr} = \iint_{A} -\frac{\partial}{\partial t}\mathbf{B}\cdot\mathbf{dA} \qquad \iint_{\partial V} \mathbf{B}\cdot\mathbf{dA} = 0$$

$$\oint_{\partial A} \mathbf{H}\cdot\mathbf{dr} = \iint_{A} -\left(\mathbf{J} + \frac{\partial}{\partial t}\mathbf{D}\right)\cdot\mathbf{dA} \qquad \int_{\partial V} \mathbf{D}\cdot\mathbf{dA} = \iiint_{V} \rho \mathrm{d}V. \tag{8}$$

These equations reveal their macroscopic character with the connection to geometric objects such as volumes V, areas A and lines. Both, the FITD and FDTD methods are based on the Yee algorithm, published originally by Kane Yee in 1966 [26]. The strength of Yee's method lies in its choice of sampling grid, in which every component of the electric field is surrounded by components of the magnetic field and vice versa. In the FITD method the integral form of the Maxwell equations (8) is directly translated to such a dual grid space with, on the one hand, the electric field, and on the other hand, the magnetic field. A typical grid size step for an accurate solution is in the order of $\lambda/10$. Further, since the electric and magnetic fields are interconnected in time and space the equations are solved in a leapfrog manner which samples values of E and H at times separated by half a time step so that the E-field and H-field updates are staggered. This iterative recursion technique is numerically stable with the following condition on the time step for the case of a regular equidistant coordinate grid:

$$c\Delta t = \left(\frac{1}{\Delta x^2} + \frac{1}{\Delta y^2} + \frac{1}{\Delta z^2} \right)^{-\frac{1}{2}}. \tag{9}$$

In order to eliminate back reflections in a finite numerical domain, containing for example the photonic crystal structure, special absorbing boundary conditions have to be added. One of the most effective boundary condition is the perfectly matched layers (PMLs) condition based on the idea suggested by Berenger in 1994 [27]. This condition provides a near reflectionless interface between the region of interest and the PML layers at a wide range of incident angles. The layers themselves are lossy, so that after a few layers the wave is significantly attenuated.

The time domain method is a versatile computational technique and has been widely applied in the modeling of finite photonic crystal structures. One of the main advantages is that you can use a broad-band pulse as the incident excitation which allows you to obtain the frequency response of your structure with a calculation involving the propagation of a single field. However, since FITD requires that the entire computational domain be gridded sufficiently fine to resolve both the smallest electromagnetic wavelength and the smallest geometrical feature in the model, very large computational domains can be developed, which results in very long calculation times. Likewise, resonant structures with a long electromagnetic time response result in a computationally expensive problem.

4 Fabrication methods

The fabrication process is today's main challenge in the realization of photonic crystals working in the near infrared region with structures of micro- and nanoscopic dimensions. Typically, high resolution lithography techniques are needed in order to meet the requirements of the designed structures. For planar two-dimensional devices, such techniques have been developed by the semiconductor industry, which has been driven by the demand for smaller and more integrated electronic devices. Silicon-on-Insulator (SOI) material is the most popular platform on which to build such 2D photonic crystal circuits due to its compatibility with CMOS processing tools and its favorable optical properties (transparent, high refractive index) at 1.55 μm wavelengths.

The photonic crystal structures in this work have been fabricated by the two most commonly used lithography techniques: electron beam lithography and deep ultraviolet lithography [28, 29]. Access to both fabrication techniques has been a strong point in this work. Each technique has its advantages and disadvantages. E-beam lithography is typically used for prototyping and mask-making for its high resolution and flexibility, whereas deep UV-lithography barely fulfills the resolution requirements but enables the fabrication process for larger production.

The main difference between the two lithography methods lies in the first step, where the photonic crystal pattern is written into a photoresist sensitive to an electron beam or deep UV light, such as PMMA. The e-beam lithography technique consists of scanning a beam of electrons across the resist film and depositing energy in order to replicate the photonic crystal pattern into the resist. This method is very flexible since it allows direct writing without the use of any mask. However, larger structures result in very long writing times and the high expense of making direct writing by e-beam lithography is unsuitable for volume production. However, if the e-beam version is used as a “master” structure from which copies could be made, then this would clearly open the way to cheaper, larger volume fabrication. This is where the deep UV technique comes in. The deep UV lithography technique consists of transferring the photonic crystal pattern in one exposure from a mask, usually fabricated by e-beam lithography, into the resist using deep UV light at a wavelength of 193 nm. This parallel writing process provides the possibility for mass production and industrial application. In order to accurately write the photonic crystal pattern into the resist, optical proximity corrections are needed for both lithography techniques. Structures, such as holes, that are situated at exposed places (e.g. corners, borders) are adjusted by the modification of the electron beam dose or the mask, respectively.

After the lithography process, the patterns in the photoresist are transferred into the silicon layer of the SOI wafer using dry etching technology, such as reactive ion etching (RIE) and deep reactive ion etching (DRIE). In order to achieve better optical properties (larger band gaps, lower losses, preventing the interaction between TM and TE modes), the photonic crystal slab structure must have mirror symmetry in the vertical direction, which is at this stage of fabrication broken by the presence of the substrate. Therefore, as a final step, the silicon photonic crystal structure is either undercut forming a membrane surrounded by air or covered with a silicon dioxide layer forming a complete oxide cladding. The membrane structure is realized by removing the silicon dioxide layer underneath the silicon slab using buffered hydrofluoric acid vapour (BHF) etching.

For this work, the photonic crystal membrane structures fabricated by e-beam lithography have been realized by IMT-Samlab (Institute of Microtechnology, University of Neuchâtel). The structures fabricated by deep UV-lithography are completely buried in silicon dioxide and have been realized by LETI (Laboratoire d'Electronique de Technologie de l'Information, France).

5 Photonic crystal components

Components based on photonic crystals have experienced major developments during the last ten to fifteen years. This progress is mainly due to improvements in the design of these devices and the fabrication techniques. However, the challenge of realizing the benefits of photonic crystals in practical systems with increased functionalities continues to be a major subject for research. In the following, we give a brief survey of published research on basic two-dimensional photonic crystal components. In accordance with the results presented in this thesis, we divide the survey into passive and active components and fit in our contributions to the photonic crystal research.

5.1 Passive components

Research on passive photonic crystal components focuses mainly on the introduction of different kinds of defects and on the engineering of the coupling efficiency from conventional optical components and external sources to photonic crystal structures.

Point defects in photonic crystals can create resonant microcavities, which are of great interest because they exhibit highly confined optical fields for a narrow frequency range. The cavity quality (Q) factor is one of the characteristic quantities that describe the strength of various interactions within the cavity. Much effort has been spent by different groups in design and fabrication in order to improve the Q factor of microcavities. One of the early photonic crystal cavity structures was integrated directly into a silicon waveguide [30]. It exhibited a modal volume of 0.055 μm^3 and a Q factor of 256 for a wavelength of 1.56 μm. In two-dimensional photonic crystals improvements in the Q have been achieved by tailoring the defect geometry surrounding the cavity, thus limiting radiation losses [31, 32]. We presented cavity structures that are fabricated by deep UV lithography and fully buried in a silicon dioxide cladding. Due to the cladding the cavity structure is well protected and very promising for various applications [33]. The cavity structure, which is formed by two identical Bragg reflectors and is situated inside a photonic crystal waveguide, is designed to realize both a high Q factor and high in-plane transmission. The structure was optimized by engineering the hole dimensions and positions of the Bragg reflectors based on several design methods that have been suggested for optimizing the performance of resonant cavities [34, 35]. However, due to the limited accuracy of our fabrication technology, we have kept the design as simple as possible while accepting lower performance for the cavity. Recently, nanocavities with an extremely high Q factor of 600 000 have been demonstrated in a two-dimensional photonic crystal slab [36, 37]. The important design rule that has been suggested consists of realizing a cavity design where the form of the electric field distribution within the cavity should slowly vary, most ideally as described by a gaussian function, in order to suppress out-of-plane losses. The cavity was formed by a photonic double-heterostructure consisting of a line-defect waveguide, along which the lattice constant of the photonic crystal increased in one or two steps towards the center. Due to the differences between the mode-gap frequencies along the line defect, the light is mainly confined to the central region. It is believed that cavities with Q factors of the order of several millions will be obtained in the future through improved fabrication techniques [36].

The photonic crystal waveguide and cavity form the basic building blocks for applications such as microlasers, filters, multiplexers and optical switches. A first detailed investigation of light propagation in linear defects has illustrated how true guided modes can be created in photonic crystal slabs [38]. In section 2.3 we have shown that a line defect in a two-dimensional photonic crystal can confine the light in the lateral direction if the defect mode is within the photonic band gap, and that a slab structure can confine the light in the vertical direction as long as the mode is below the light line. In order to realize an "ideal", intrinsically lossless, photonic crystal waveguide, it is necessary to design the geometric parameters of the line defect and the slab structure such as to position the defect mode within the center of the band gap as well as below the light line [39]. Recently, different optimized photonic crystal waveguide designs have been demonstrated, achieving a low-loss propagation bandwidth up to 125nm and propagation losses on the order of 8 to 14 dB/cm [40–42]. Although intrinsically lossless in the regime below the light line where no radiation modes are available, these photonic crystal waveguides still suffer from fabrication irregularities such as wall roughness, non-verticality and randomization of the hole position, size and shape. By further improving the fabrication process propagation losses in photonic crystal waveguides will continue to decrease.

With line defects in photonic crystals, waveguiding even around sharp turns can be realized. In one of the first experimental demonstrations of guiding and bending for a wavelength around 1.55 μm, near 100% efficiency around a 60° bend was observed [43]. With a practical and theoretical stage-by-stage analysis of light propagation around a 90° corner going from a ridge waveguide to a photonic crystal waveguide to the 90° corner, we have demonstrated nearly 90% bending efficiency [44, 45]. Further, in collaboration with the Ultrafast & Nanoscale Optics group in the Department of Electrical and Computer Engineering of the University of California, San Diego (US), we observed with subwavelength resolution the amplitude and phase of the optical field propagating in photonic crystal waveguide structures by means of scanning near-field optical microscopy [46, 47].

By combining one- and two-dimensional defects, a great variety of photonic crystal components can be imagined. For example, an add-drop filter has been demonstrated by combining a line defect forming a waveguide and isolated cavity defects [48]. As light propagates in the waveguide, light couples to the cavities corresponding to the specific resonance conditions and is radiated to free space. Channel drop filters have been investigated using a resonant cavity to tunnel light from one waveguide to another [40, 49, 50]. Further, a Mach-Zehnder interferometer in a two-dimensional photonic crystal leading to the possibility of dense device integration has been realized and its interference properties have been measured [51].

One of the main obstacles that hinders the further exploration of the described photonic crystal components is the difficulty to couple light from an external source to the photonic crystal structure. Large coupling losses are a direct result of the small geometric overlap and of the modal mismatch between the source (usually a fiber) and the semiconductor waveguide structure. In order to facilitate the coupling to the photonic crystal structure silicon strip waveguides are typically used. In addition, with efficient spot-size converters for coupling the light from a fiber to the silicon strip waveguide the coupling losses can be reduced to 1 dB [52]. A coupling efficiency of 95% has been demonstrated using a fiber taper waveguide formed from a standard silica single-mode optical fiber to evanescently couple light into guided modes of a photonic crystal waveguide [53]. Several taper structures have been suggested in order to achieve adiabatic modal conversion from conventional waveguides to photonic crystal waveguides [54–56]. Nevertheless, loss issues remain a challenge that needs to be addressed for photonic crystal devices to become practical.

Another concept is based on the dispersion properties for the allowed states within the photonic crystal structure. By engineering the mode dispersion, effects such as self-collimation and superprisms can be created. A theoretical study for self-collimated beams in photonic crystal structures has shown that bends and splitters can be constructed by truncating the photonic crystal [57]. The superprism effect, which has its potential application in wavelength division multiplexing devices, has been theoretically and experimentally demonstrated in planar photonic crystal geometries [20, 58]. Again, issues such as losses and coupling efficiencies need to be addressed to move towards practical integrated optical circuits.

5.2 Active components

Research on active photonic crystal components focuses on tunable or switchable devices and on the use of active materials. Tunability and nonlinearities open up new opportunities for photonic crystal circuits with increased and active functionalities. Photonic crystal microcavities are of special interest for active components due to their strong light confinement. Even small changes in the structure, the optical properties of the materials or the environment of the cavity can influence the optical response. Ideally, such a change should be reversible so that an active, tunable device on a very small scale can be realized.

Numerous ways to tune or switch photonic crystal devices have been demonstrated. One of the most common ways is temperature tuning induced by the temperature dependence of the refractive index of the material [59, 60]. However, with this method it is difficult to locally restrict the tuning effect on a chip. Both theoretical [61] and experimental [62, 63] work has demonstrated the possibility of infiltrating photonic structures with liquid crystals and achieving the desired modulation by electromagnetically rotating the director field of the liquid crystal or thermally inducing a phase transition in the liquid crystal. Tunable spectral filtering of a planar photonic crystal has been demonstrated by means of a nanofluidic delivery structure using fluids with different refractive indices [64]. Electro-optical switching has been presented using a PN junction to inject free charge carriers and induce electro-absorption [65]. First results on mechanically tunable photonic crystal structures point out their great potential for multifunctional integrated optical devices using MEMS technology [66–68]. By probing the highly localized field in the vicinity of a photonic crystal cavity with a silicon AFM tip, we have shown that on-off switching in the kHz range and tuning of the resonant wavelength can be achieved, depending on the position of the AFM tip with respect to the cavity structure [69].

Photonic crystal lasers can be created by incorporating active materials into photonic crystal cavities. A photonic crystal laser was demonstrated to exhibit peak emission at 1.55 μm [70, 71]. The cavity was formed by a single missing air hole in a triangular array of air holes in a thin InGaAsP membrane. The laser structures were optically pumped and the light was emitted vertically. In another experiment the spontaneous emission from a PbS quantum dot was modified when coupling to photonic crystal cavities. The dot emission mapped out the cavity resonances and was enhanced relative to the bulk emission [72].

In all-optical signal processing one needs to control light with light. Thus, nonlinear effects that change the optical properties of the material when light is present are needed. All-optical switching has been demonstrated by different groups with time responses varying from ms to fs depending on the mechanism and materials used. Fast band-edge tuning of a two-dimensional silicon photonic crystal has been demonstrated using 300 fs laser pulses [73]. A photonic crystal Mach-Zehnder type all-optical switch with InAs quantum dots acting as a nonlinear phase-shift source has been realized [74]. The non-linear optical phase shift was achieved at an optical energy of 100 fJ per pulse. We have demonstrated all-optical tuning and switching of a two-dimensional photonic crystal cavity in silicon. By focusing a laser onto the cavity region, both a thermal and a plasma dispersion effect are generated, allowing tuning and fast modulation up to the gigahertz level of the in-plane transmission [75]. Further, nonlinear photonic crystal structures can exhibit bistable behaviour, which can lead to the development of all-optical transistors and logic gates. Optical bistability is observed in photonic crystal cavities based on nonlinear absorption and dispersion effects [76, 77]. Due to the enhancement of the local energy density enabled by photonic crystal cavities the required input power for nonlinear behaviour is significantly reduced. These nonlinear effects have the potential to work as various signal processing functions in photonic crystal based optical circuits.

One of the objectives of today's on-going research is to increase the active functionality and to achieve applicability for photonic crystal devices in practical applications.

6 List of articles

The results of this thesis are constituted by the author's publications as listed below:

1. I. Märki, M. Salt and H. P. Herzig, *Practical and theoretical modal analysis of photonic crystal waveguides*, J. of App. Phys. **95**, 7-11 (2004).
2. I. Märki, M. Salt, R. Stanley and H. P. Herzig, *Characterization of Photonic Crystal Waveguides Based on Fabry-Pérot Interference*, J. of App. Phys. **96**, 6966-6969 (2004).
3. I. Märki, M. Salt, H. P. Herzig, R. Stanley, L. El Melhaoui, P. Lyan, J. M. Fedeli, *Characterization of buried photonic crystal waveguides and microcavities fabricated by deep UV-lithography*, J. of App. Phys. **98**, 013103 (2005).
4. P. Tortora, M. Abashin, I. Märki, W. Nakagawa, L. Vaccaro, M. Salt, H. P. Herzig, U. Levy, S. Fainman, *Observation of amplitude and phase in ridge and photonic crystal waveguides operating at 1.55 μm using heterodyne scanning near-field optical microscopy*, Opt. Lett. **30**, 2885 (2005).
5. M. Abashin, P. Tortora, I. Märki, U. Levy, W. Nakagawa, L. Vaccaro, H. P. Herzig, Y. Fainman, *Near-field characterization of propagating optical modes in photonic crystal waveguides*, Opt. Express **14**, 1643 (2006).
6. I. Märki, M. Salt, H. P. Herzig, R. Stanley, L. El Melhaoui, P. Lyan, J. M. Fedeli, *Optically tuneable microcavity in a planar photonic crystal silicon waveguide buried in oxide*, Opt. Lett. **31**, 011604 (2005).
7. I. Märki, M. Salt and H. P. Herzig, *Tuning the resonance of a photonic crystal microcavity with an AFM tip*, Opt. Express **14**, 2969 (2006).
8. R. Dändliker, I. Märki, M. Salt, A. Nesci, *Measuring Optical Phase Singularities at Subwavelength Resolution*, Journal of Optics A: Pure and App. Opt. **6**, 189-196 (2004). Special issue on singular optics, (2004)

7 Conclusion

The objectives of this thesis were to design, realize and investigate passive and active two-dimensional photonic crystal components in silicon. The study resulted in a better understanding of their fundamental properties and their limiting factors, such as fabrication defects and propagation losses. In addition, the results on the photonic crystal components with active functionalities contribute towards practical integrated optical circuits.

First, the fundamental properties of photonic crystals have been concisely described providing the basic theory and tools for the design of photonic crystal components. Following this, two-dimensional photonic crystal waveguides, bends, and microcavities have been investigated in detail. These structures are fundamental and indispensable to understand and analyze since they are considered basic building blocks for applications such as microlasers, filters, multiplexers, and optical switches.

The first set of photonic crystal structures, fabricated by e-beam lithography, consisted of a square array of cylindrical air holes in a thin silicon membrane surrounded by air. In a practical and theoretical stage-by-stage analysis of light propagation around a 90° bend in a photonic crystal waveguide the guided modes have been identified and transmission efficiencies of nearly 90% have been measured. Based on the fringe contrast of the measured Fabry-Pérot modulation in the transmission spectrum, the loss contributions of each waveguide element, such as tapers and the 90° corner, have been calculated. In addition, the feasibility of measuring the amplitude and the phase of the propagating field in ridge and silicon membrane photonic crystal waveguides operating around 1.55 μm wavelength has been demonstrated using the heterodyne scanning near-field optical microscopy (SNOM) technique. These measurements allowed the identification of the propagating modes of the photonic crystal waveguides and a detailed analysis of their propagation characteristics, which were found to be in agreement with theoretical predictions within the limits of fabrication tolerances. The obtained results show the usefulness of the heterodyne SNOM as an investigative and diagnostic tool in the study of optical nanostructures, in particular in cases where subwavelength-scale and near-field effects are important.

The second set of photonic crystal structures, fabricated by deep UV-lithography, consisted of a triangular array of cylindrical holes in a thin silicon membrane, completely buried in a silicon dioxide cladding. On the one hand, the cladding protected the structure from the environment making them more practical for applications; on the other hand the lower refractive index contrast between the structure and the cladding induced higher guiding losses. The optical characterization of the photonic crystal waveguide and resonant microcavity yielded a propagation loss of 150 dB/mm and a quality factor of 200, respectively. Despite the somewhat lower performance of these structures, they represent a step towards more practical photonic crystal components due to the protective cladding and the fabrication process providing the technology for cheaper, larger volume production.

Next, photonic crystal components with active functionalities have been investigated. In the first configuration, optical tuning and switching of a resonant microcavity in a silicon photonic crystal waveguide completely buried in silicon oxide has been achieved by focusing a laser onto the microcavity region. As a result, thermal and plasma dispersion effects are generated allowing tuning and fast modulation of the in-plane transmission with modulation bandwidths on the order of several 100 kHz and up to the GHz level, respectively. As shown in similar all-optical switching experiments [76–78], the thermal background connected to the induced linear and non linear effects such as free-carrier and two-photon absorbtion limits the straightforward integration into silicon photonic crystal based circuits for all-optical high-speed devices. Nevertheless, for use in nonlinear optical applications these results are an important step forward for silicon photonics.

In the second configuration, tuning and switching the optical properties of a photonic crystal microcavity is achieved based on a mechanical perturbation of the optical field. By means of a silicon AFM tip probing the highly localized optical field in the vicinity of the cavity, tuning, on-off switching and modulation of the transmission signal in the kHz range is obtained. When the AFM tip probed the center of the microcavity, vertical losses were induced and a damping of the transmission was observed allowing on-off switching and modulation. When inserting the AFM tip into one of the Bragg mirror holes, resonant wavelength tuning was possible. On the one hand, these results lead to a better understanding of the interaction of a silicon tip with the highly localized optical field within the cavity structure, which is of great importance in SNOM measurements. On the other hand, the progress in nanotechnology makes it possible to integrate tips for local tuning of individual resonant structures in photonic crystals that contain many functional components. Furthermore, one could attempt to create a standalone MEMS solution, which consists of a chip-based device combining tuning and switching functions going towards multi-functional programmable integrated optical circuits.

Finally, apart from photonic crystals, optical phase singularities produced by a grating and microlenses have been investigated by means of heterodyne scanning probe microscopy and high resolution interference microscopy. The optical phase singularities have been localized with subwavelength resolution. Such measurements could find an application in metrology in the fabrication process of nanostructured materials.

In summary, photonic crystal structures offer innovative ways to manipulate and control light on a wavelength scale. The combined progress in numerical design, microfabrication techniques and characterization of photonic crystal components build a solid basis for the development of more practical devices for various applications in a large range of domains such as telecommunication, information technologies, biology or chemistry. In particular, components with active functionalities open up additional possibilities for novel devices integrated with optical circuits such as miniature lasers, tunable filters and switches.

References

[1] Lord Rayleigh, "On the remarkable phenomenon of crystalline reflexion described by Prof. Stokes," Philosophical Magazine **26,** 256–265 (1888).

[2] H. Ghiradella, "Light and color on the wing: structural colors in butterflies and moths," Applied Optics **30,** 3492–3500 (1991).

[3] E. Yablonovitch, "Inhibited spontaneous emission in solid-state physics and electronics," Phys. Rev. Lett. **58**, 2059–2062 (1987).

[4] S. John, "Strong localization of photons in certain disordered dielectric superlattices," Phys. Rev. Lett. **58**, 2486–2489 (1987).

[5] S. John, J. Wang, "Quantum optics of localized light in a photonic band gap," Phys. Rev. B **43**, 12772 (1991).

[6] S. John, T. Quang, "Spontaneous emission near the edge of a photonic band gap," Phys. Rev. A **50**, 1764 (1994).

[7] E. Yablonovitch, T. J. Gmitter, and K. M. Leung, "Photonic band structure: The face-centered-cubic case employing nonspherical atoms," Phys. Rev. Lett. **67**, 2295 (1991).

[8] S. Y. Lin, J. G. Fleming, D. L. Hetherington, B. K. Smith, R. Biswas, K. M. Ho, M. M. Sigalas, W. Zubrzycki, S. R. Kurtz, J. Bur, "A three-dimensional photonic crystal operating at infrared wavelengths," Nature **394**, 251–253 (1998).

[9] J. G. Fleming and S. Y. Lin, "A three-dimensional photonic crystal with. stop band between 1.35 and 1.95 microns," Opt. Lett., vol. **24**, p. 49–51 (1999).

[10] S. G. Johnson and J. D. Joannopoulos, "Three-dimensionally periodic dielectric layered structure with omnidirectional photonic band gap," Appl. Phys. Lett. **77**, 3490 (2000).

[11] Y. A. Vlasov, X.-Z. Bo, J. C. Sturm, and D. J. Norris, "On-chip natural assembly of silicon photonic bandgap crystals," Nature, **414**(6861): 289–93 (2001).

[12] D.N. Sharp, M. Campbell, E.R. Dedman, M.T. Harrison, R.G. Denning and A.J. Turberfield, "Photonic crystals for the visible spectrum by holographic lithography," Opt. Quant. Elec. **34**, 3–12 (2002).

[13] W. M. Robertson, G. Arjavalingam, R. D. Meade, K. D. Brommer, A. M. Rappe, J. D. Joannopoulos, “Measurement of photonic band structure in a two-dimensional periodic dielectric array,” Phys. Rev. Lett. **68**, 2023 (1992).

[14] P. R. Villeneuve, M. Piché, “Photonic band gaps in two-dimensional square and hexagonal lattices,” Phys. Rev. B **46**, 4969 (1992).

[15] S. G. Johnson, S. Fan, P. R. Villeneuve, J. D. Joannopoulos, “Guided modes in photonic crystal slabs” Phys. Rev. B **60**, 5751–5758 (1999).

[16] C. M. Soukoulis, ed., Photonic Band Gap Materials (Kluwer, Dordrecht 1996)

[17] J. D. Joannopoulos, R. D. Meade, J. N. Winn, Photonic Crystals - Molding the Flow of Light (Princeton University Press, Princeton 1995).

[18] N. W. Ashcroft, N. D. Mermin, Solid State Physics (Sounders College, Fort Worth, 1976).

[19] M. Notomi, “Theory of light propagation in strongly modulated photonic crystals: Refractionlike behavior in the vicinity of the photonic band gap,” Phys. Rev. B **62**, 10696 (2000).

[20] H. Kosaka, T. Kawashima, A. Tomita, M. Notomi, T. Tamamura, T. Sato, and S. Kawakami, “Superprism phenomena in photonic crystals,” Phys. Rev. B **58**, R10096 (1998).

[21] Y. A. Vlasov, M. O’Boyle, H. F. Hamann, S. J. McNab, “Active control of slow light on a chip with photonic crystal waveguides,” Nature **438**, 65–69 (2005)

[22] H. Gersen, T. J. Karle, R. J. P. Engelen, W. Bogaerts, J. P. Korterik, N. F. van Hulst, T. F. Krauss, L. Kuipers, “Real-Space Observation of Ultraslow Light in Photonic CrystalWaveguides,” Phys. Rev. Lett. **94**, 073903 (2005).

[23] A. Mekis, J. C. Chen, I. Kurland, S. Fan, P. R. Villeneuve, J. D. Joannopoulos, “High Transmission through Sharp Bends in Photonic Crystal Waveguides,” Phys. Rev. Lett. **77**, 3787 (1996).

[24] S. G. Johnson and J. D. Joannopoulos, “Block-iterative frequency-domain methods for Maxwell’s equations in a planewave basis,” Optics Express **8**, no. 3, 173–190 (2001),

[25] T. Weiland, “A discretization method for the solution of Maxwell’s equations for six-component fields,” Electron. Commun. **31**, 116–120, 1977.

[26] K.S.Yee, “Numerical Solution of Initial Boundary Value Problems involving Maxwell’s Equations,” IEEE Trans. Antennas and Propagation **14**, 302–307 (1966).

[27] J.-P. Berenger, “A perfectly matched layer for the absorption of electromagnetic waves,” Journal of Computational Physics **114**, 185–200 (1994).

[28] C. C. Cheng and A. Scherer, “Fabrication of photonic band-gap crystals,” Journal of Vacuum and Science & Technology B **13**, 2696–2700 (1995).

[29] W. Bogaerts, V. Wiaux, D. Taillaert, S. Beckx, B. Luyssaert, P. Bienstman, R. Baets, “Fabrication of photonic crystals in silicon-on-insulator using 248-nm deep UV lithography,” IEEE J. Sel. Top. Quantum Electron. **8**, 928–934 (2002).

[30] J. S. Foresi, P. R. Villeneuve, J. Ferrera, E. R. Thoen, G. Steinmeyer, S. Fan, J. D. Joannopoulos, L. C. Kimerling, Henry I. Smith, E. P. Ippen, “Photonic-bandgap microcavities in optical waveguides,” Nature **390**, 143–145 (1997).

[31] K. Srinivasan, P. E. Barclay, O. Painter, J. Chen, A. Y. Cho, and C. Gmachl, “Experimental demonstration of a high quality factor photonic crystal microcavity,” Appl. Phys. Lett. **83**, 1915–1917 (2003).

[32] Y. Akahane, T. Asano, B.-S. Song, and S. Noda, “High-Q photonic nanocavity in a two-dimensional photonic crystal,” Nature **425**, 944–947 (2003).

[33] I. Märki, M. Salt, H. P. Herzig, R. Stanley, L. El Melhaoui, P. Lyan, J. M. Fedeli, “Characterization of buried photonic crystal waveguides and microcavities fabricated by deep UV-lithography,” J. of App. Phys. **98**, 013103 (2005).

[34] Ph. Lalanne, J. P. Hugonin, “Bloch-Wave Engineering for High-Q, Small-V Microcavities,” IEEE J. Quantum Electr. **39**, 1430–1438 (2003).

[35] Ph. Lalanne, S. Mias, J. P. Hugonin, “Two physicial mechanisms for boosting the quality factor to cavity volume ratio of photonic crystal microcavities,” Opt. Express **12**, 458–467 (2004).

[36] B. S. Song, S. Noda, T. Asano and Y. Akahane, “Ultra-high-Q photonic double-heterostructure nanocavity,” Nature Materials **4**, 207–210 (2005).

[37] T. Asano, B. S. Song, S. Noda, “Analysis of the experimental Q factors (∼1 million) of photonic crystal nanocavities,” Opt. Express **14**, 1996–2002 (2006).

[38] S. G. Johnson, P. R. Villeneuve, S. Fan, J. D. Joannopoulos, “Linear waveguides in photonic-crystal slabs,” Phys. Rev. B **62**, 8212–8221 (2000).

[39] M. Loncar, J. Vuckovic, A. Scherer, "Methods for controlling positions of guided modes of photonic-crystal waveguides," J. Opt. Soc. Am. B **18**, 1362–1368 (2001).

[40] M. Notomi, A. Shinya, S. Mitsugi, E. Kuramochi, and H. Y. Ryu, "Waveguides, resonators and their coupled elements in photonic crystal slabs," Opt. Express **12**, 1551–1561 (2004).

[41] E. Dulkeith, S. J. McNab, Y. A. Vlasov, "Mapping the optical properties of slab-type tow-dimensional photonic crystal waveguides," Phys. Rev. B **72**, 115102 (2005).

[42] M. Settle, M. Salib, A. Michaeli, Th. F. Krauss, "Low loss silicon on insulator photonic crystal waveguides made by 193nm optical lithography," Opt. Express **14**, 2440–2445 (2006).

[43] E. Chow, S. Y. Lin, J. R. Wendt, S. G. Johnson, J. D. Joannopoulos, "Quantative analysis of bending efficiency in photonic-crystal waveguide bends at l = 1.55 mm wavelengths," Optics Letters **26**, 286–288 (2001).

[44] I. Märki, M. Salt and H. P. Herzig, "Practical and theoretical modal analysis of photonic crystal waveguides," J. of App. Phys. **95**, 7–11 (2004).

[45] I. Märki, M. Salt, R. Stanley and H. P. Herzig, "Characterization of Photonic Crystal Waveguides Based on Fabry-Pérot Interference," J. of App. Phys. **96**, 6966–6969 (2004).

[46] P. Tortora, M. Abashin, I. Märki, W. Nakagawa, L. Vaccaro, M. Salt, H. P. Herzig, U. Levy, S. Fainman, "Observation of amplitude and phase in ridge and photonic crystal waveguides operating at 1.55 μm using heterodyne scanning near-field optical microscopy," Opt. Lett. **30**, 2885 (2005).

[47] M. Abashin, P. Tortora, I. Märki, U. Levy, W. Nakagawa, L. Vaccaro, H. P. Herzig, Y. Fainman, "Near-field characterization of propagating optical modes in photonic crystal waveguides," Opt. Express **14**, 1643 (2006).

[48] S. Noda, A. Chutinan, and M. Imada, "Trapping and emission of photons by a single defect in a photonic bandgap structure," Nature **407**, 608–610 (2000).

[49] S. Fan, P. R. Villeneuve, J. D. Joannopoulos, M. J. Khan, C. Manolatou, and H. A. Haus, "Theoretical analysis of channel drop tunneling processes," Phys. Rev. B **59**, 15882–15892 (1999).

[50] Y. Akahane, T. Asano, H. Takano, B. -S. Song, Y. Takana, and S. Noda, “Two-dimensional photonic-crystal-slab channeldrop filter with flat-top response,” Opt. Express **13**, 2512–2530 (2005).

[51] M. H. Shih, W. J. Kim, W. Kuang, J. R. Cao, H. Yukawa, S. J. Choi, J. D. O’Brien, and P. D. Dapkus, “Twodimensional photonic crystal Mach-Zehnder interferometers,” Appl. Phys. Lett. **84**, 460 (2004).

[52] S. McNab, N. Moll, and Y. Vlasov, “Ultra-low loss photonic integrated circuit with membrane-type photonic crystal waveguides,” Opt. Express **11**, 2927–2939 (2003)

[53] P. E. Barclay, K. Srinivasan, M. Borselli, and O. Painter, “Efficient input and output optical fiber coupling to a photonic crystal waveguide,” Opt. Lett. **29**, 697–699 (2004).

[54] M. Palamaru and P. Lalanne, “Photonic crystal waveguides: out-of-plane losses and adiabatic modal conversion,” Appl. Phys. Lett. **78**, 1466–1469 (2001).

[55] A. Talneau, P. Lalanne, M. Agio, and C. M. Soukoulis, “Low-reflection photonic-crystal taper for efficient coupling between guide sections of arbitrary widths ,” Opt. Lett. **27**, 1522–1524 (2002).

[56] A. Mekis and J. D. Joannopoulos, “Tapered couplers for efficient interfacing between dielectric and photonic crystal waveguides,” J. Lightwave Technol. **19**, 861–865 (2001).

[57] X. Yu, S. Fan, “Bends and splitters for self-collimated beams in photonic crystals,” App. Phys. Lett. **83**, 3251 (2003).

[58] L. Wu, M. Mazilu, T. Karle, and T. Krauss, “Superprism phenomena. in planar photonic crystals,” IEEE J. Quantum Electron. **38**, 915–918 (2002).

[59] E. A. Camargo, H. M. H. Chong and R. M. De La Rue, “2D Photonic crystal thermo-optic switch based on AlGaAs/GaAs epitaxial structure,” Optics Express **12**, 588–592 (2004).

[60] B. Wild, R. Ferrini, R. Houdré, M. Mulot, S. Anand, C. J. M. Smith, “Temperature tuning of the optical properties of planar photonic crystal microcavities,” Applied Physics Letters **84**, 846–848, (2004).

[61] D. M. Pustai, A. Sharkawy, S. Shi, D. W. Prather, “Tunable photonic crystal microcavities,” Applied Opitcs **41**, 5574–5579, (2002).

[62] Ch. Schuller, F. Klopf, J. P. Reithmaier, M. Kamp, and A. Forchel, "Tunable photonic crystals fabricated in III-V semiconductor slab waveguides using infiltrated liquid crystals," Applied Physics Letters **82**, 2767–2769 (2003).

[63] S. M. Weiss, H. Ouyang, J Zhang, Ph. M. Fauchet, "Electrical and thermal modulation of silicon photonic bandgap microcavities containing liquid crystals," Optics Express **13**, 1090–1097, (2005).

[64] D. Erickson, T. Rockwood, T. Emery, A. Scherer, D. Psaltis, "Nanofluidic tuning of photonic crystal circuits," Opt. Lett. **31**, 59–61, (2006).

[65] A. Sharkawy, S. Shi, D. W. Prather, "Electro-optical switching using coupled photonic crystal waveguides," Optics Express **10**, 1048–1059, (2002).

[66] W. Park, J.-B. Lee, "Mechanically tunable photonic crystal structure," Applied Physics Letters **85**, 4845–4547, (2004).

[67] S. Iwamoto, S. Ishida, Y. Arakawa, M. Tokushima, A. Gomyo, H. Yamada, A. Higo, H. Toshiyoshi, H. Fujita, "Observation of micromechanically controlled tuning of photonic line-defect waveguide," Applied Physics Letters **88**, 011104 (2006).

[68] T. Takahata, K. Hoshino, K. Matsumoto, I. Shimoyama, "Photonic crystal tuned by cantilever," 18th IEEE International Conference on Micro Electro Mechanical Systems, Miami, Florida, USA, January 30 - February 3, 2005.

[69] I. Märki, M. Salt and H. P. Herzig, "Tuning the resonance of a photonic crystal microcavity with an AFM tip," Opt. Express **14**, 2969 (2006).

[70] O. J. Painter, A. Husain, A. Scherer, J.D. O'Brien, I.Kim, and P.D.Dapkus, "RoomTemperature Photonic Crystal Defect Lasers at Near-Infrared Wavelengths in InGaAsP," J. Lightwave Tech. **17**, 2082–2088 (1999).

[71] M. Loncar, T. Yoshie, A. Scherer, P. Gogna, and Y. Qiu, "Low-threshold photonic crystal laser," Appl. Phys. Lett. **81**, 2680–2682, (2002).

[72] I. Fushman, D. Englund, and J. Vuckovic, "Coupling of PbS quantum dots to photonic crystal cavities at room temperature," App. Phys. Lett. **87**, 241102 (2005).

[73] S. W. Leonard, H. M. van Drield, J. Schilling, R. B. Wehrspohn, "Ultrafast band-edge tuning of a two-dimensional silicon photonic crystal via free-carrier injection," Phys. Rev. B **66**, 161102 (2002).

[74] N. Hitoshi, Y. Sugimoto, K. Kanamoto, N. Ikeda, Y. Tanaka, Y. Nakamura, S. Ohkouchi, Y. Watanabe, K. Inoue, H. Ishikawa, and K. Asakawa, "Ultra-fast photonic crystal/quantum dot alloptical switch for future photonic networks," Opt. Express **12**, 6606–6614 (2004).

[75] I. Märki, M. Salt, H. P. Herzig, R. Stanley, L. El Melhaoui, P. Lyan, J. M. Fedeli, "Optically tunable microcavity in a planar photonic crystal silicon waveguide buried in oxide," Optics Letters **31**, 011604, (2006).

[76] P. E. Barclay, K. Srinivasan, and O. Painter, "Nonlinear response of silicon photonic crystal microresonators excited via an integrated waveguide and fiber taper," Opt. Express **13**, 801–820 (2005).

[77] M. Notomi, A. Shinya, S. Mitsugi, G. Kira, E. Kuramochi, and T. Tanabe, "Optical bistable switching action of Si high-Q photonic-crystal nanocavities," Opt. Express **13**, 2678–2687 (2005).

[78] T. Uesugi, B.-S. Song, T. Asano, S. Noda, "Investigation of optical nonlinearities in an ultra-high-Q Si nanocavity in a two-dimensional photonic crystal slab," Opt. Express **14**, 377–386 (2006).

Part II
Articles

Practical and theoretical modal analysis of photonic crystal waveguides

Iwan Märki, Martin Salt, and Hans Peter Herzig

University of Neuchâtel, Institute of Microtechnology,
Rue A.-L. Breguet 2, CH-2000 Neuchâtel, Switzerland

Abstract

We present practical and theoretical, stage-by-stage analysis of light propagation around a 90° corner in a two-dimensional photonic crystal waveguide. Using a series of different samples we quantify the coupling efficiency between the conventional ridge waveguide and the photonic crystal waveguide as well as the bending efficiency around the 90° corner. From this, the transmission spectra indicate nearly 90% bending efficiency. We compare the experimental results to the three-dimensional simulated band diagram and field distribution. The propagating defect modes are identified in detail and we show that efficient transmission around sharp bends in photonic crystal waveguides can be achieved for leaky modes above the light line with short photonic crystal sections.

DOI: 10.1063/1.1737809.

1 Introduction

Light propagation in photonic crystal waveguides is a topic under intense investigation. By introducing a properly designed line defect in a photonic crystal structure, propagating modes confined within the defect are created [1–10]. Depending on the nature of the guided defect mode, waveguiding with low losses even around sharp bends can be achieved [11–16]. We present thorough experimental and theoretical analysis of light propagation around a 90° corner in a photonic crystal slab. Quantative transmission spectra of samples with different designs are compared to fully (3D) simulations for a more complete understanding of the transmission efficiency, the propagating modes and the coupling between the ridge waveguide and the photonic crystal waveguide. We identify in detail the propagating defect modes and show that efficient transmission around sharp bends can be achieved above the light line. In this paper we concentrate on the modal analysis of the photonic crystal waveguide whereas the experimental results will be presented in more detail elsewhere.

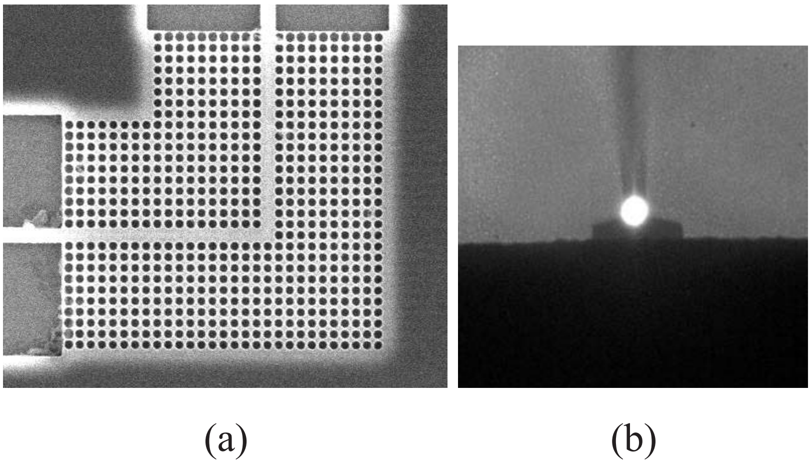
(a) (b)

Figure 1: Scanning electron microscope image of the 90° bend photonic crystal waveguide.

In our case the photonic crystal consists of a square array of cylindrical air holes in a thin Silicon membrane surrounded by air. The structure is designed to give rise to a TE-like (in-plane polarization) photonic band gap around $\lambda \sim 1.5$ μm. The design parameters of the photonic crystal structure are the lattice constant a=496 nm, the hole radius r=190 nm and the slab thickness t=290 nm. Our waveguides are fabricated in Silicon-on-insulator (SOI) wafers [5, 17]. The thickness of the Silicon slab is defined by oxidation and HF dip. The photonic crystal waveguide structure is then written into a PMMA layer by means of electron beam lithography. Then, we use RIE and DRIE to transfer the structure from the PMMA layer into the Silicon. Lastly, buffered hydrofluoric acid vapour (BHF) etching removes the silicon dioxide layer underneath the Silicon slab forming the membrane (Fig. 1(a)). Measurements are performed with an optical setup that includes a tunable laser source. TE-polarized light is coupled into a wide (10 μm) ridge waveguide on a SiO_2 substrate using an aspheric lens with a high numerical aperture (NA=0.65). Chemically etched end-facets at the input and output of the waveguide greatly reduce scattering of the laser light and allow a better coupling at the input and a very well defined mode profile at the output (Fig. 1(b)). To measure the transmitted intensity, the light is collected at the output of the waveguide by a microscope objective (NA=0.35) and focused onto an InGaAs detector. The tunable laser source allows us to measure the transmission spectrum ranging from 1440 nm to 1580 nm.

In order to study the effects of ridge waveguide to photonic crystal waveguide modal mismatch and induced modal conversion, we fabricated a series of samples that represent the different sub-elements of a final photonic crystal bend sample. This allows a better understanding of how each element contributes to the final photonic crystal bend spectrum. The first design is a simple, straight multimode waveguide (Fig. 2(a)) on a SiO2 substrate with a width of 10 μm and a thickness of 290 nm. It serves as reference for the transmission efficiency [12]. The second design is a straight waveguide with a taper (Fig. 2(b)) that reduces the width to 500 nm, leading to a waveguide section of a length of 25 μm in the middle and again a taper to increase the width back to 10 μm. The 25 μm middle waveguide section is a free-standing membrane and its width is approximately equal to the width of the photonic crystal waveguide defect channel. This second design allows us to observe the influence of the taper-induced modal conversion. The next stage is the insertion of the photonic crystal containing a straight, single line defect (no holes) into the middle of the waveguide (Fig. 2(c)). The photonic crystal section is again a free-standing membrane due to the under-etching of the SiO2 substrate through the holes. It has a length of 20 μm and allows us to study the effect of the modal mismatch between the ridge waveguide and the photonic crystal waveguide [18], as well as losses created by the crystal. Finally, the 90° bend is introduced into the photonic crystal waveguide section (Fig. 2(d)).

2 Transmission efficiency and modal analysis

To obtain the approximate transmission efficiency of the different waveguides, shown in Fig. 3(a), we first remove numerically the periodic Fabry-Pérot interference pattern, which is due to the smooth end-facets. Secondly, we divide the transmission spectra by the spectrum of the simple, straight, reference waveguide (a) for normalization. This eliminates extrinsic effects of the end injection and

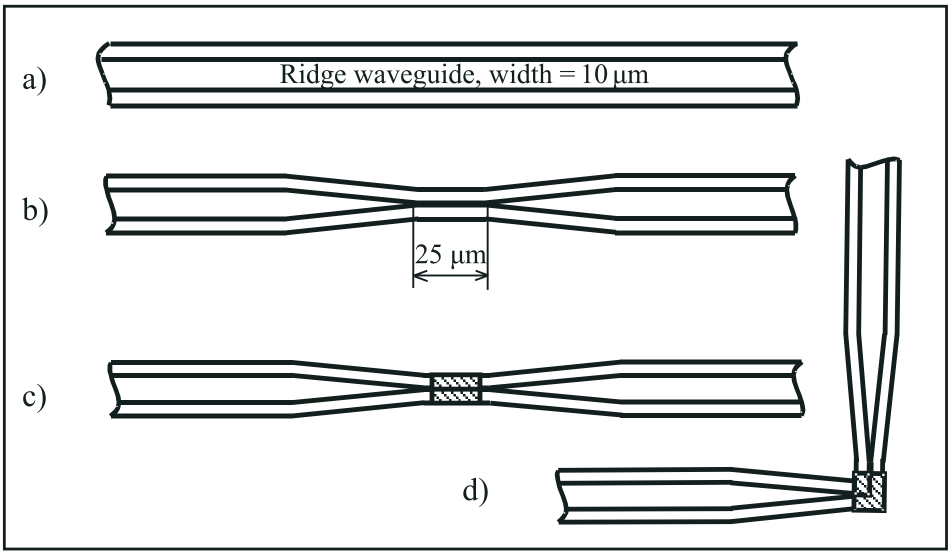

Figure 2: Designs of the fabricated waveguides: (a) simple straight waveguide (width=10 μm); (b) straight waveguide with taper and narrow width section (width=500 nm); (c) straight waveguide with photonic crystal waveguide (photonic crystal waveguide length=25 μm); and (d) waveguide with 90° bend.

most of the spectral response of the measurement optics. Repeated measurement of the same sample and of different samples of the same type has shown that an error of about 10% has to be attributed to the transmission measurements. These errors are due to changes in the alignment of the optical measurement system and due to fabrication-induced variations between the different waveguides. For the straight waveguide containing the taper and the small width section we observe comparatively high transmission efficiency over the entire measured frequency range in respect to the reference waveguide (a). Therefore we conclude that there are only slight losses induced by the taper in our set-up, which indicates a good modal conversion. It also indicates that the majority of the injected light must couple to the lower-order modes of the waveguide.

For the straight photonic crystal waveguide channel a high transmission efficiency is observed for the lower frequency range whereas for the higher frequency range the transmission is near to zero. The cut-off frequency is around 1.96×10^{14} Hz. The high transmission efficiency for the lower frequency range indicates a high coupling efficiency with low propagation loss and therefore a small modal mismatch between the ridge waveguide and the photonic crystal waveguide. From the measurement data we have estimated the propagation loss in the photonic crystal section to be 25 dB/mm in the best case. Details of the loss calculation will be presented elsewhere. A transmission efficiency of nearly 90%, which in-

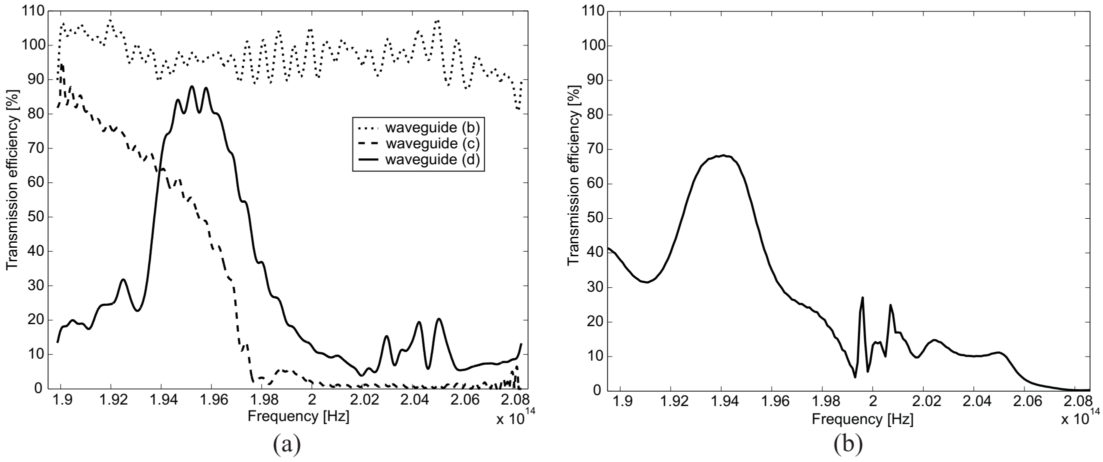

Figure 3: (a) Transmission efficiency calculated from the measured transmission spectra in reference to the simple, straight ridge waveguide with width of 10 μm. The rapid fluctuations are due to interference in the optical system that has not been eliminated in the filtering and normalizing process. (b) Fully 3D simulated transmission efficiency for the 90° bend waveguide.

cludes ridge waveguide to photonic crystal losses, is observed for the 90° bend waveguide at a frequency of 1.957×10^{14} Hz. It has a bandwidth of Δf $\approx$ 2700 GHz for a transmission efficiency of more than 60%. In Fig. 3(b) we show the fully 3D simulated transmission efficiency for the 90° bend waveguide. The simulation has been performed by a 3D FITD algorithm [19]. The general shape of the simulated transmission spectrum compares relatively well with the measured transmission efficiency. The observed differences are due to variations between the ideal simulated structure and the fabricated structure. The simulated photonic crystal structure was slightly shorter than the real structure due to the limited calculation capacity. Also, the many parameters (hole radius, lattice period, slab thickness, surface roughness) and the lengthy calculations do not allow rigorous convergence to the response of the real fabricated structure.

For a better understanding of the observed results we introduce the computed dispersion diagram for TE-like modes of the photonic crystal waveguide obtained by a fully three-dimensional calculation [20]. The guided defect modes, shown in Fig. 2, are represented by solid black lines. The dark grey regions correspond to modes of the photonic crystal, which are states that can propagate through the crystal. Guided modes that exist in that region can couple to the states of the photonic crystal and leak energy into it. The light line is indicated by the thin solid black line. Modes above the light line (light grey region) can escape in the vertical direction and therefore can leak energy into the air.

The first guided mode, labeled e1, is a laterally even mode [9]. Its disper-

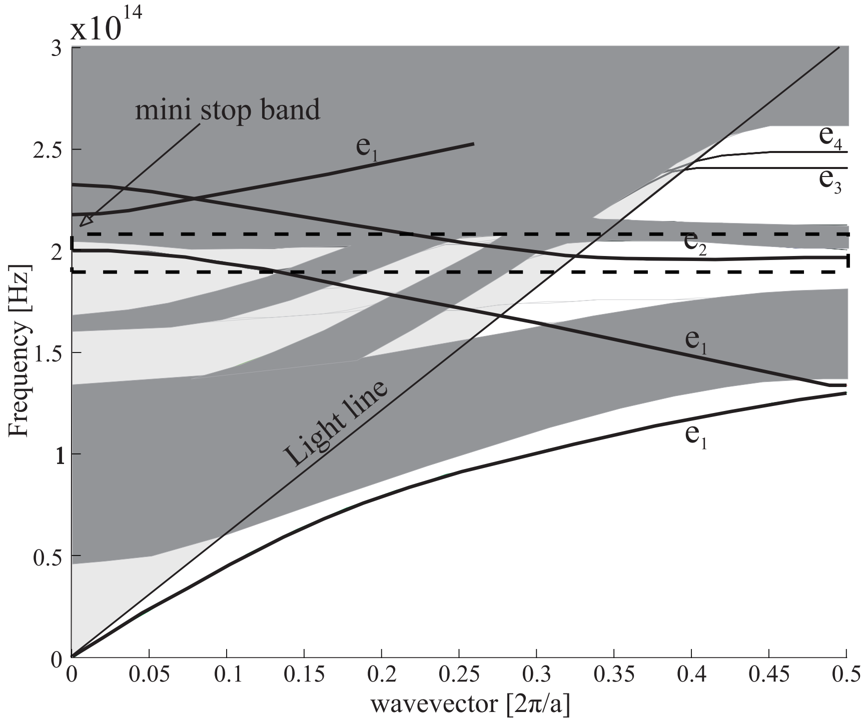

Figure 4: Computed dispersion diagram for TE-like guided modes in the photonic crystal waveguide. The defect modes are represented by solid black lines and are labeled e1 and e2. The dark gray regions correspond to modes of the photonic crystal, which are states that can propagate through the crystal.

sion is comparable to the folded dispersion of a standard ridge waveguide mode. It sees the periodicity of the photonic crystal weakly, rather seeing an average refractive index. The influence of the photonic crystal is especially observed at the boundaries of the Brillouin zone where the dispersion slope is flattened and where a mini stop band opens up each time the mode is folded back into the first Brillouin zone. This mode is called the leaky refractive-like mode [5,6,8,11] because above 1.1×10^{14} Hz it leaks energy into the photonic crystal, when crossing regions where the density of crystal modes is high, and into air where it is located above the light line. Indeed, both can occur at the same time. The second guided mode, labeled e2, is a laterally odd mode and is located in the first bandgap of the photonic crystal [9]. By introducing the defect line into the photonic crystal, the e2 mode is pulled down from the upper crystal band and therefore has the symmetry thereof. This mode is a truly photonic band gap effect guided mode. Generally, below the light line this mode is expected to be guided with very low loss, often even through waveguide channels with sharp corners, since it lies within the photonic bandgap. This mode is called the diffractive-like mode because its dispersion depends very strongly on the surrounding periodic structure of the crystal [5, 8, 11].

The region encircled with a dotted rectangle in Fig. 2 indicates the measurement range shown in Fig. 3(a). We observe that the described refractive-like and diffractive-like guided modes are present in the measurement region. The refractive-like mode has a similar wavevector and field distribution to the fundamental mode of the ridge waveguide [6], therefore the coupling from the ridge waveguide to this refractive-like mode is expected to be quite efficient, whereas the coupling efficiency from the ridge waveguide to the diffractive-like mode is expected to be very low because of the mode symmetry mismatch [8].

The measured transmission spectrum of the straight photonic crystal waveguide (Fig. 3(a)) indicates efficient coupling from the ridge waveguide up to a frequency of 1.96×10^{14} Hz, which corresponds to about the lower edge of the mini stop band of the refractive-like mode in the dispersion diagram. Above the cut-off frequency the guided modes are either not available (e1) or situated in regions where the density of photonic crystal states is high (e2), therefore the mode from the ridge waveguide couples to the existing states of the photonic crystal, leaks energy into it and is no longer guided in the defect. This lack of light guidance corresponds to the very low measured transmission efficiency. These agreements between the measurements and the dispersion diagram confirm the coupling to the leaky refractive-like mode of the photonic crystal waveguide.

For low-loss transmission through a 90° bend waveguide a diffractive-like mode, which is located below the light line and in the photonic band gap, is desirable. A refractive-like mode is not expected to have a particularly high transmission efficiency around sharp bends. Since we have shown in the previous section that light from the ridge waveguide couples effectively into the refractive-like mode of the photonic crystal waveguide, a low transmission efficiency is expected. Nevertheless, the measured transmission spectrum of the 90° bend waveguide reaches nearly 90% at a frequency of 1.957×10^{14} Hz. Several observations in comparing the measurements and the dispersion diagram can give information as to why the observed high transmission efficiency is achieved. We observe that the frequency range of high transmission efficiency is situated close to the cut-off frequency of the straight photonic crystal waveguide, which corresponds to the mini-stop band edge in the dispersion diagram. The cut-off frequency shift between the straight and the 90° bend waveguide is caused by fabrication-induced deviations in the crystal structure. In our simulations we have observed that the mini-stop band edge position depends strongly on the design parameters. As mentioned already, the flattening of the dispersion slope approaching the mini-stop band edge indicates the increased effect of the photonic crystal structure on the refractive-like waveguide mode. Due to this increased effect of the photonic crystal structure, two positive observations in respect of the transmission efficiency can be made. First, drawing nearer to the mini-stop band edge, Loncar et. al. have observed that the propagation losses of the leaky refractive-like mode decrease [7]. Second, due to the flattened dispersion, the density of wavevectors of the propagating defect mode that are accessible for the light at the bend has increased, which makes an efficient change of propagation direction and high transmission around the 90° bend more probable. In addition, close to the edge of the Brillouin zone, the field distribution in the corner is such that an efficient coupling to the perpendicular photonic crystal waveguide is possible.

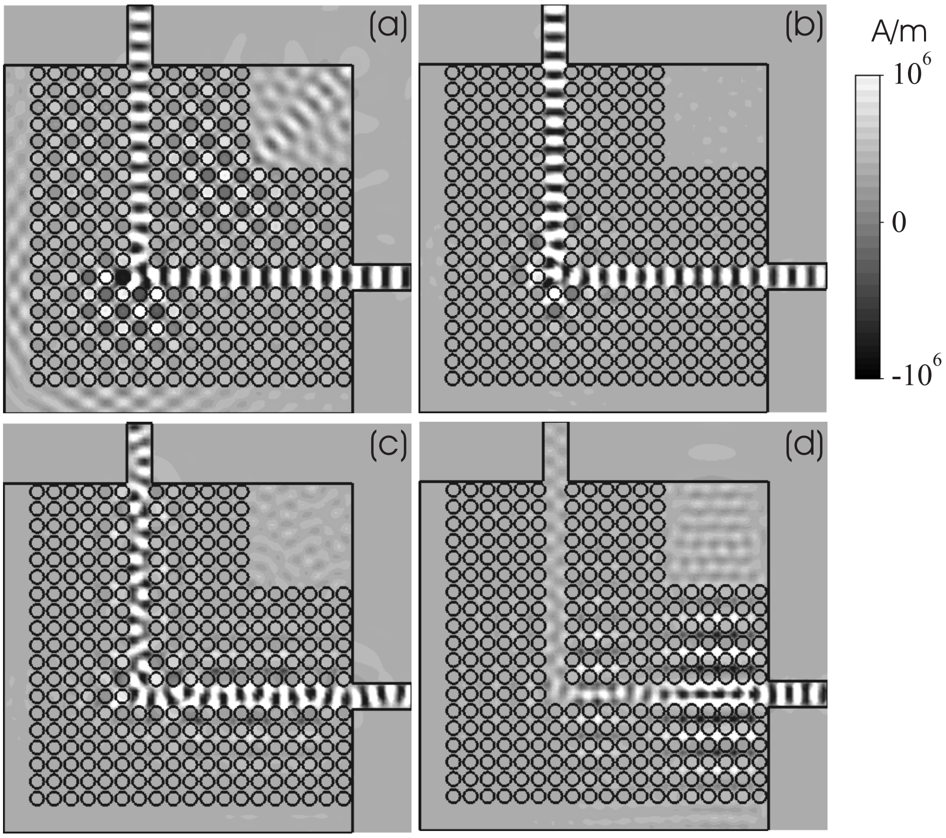

Figure 5: Fully 3D simulated field distribution (magnetic field perpendicular to the photonic crystal membrane) of the light propagating around the 90° bend waveguide at different frequencies: (a) at 1.8614e^{14} Hz (b) at 1.9481e^{14} Hz (c) at 2.0286e^{14} Hz and (d) at 2.0878e^{14} Hz.

The fully 3D simulated field distribution (magnetic field perpendicular to the photonic crystal membrane) of the light propagating around the 90° bend waveguide is shown in Fig. 5 at different frequencies. At lower frequencies the e1 mode behaves like an index-guided mode, which can be seen in Fig. 5(a). The light is well guided up to the bend, where it is then mostly reflected by the crystal, since the frequency of the light is situated in the range of the first photonic band gap. Only a small amount of light is guided around the bend. Increasing the frequency into the region where the dispersion slope flattens, the transmission efficiency around the bend increases due to the more diffractive-like character of the guided e1 mode (Fig. 5(b)). We also notice that at the bend a small amount of energy couples to the e2 mode. However, it disappears after a few periods because according to the dispersion diagram e2 couples to states of the photonic crystal and thus leaks energy into the crystal. Increasing the frequency close to the mini-stop band edge, the ridge waveguide mode couples to the e1 mode, which then couples in the corner to the several modes (beating in the field distribution) due to the broken symmetry matching the field distribution at the corner Fig. 5(c). Amongst others, the e2 mode can be identified in both of the waveguide branches. One part of the e2 mode is guided around the bend to the exiting ridge waveguide whereas the other part is reflected in the corner. Due to the low modal conversion efficiency between the e1 and the e2 mode the transmission efficiency decreases. The discussed modal conversion could be an interesting point of study. Since the e2 mode is truly photonic band gap effect guided and therefore is preferable to the e1 mode for low loss guiding, it might be possible to design a waveguide that deliberately breaks the symmetry of the e1 mode in order to couple to e2 mode. Efficient modal conversion from a ridge waveguide mode to the e1 mode and then to the e2 mode might then be achieved. At the frequency of 2.08*1014 Hz no propagating mode exists outside of regions with a high density of photonic crystal states, therefore light couples to the photonic crystal modes and is no longer confined within the defect (Fig. 5(d)). The comparison of the measurements with the dispersion diagram and the field simulation has shown that the measured maximum transmission efficiency is mainly associated with the leaky refractive-like mode, whereas the small peaks above the cut-off frequency, seen in both experiment and theory, are associated with weak coupling to the diffractive-like mode.

3 Conclusion

To conclude, by comparing different designs of waveguides with 3D calculation, we have identified the guided modes propagating around the 90° bend waveguide. High transmission efficiency was achieved with the leaky refractive-like mode. Despite the vertical losses, the leaky refractive-like mode presents some interesting advantages for short photonic crystal waveguide sections. Due to the good modal matching, a high coupling efficiency is observed between the conventional ridge waveguide and the photonic crystal waveguide mode. We have shown that the refractive-like mode can also be guided effectively around sharp bends close to the mini-stop band at the boundary of the Brillouin zone where the dispersion slope in the band diagram becomes flatter and the mode gains a more diffractive-like character. Further improvement of the transmission efficiency should be possible by reducing the sidewall roughness of the photonic crystal. By optimizing the design of the 90° bend, by restructuring the layout of the corner, it should be possible to broaden the transmission bandwidth [15, 21]. The presented results prove that the leaky refractive-like mode can be used in devices containing short photonic crystal sections and can exhibit quite high transmission efficiencies even around sharp waveguide bends.

4 Acknowledgements

The authors acknowledge F. Schädelin, S. Gautsch, U. Staufer and P.-A. Künzi for useful discussions and for fabricating the photonic crystal waveguide samples. Furthermore, the authors thank R. Stanley of the Swiss Center of Electronics and Microtechnology (CSEM) for fruitful discussions. This work is funded under a joint projects program between the Swiss Center of Electronics and Microtechnology (CSEM) and the IMT-Uni Neuchâtel.

References

[1] S.G. Johnson, P.R. Villeneuve, S. Fan, J.D. Joannopoulos, "Linear waveguides in photonic-crystal slabs," Physical Review B **62**, 8212–8222 (2000).

[2] Loncar, J. Vuckovic, A. Scherer, "Methods for controlling positions of guided modes of photoniccrystal waveguides," J. Opt. Soc. Am. B **18**, 1362–1368 (2001).

[3] M.D.B. Charlton et. al., "Experimental investigation of photonic crystal waveguide devices and line-defect waveguide bends," Materials Science and Engineering B **74**, 17–24 (2000).

[4] S.Y. Lin, E. Chow, S.G. Johnson, J.D. Joannopoulos, "Demonstration of highly efficient waveguiding in a photonic crystal slab at the 1.5-μm wavelength," Optics Letters **25**, 1297–1299 (2000).

[5] M. Loncar, T. Doll, J. Vuckovic, A. Scherer, "Design and Fabrication of Silicon Photonic Crystal Optical Waveguides," Journal of Lightwave Technology **18**, 1402–1410 (2000).

[6] A. Adibi, Y. Xu, R. K. Lee, A. Yariv, A. Scherer, "Properties of the Slab Modes in Photonic Crystal Optical Waveguides," Journal of Lightwave Technology **18**, 1554–1564 (2000).

[7] M. Loncar et. al., "Experimental and theoretical confirmation of Bloch-mode light propagation in planar photonic crystal waveguides," Applied Physics Letters **80**, 1689–169 (2002).

[8] Y. Desieres et. al., "Propagation losses of the fundamental mode in a single line-defect photonic crystal waveguide on an InP membrane," Journal of Applied Physics **92** 2227–2234 (2002).

[9] X. Letartre et. al., "Group velocity and propagation losses measurements in a single-line photonic-crystal waveguide on InP membranes," Applied Physics Letters **79**, 2312–2314 (2001).

[10] S. Kuchinsky, D.C. Allan, N.F. Borelli, J.-C. Cotteverte, "3D localization in a channel waveguide in a photonic crystal with 2D periodicity," Optics Communications bf 175, 147–152 (2000).

[11] A. Mekis, J. C. Chen, I. Kurland, S. Fan, P. R. Villeneuve, J. D. Joannopoulos, "High Transmission through Sharp Bends in Photonic Crystal Waveguides," Physical Review Letters **77**, 3787–3789 (1996).

[12] E. Chow, S. Y. Lin, J. R. Wendt, S. G. Johnson, J. D. Joannopoulos, "Quantative analysis of bending efficiency in photonic-crystal waveguide bends at l = 1.55 μm wavelengths," Optics Letters **26**, 286–288 (2001).

[13] A. Talneau, L. Le Gouezigou, N. Bouadma, M. Kafesaki, C. M. Sokoulis, M. Agio, "Photonic-crystal ultrashort bends with improved transmission and low reflection at 1.55 μm," Applied Physics Letters **80**, 547–549 (2002).

[14] M. Tokushima, H. Kosaka, A. Tomita, H. Yamada, "Lightwave propagation through a 120° sharply bent single-line-defect photonic crystal waveguide," Applied Physics Letters **76**, 952–954 (2000).

[15] A. Chutinan, M. Okano, S. Noda, "Wider bandwidth with high transmission through waveguide bends in two-dimensional photonic crystal slabs," Applied Physics Letters **80**, 1698–1700 (2002).

[16] Y. Sugimoto et. al., "Experimental verification of guided mode in 60°-bent defect waveguides in AIGaAs-based air-bridge-type two-dimensional photonic crystal slabs," Journal of Applied Phyisics **91**, 3477-3479 (2002).

[17] C. C. Cheng and A. Scherer, "Fabrication of photonic band-gap crystals," Journal of Vacuum and Science & Technology B **13**, 2696–2700 (1995).

[18] E. Miyai, M. Okano, M. Mochizuki, S. Noda, "Analysis of coupling between two-dimensional photonic crystal waveguide and external waveguide," Applied Physics Letters **81**, 3729–3731 (2002).

[19] T. Weiland, "Time Domain Electromagnetic Field Computation with Finite Difference Methods," International Journal of Numerical Modelling **9**, 295–319 (1996).

[20] S.G. Johnson, J.D. Joannopoulos, "Block-iterative frequency-domain methods for Maxwell's equations in a planewave basis," Optics Express **8**, 173–190 (2001).

[21] J. Smajic, C. Hafner, D. Erni, "On the design of photonic crystal multiplexers," Optics Express **11**, 1378–1384 (2003).

Characterization of photonic crystal waveguides based on Fabry-Pérot interference

Iwan Märki, Martin Salt, Ross Stanley[*],
Urs Stauferand Hans Peter Herzig

University of Neuchâtel, Institute of Microtechnology,
Rue A.-L. Breguet 2, CH-2000 Neuchâtel, Switzerland

Abstract

We present two methods based on the analysis of Fabry-Pérot interference for a detailed characterization of a 90° corner in a two-dimensional photonic crystal waveguide fabricated in a thin Si membrane. These methods are a means of identifying the critical waveguide elements in the process of improving photonic crystal devices. The effects of the elements forming the photonic crystal waveguide are identified and quantified by means of a stage-by-stage analysis. By Fourier transforming the transmission spectra we observe the amount of light that is back-reflected inside the waveguide and based on the fringe contrast of the Fabry-Pérot modulation we calculate the loss contribution of each waveguide element, such as the tapers and the 90° corner.

DOI: 10.1063/1.1810204.

---

[*] Present address: CSEM, Centre Suisse d'Electronique et de Microtechnique SA, Rue Jaquet-Droz 1, CH-2007 Neuchâtel.

1 Introduction

Photonic crystals are periodic structures that provide a great potential for controlling the propagation of light and permit further miniaturization of optical devices [1–10]. Waveguides and waveguide bends can be created for frequencies inside the photonic band gap by introducing line defects into the photonic crystal structure [11–16]. A sharp bend in a photonic crystal, potentially a key component for integrated photonic circuits, provides an opportunity to study the optical characteristics of photonic band gap structures. In this paper, we present two methods based on the Fabry-Pérot interference technique [17] for a detailed and stage-by-stage experimental analysis of light propagation around a 90° bend in a photonic crystal slab. Transmission spectra of samples with different designs are compared for a better understanding of the transmission efficiency. This analysis allows the study of the effects induced by the different elements of the photonic crystal waveguide. By performing a Fourier transform on the transmission spectra, regions in the waveguide where reflections occur are identified. The losses in all the waveguides are evaluated by calculating the loss coefficient, a very important parameter.

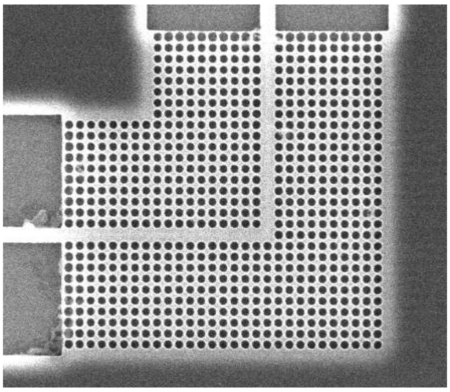

Figure 1: Scanning electron microscope image of the 90° bend photonic crystal waveguide.

The photonic crystal consists of a square array of cylindrical air holes in a thin Silicon membrane surrounded by air (Fig. 1). The structure is designed to give rise to a TE-like (in-plane polarization) photonic band gap around $\lambda \sim 1.5\ \mu$m. The design parameters of the photonic crystal structure are the lattice constant $a = 496$ nm, the hole radius $r = 190$ nm and the slab thickness $t = 290$ nm. Measurements are performed with an optical setup that includes a tunable laser source ranging from 1440 nm to 1580 nm.

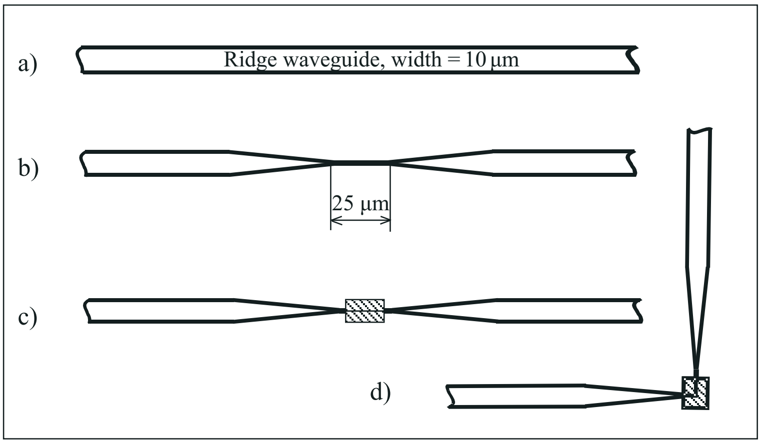

Figure 2: Designs of the fabricated waveguides: (a) straight waveguide (width=10 μmm); (b) straight waveguide with taper and narrow width section (width=500 nm); (c) straight waveguide with photonic crystal waveguide (photonic crystal waveguide length=25 μm); and (d) waveguide with 90° bend.

2 Transmission efficiency

In order to study the effects induced by the taper, the ridge waveguide to photonic crystal waveguide interface and the photonic crystal sections, we fabricated a series of samples that represent the different sub-elements of a final photonic crystal bend sample. This allows a better understanding of how each element contributes to the final photonic crystal bend spectrum. The first design is a straight multimode waveguide (Fig. 2(a)) on a SiO2 substrate with a width of 10 μm, a thickness of 290 nm and an overall length of 2 mm. It serves as reference for the computation of the transmission efficiency [12]. The second design is a straight waveguide with a taper (Fig. 2(b)) that reduces the width to 500 nm, a ridge waveguide section of a length of 25 μm in the middle and again a taper to increase the width to 10 μm. The length of the two tapers is 75 μm each. The 25 μm middle waveguide section is a free-standing membrane and its width (500 nm) is approximately equal to the width of the photonic crystal waveguide defect channel (a=496 nm). This second design allows us to observe the influence of the taper-induced modal conversion. The next stage is the insertion of the photonic crystal containing a straight single line defect (no holes) into the middle of the waveguide (Fig. 2(c)). The photonic crystal section is a free-standing membrane and has a length of 20 μm. It allows us to study the effect of the modal mismatch between the ridge waveguide and the photonic crystal waveguide [18, 19] as well as losses created by the crystal. Finally, the 90° bend is introduced into the photonic crystal waveguide section (Fig. 2(d)).

3 Reflections and loss calculations

All the measured transmission spectra of the different waveguide types exhibit a characteristic Fabry-Pérot interference pattern (shown in the inset of Fig. 3), which is mostly due to the smooth end-facets and which will be discussed in detail in the next section. To obtain the approximate transmission efficiency of the different waveguides, shown in Fig. 3, we first remove numerically the periodic Fabry-Pérot interference pattern and secondly, we divide the transmission spectra by the spectrum of the straight reference waveguide for normalization. This eliminates extrinsic effects of the end-injection and most of the spectral response of the measurement optics. Repeated transmission measurements have confirmed that the experimental set-up is sufficiently stable to validate the used normalization method. The remaining error is therefore due to fabrication-induced variations between the different waveguides. A transmission efficiency of nearly 85% (±10%), which includes ridge waveguide to photonic crystal losses, is observed for the 90° bend waveguide at a frequency of 1.957×10^{14} Hz. It has a bandwidth of Δf $\approx$2700 GHz for a transmission efficiency of more than 60%. The measured transmission efficiency compares relatively well to the general shape and values of the 3D simulations, which have been presented in Ref. [19]. A detailed modal analysis of the different waveguide types is also presented in Ref. [19].

All back-reflections in the waveguide introduce a spectral Fabry-Pérot interference pattern related to the path length between reflecting points. Thus, the Fourier transform of the transmission spectra allows the identification of the points where reflections occur [20]. Fig. 4 shows the Fourier transform of the different waveguides, which all indicate a dominating Fabry-Pérot interference. This dominant peak corresponds to a Silicon path length of about 2 mm, and therefore is the Fabry-Pérot effect created by the end facets. Our three-dimensional simulations [21] have shown that about 38% of the light is reflected at the silicon/air interface of each end face. For the design containing the straight photonic crystal waveguide section (Fig. 4(c)), a small second Fabry-Pérot interference appears, which is attributed to the waveguide half-length (1 mm) less half the length of the photonic crystal section (10 μm), i.e., $\approx$1 mm. This suggests the presence of some reflection at the interface between the ridge waveguide and the photonic crystal waveguide section. The much smaller height of the second Fabry-Pérot interference peak in comparison to the first Fabry-Pérot interference peak indicates that the reflection at the interface between the ridge waveguide and the photonic crystal waveguide section is much smaller than the reflection at the end-facets (38%). The quantification of the second reflection from the relation between the height of the Fabry-Pérot interference peaks is difficult due to too many unknown parameters such as scattering and radiation. However, our three-dimensional numerical simulations have shown a reflection of 1%–5% at the interface between

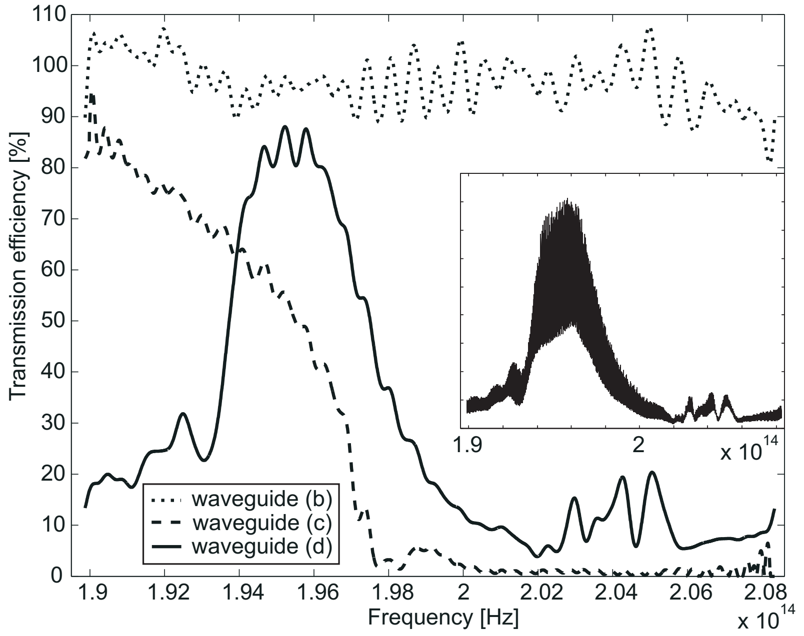

Figure 3: Transmission efficiency calculated from the measured transmission spectra in reference to the ridge waveguide with a width of 10 μm. The rapid fluctuations are due to interference in the optical system that has not been eliminated in the filtering and normalizing process. The Fabry-Pérot interference pattern corresponding to the total length of the waveguide is shown in the inset. The key corresponds to the different waveguide types shown in Fig. 2. The straight waveguide with the tapered section [waveguide (b)] exhibits a relatively flat transmission spectrum. The straight photonic crystal waveguide (waveguide (c)) exhibits a characteristic cut-off which corresponds to the mini stop band edge. The corner waveguide (waveguide (d)) shows a transmission band with a bandwidth of 2.7 Mhz for a transmission efficiency of more than 60%.

the ridge waveguide and the photonic crystal waveguide section. Therefore, we can conclude that in the high transmission efficiency range the coupling between the ridge waveguide and the photonic crystal waveguide is quite efficient. In the case of the 90° bend waveguide the secondary Fabry-Pérot interference generated by the Fourier transform over the whole transmission spectrum is about three times as strong as for the straight photonic crystal waveguide. This indicates back-reflections at the corner added to the previously observed reflection at the interface between the ridge waveguide and the photonic crystal waveguide. The difference in the path length of the reflection at the waveguide to photonic crystal interface and the reflection at the corner is too small to distinguish the two different peaks in the Fourier transform. At most one can observe a slight broadening of the peak corresponding to the path length of about the half-length of the waveguide. For a detailed understanding of these back-reflections at the corner,

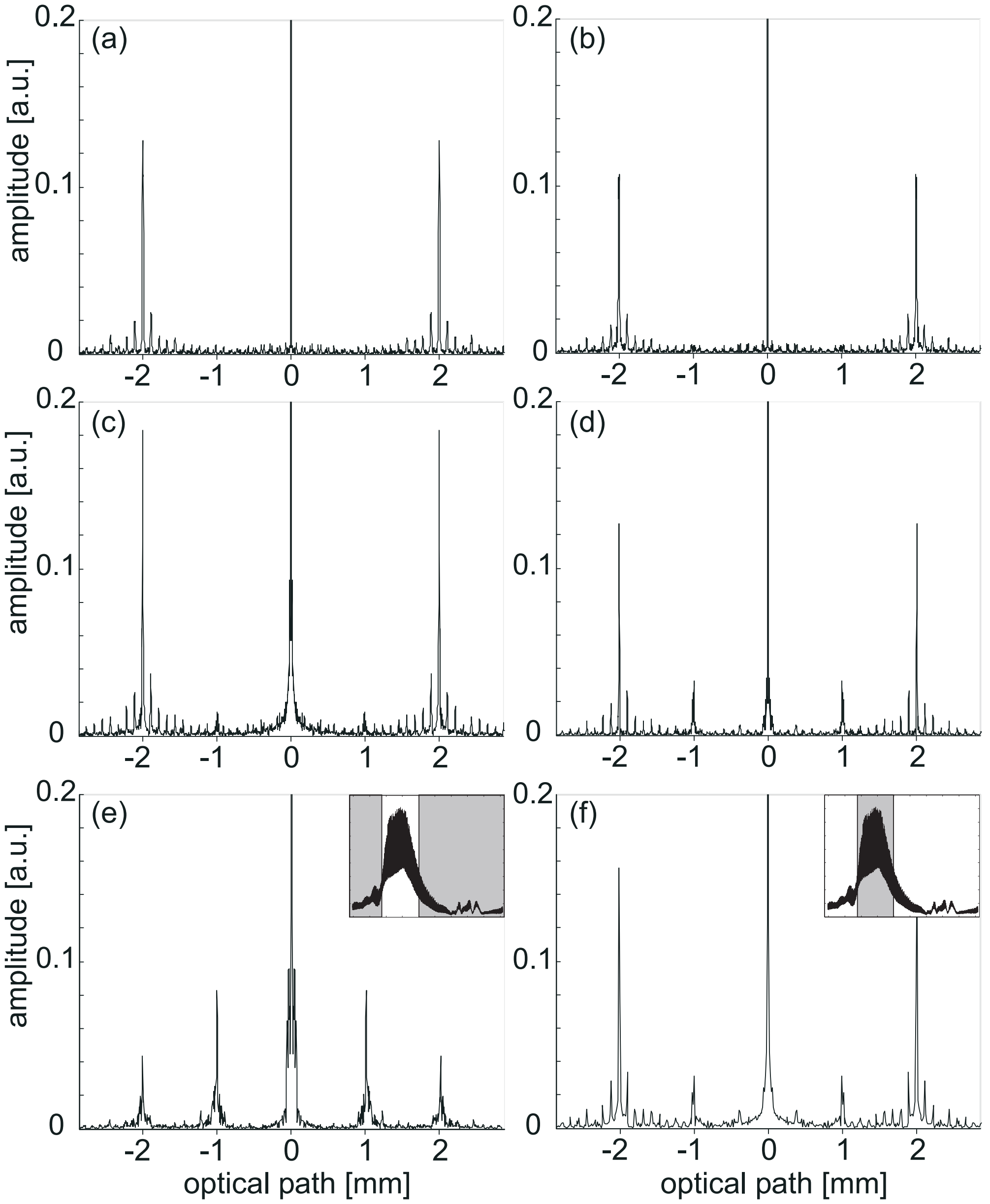

Figure 4: Fourier transform of the measurement data from the different waveguides: (a) straight waveguide; (b) straight waveguide with taper and narrow section; (c) straight waveguide with photonic crystal waveguide; (d) waveguide with 90° bend; (e) waveguide with 90° bend for frequency ranges where the transmission efficiency is low (indicated dark region in the inset); (f) waveguide with 90° bend for frequency ranges where the transmission efficiency is high (indicated dark region in the inset).

we divide the transmission spectrum into different sections and take the Fourier transform thereof (shown in Fig. 4(e) and 4(f)). On the one hand, we observe that, for frequency ranges where the transmission efficiency is low, the Fabry-Pérot peak corresponding to the backreflection at the corner is greater than the peak corresponding to the end-facet reflection. In this case, most of the light is reflected at the corner. On the other hand, for the frequency range where the transmission efficiency is high, the backreflection at the corner is low and most of the light travels around the corner. The numerically calculated backreflection at the corner in the case of high transmission is about 1%–5%. In the case of low transmission about 50%–72% of the light is reflected at the corner, depending on the amount of light that is scattered out of the photonic crystal waveguide.

Additional information can be taken from the fringe contrast of the Fabry-Pérot modulation in the measured transmission spectrum. Based on the fringe contrast, it is possible to evaluate the losses in the waveguide. Considering our waveguides as simple resonators with losses, we introduce the round-trip intensity attenuation factor [22], which is related to the two mirror reflectivities (end facets) and the absorption coefficient of the medium associated with both optical absorption and radiation loss:

$$r^2 = R_1 R_2 e^{-2\alpha_s}, \tag{1}$$

where $R1$ and $R2$ represent the end-facet reflectivities, d the total waveguide length of 2 mm, and $alpha_s$ the absorption coefficient. The maximum and minimum intensity (fringe contrast) observed in the measured transmission spectrum is related to the attenuation factor as follows:

$$\frac{I_{max}}{I_{min}} = \frac{(1+r)^2}{(1-r)^2}. \tag{2}$$

Using the two relations, we can solve for the absorption coefficient:

$$\alpha_s = \frac{ln(\frac{\sqrt{R_1 R_2}(\sqrt{I_{max}} - \sqrt{I_{min}})}{(\sqrt{I_{max}} + \sqrt{I_{min}})})}{d}. \tag{3}$$

The loss contribution of each element of the bend waveguide can now be calculated, assuming zero material absorption and that the calculated end-facet reflectivities of 38% are not significantly wavelength dependent in our measurement range. In Fig. 5 we show the calculated overall loss for the different waveguides. The straight reference waveguide shows an overall loss of between 8 and 9 dB for the entire measurement range. Considering the waveguide length of 2 mm, we can estimate a relative loss of 4.5 dB/mm. As already observed from the transmission efficiency, the loss calculation of the waveguide with taper confirms that practically no significant losses are induced by the taper. Compared to the reference

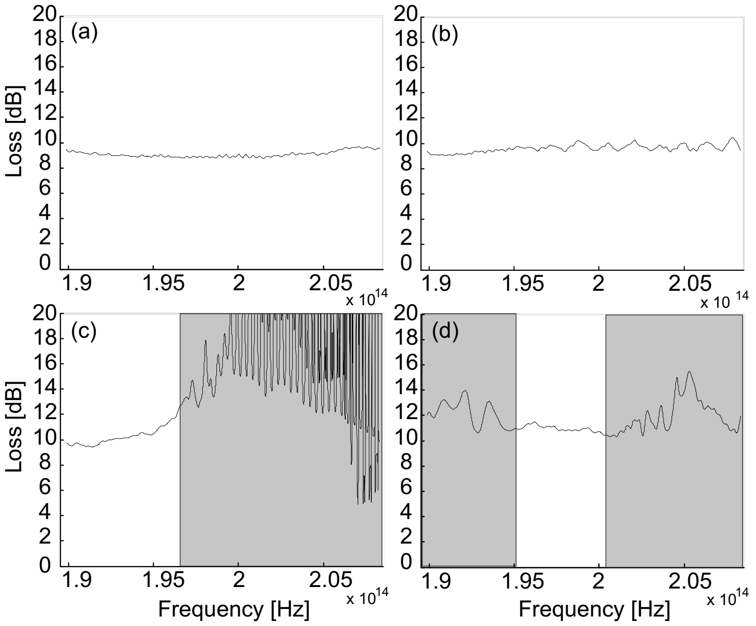

Figure 5: Calculated overall loss of the different waveguides: (a) simple straight waveguide; (b) straight waveguide with taper and narrow section; (c) straight waveguide with photonic crystal waveguide; (d) waveguide with 90° bend. The grey regions indicate the frequency ranges where the loss calculation is not valid.

waveguide, we can attribute an approximate loss of up to 0.5 dB to the taper. For the straight photonic crystal waveguide we observe in the frequency range below the cut-off between 0.5 and 2.5 dB of loss, which is due to the inserted photonic crystal waveguide section. Above the cut-off frequency the loss explodes and the applied loss calculation method looses its validity. The numerical noise above the cut-off frequency is due to a too small Fabry-Pérot fringe contrast. From the calculated loss corresponding to the photonic crystal waveguide section, we can estimate the relative loss coefficient of the defect guide. The section length of 20 μm leads to a relative loss coefficient of 25–125 dB/mm. Recently loss coefficients of 1 and 2.4 dB/mm have been reported [23, 24]. Lower quality of the fabricated photonic crystal structure can explain the higher loss coefficient. In addition, in Ref. 19 we have shown with a detailed modal analysis that the dispersion curve of the propagating defect mode is above the light line, which contributes significantly to the loss coefficient. Finally, the loss that can be attributed to the 90° bend waveguide adds up to between 1 and 2.5 dB in comparison to the reference waveguide for the high transmission frequency range. Comparing the 90° bend waveguide with the straight photonic crystal waveguide, we can estimate a loss of 0.5–2 dB due to the corner itself. It should be noted that the applied loss calculation method is valid only to a limited extent in the case of the 90° bend waveguide. As long as any reflections at points in between the end-facets are significantly small in comparison with the end-facet reflection, the loss coefficient can approximately be calculated from the Fabry-Pérot fringe contrast. However, in the previous section we have shown that considerable reflections at the corner occur for frequencies where the transmission efficiency is low. Therefore, in that case the applied loss calculation method is not valid.

4 Conclusion

In summary, we have presented simple methods for a detailed analysis of the light propagation around a 90° bend corner in a photonic crystal slab. The presented measurements show efficient waveguiding around a 90° corner and help to understand better the phenomena present in a waveguide containing a section of photonic crystal. Comparing the transmission spectrum of the different waveguide designs has made it possible to evaluate the influence of the sub-elements of the corner waveguide. We have shown that nearly 85% transmission efficiency was observed for the 90° bend waveguide. By means of the Fourier transform of the transmission spectra we have identified the points where reflections occur inside the waveguide. Based on the fringe contrast of the measured Fabry-Pérot modulation in the transmission spectrum, we have calculated the losses of the waveguides. The loss for the straight photonic crystal waveguide was estimated to be 25 dB/mm in the best case. The corner alone adds an estimated loss of 0.5–2dB for the frequency range where the transmission efficiency is high. The presented methods for the characterization of the photonic crystal waveguide help identify the critical waveguide elements that need improvement. For example, back reflections can be significantly reduced by introducing tapers for better light coupling. Waveguide sections with high losses need improvement by positioning the dispersion curve of the defect mode under the light line and by reducing the roughness of the sample surface.

5 Acknowledgements

The authors acknowledge F. Schädelin, S. Gautsch and P.-A. Künzi for useful discussions and for fabricating the photonic crystal waveguide samples. This work is funded under a joint projects program between the Swiss Center of Electronics and Microtechnology (CSEM) and the IMT-Uni Neuchâtel.

References

[1] S.G. Johnson, P.R. Villeneuve, S. Fan, J.D. Joannopoulos, "Linear waveguides in photonic-crystal slabs," Physical Review B **62**, 8212–8222 (2000).

[2] Loncar, J. Vuckovic, A. Scherer, "Methods for controlling positions of guided modes of photoniccrystal waveguides," J. Opt. Soc. Am. B **18**, 1362–1368 (2001).

[3] M.D.B. Charlton et. al., "Experimental investigation of photonic crystal waveguide devices and line-defect waveguide bends," Materials Science and Engineering B **74**, 17–24 (2000).

[4] S.Y. Lin, E. Chow, S.G. Johnson, J.D. Joannopoulos, "Demonstration of highly efficient waveguiding in a photonic crystal slab at the 1.5-μm wavelength," Optics Letters **25**, 1297–1299 (2000).

[5] M. Loncar, T. Doll, J. Vuckovic, A. Scherer, "Design and Fabrication of Silicon Photonic Crystal Optical Waveguides," Journal of Lightwave Technology **18**, 1402–1410 (2000).

[6] A. Adibi, Y. Xu, R. K. Lee, A. Yariv, A. Scherer, "Properties of the Slab Modes in Photonic Crystal Optical Waveguides," Journal of Lightwave Technology **18**, 1554–1564 (2000).

[7] M. Loncar et. al., "Experimental and theoretical confirmation of Bloch-mode light propagation in planar photonic crystal waveguides," Applied Physics Letters **80**, 1689–169 (2002).

[8] Y. Desieres et. al., "Propagation losses of the fundamental mode in a single line-defect photonic crystal waveguide on an InP membrane," Journal of Applied Physics **92**, 2227–2234 (2002).

[9] X. Letartre et. al., "Group velocity and propagation losses measurements in a single-line photonic-crystal waveguide on InP membranes," Applied Physics Letters **79**, 2312–2314 (2001).

[10] S. Kuchinsky, D.C. Allan, N.F. Borelli, J.-C. Cotteverte, "3D localization in a channel waveguide in a photonic crystal with 2D periodicity," Optics Communications bf 175, 147–152 (2000).

[11] A. Mekis, J. C. Chen, I. Kurland, S. Fan, P. R. Villeneuve, J. D. Joannopoulos, "High Transmission through Sharp Bends in Photonic Crystal Waveguides," Physical Review Letters **77**, 3787–3789 (1996).

[12] E. Chow, S. Y. Lin, J. R. Wendt, S. G. Johnson, J. D. Joannopoulos, “Quantative analysis of bending efficiency in photonic-crystal waveguide bends at l = 1.55 μm wavelengths,” Optics Letters **26**, 286–288 (2001).

[13] A. Talneau, L. Le Gouezigou, N. Bouadma, M. Kafesaki, C. M. Sokoulis, M. Agio, “Photonic-crystal ultrashort bends with improved transmission and low reflection at 1.55 μm,” Applied Physics Letters **80**, 547–549 (2002).

[14] M. Tokushima, H. Kosaka, A. Tomita, H. Yamada, “Lightwave propagation through a 120° sharply bent single-line-defect photonic crystal waveguide,” Applied Physics Letters **76**, 952–954 (2000).

[15] A. Chutinan, M. Okano, S. Noda, “Wider bandwidth with high transmission through waveguide bends in two-dimensional photonic crystal slabs,” Applied Physics Letters **80**, 1698–1700 (2002).

[16] Y. Sugimoto et. al., “Experimental verification of guided mode in 60°-bent defect waveguides in AIGaAs-based air-bridge-type two-dimensional photonic crystal slabs,” Journal of Applied Phyisics **91**, 3477–3479 (2002).

[17] A. Talneau, M. Mulot, S. Anand, Ph. Lalanne, “Compound cavity measurement of transmissionand reflection of a tapered single-line Photonic-Crystal waveguide,” Applied Physics Letters **82**, 2577–2579 (2003).

[18] E. Miyai, M. Okano, M. Mochizuki, S. Noda, “Analysis of coupling between two-dimensional photonic crystal waveguide and external waveguide,” Applied Physics Letters **81**, 3729–3731 (2002).

[19] I. Märki, M. Salt, and H. P. Herzig, “Practical and theoretical modal analysis of photonic crystal waveguides,” Journal of Applied Physics **96**, 7–11 (2004).

[20] A. Talneau, Ph. Lalanne, M Agio, and C. M. Soukoulis, “Low-reflection photonic-crystal taper for efficient coupling between guide sections of arbitrary widths,” Optics Letters **27**, 1522–1524 (2002).

[21] T. Weiland, “Time Domain Electromagnetic Field Computation with Finite Difference Methods,” International Journal of Numerical Modelling **9**, 295–319 (1996).

[22] B. E. A. Saleh und M. C. Teich, *Fundamentals of Photonics* (Wiley, New York, 1991).

[23] M. Notomi, A. Shinya, S. Mitsugi, E. Kuramochi, and H.-Y. Ryu, “Waveguides, resonators and their coupled elements in photonic crystal slabs,” Optics Express **12**, 1551–1561 (2004).

[24] S. McNab, N. Moll, and Y. A. Vlasov, "Ultra-low loss photonic integrated circuit with membrane-type photonic crystal waveguides," Optics Express **11**, 2927–2939 (2003).

Characterization of buried photonic crystal waveguides and microcavities fabricated by deep ultraviolet lithography

Iwan Märki, Martin Salt, and Hans Peter Herzig
University of Neuchâtel, Institute of Microtechnology,
Rue A.-L. Breguet 2, CH-2000 Neuchâtel, Switzerland

Ross Stanley
Centre Suisse d'Electronique et de Microtechnique (CSEM), SA,
Rue Jaquet-Droz 1,CH-2007 Neuchâtel, Switzerland

L. El Melhaoui, P. Lyan, and J. M. Fedeli
Laboratoire d'Electronique de Technologie de l'Information,
Commissariat à l'Energie Atomique (CEA)-Grenoble,
17 rue des Martyrs, 38 054 Grenoble Cedex 9, France

Abstract

We present results of the optical characterization of silicon photonic crystal waveguides and microcavities that are completely buried in a silicon dioxide cladding and are fabricated by deep ultraviolet (UV) lithography. The advantages of buried waveguides and deep UV-lithography are discussed. Transmission spectra and loss factors for photonic crystal waveguides, as well as quality factors for resonant microcavities are obtained. The observed characteristics are in good agreement with the three-dimensional simulations.

DOI: 10.1063/1.1948507.

1 Introduction

Photonic crystal structures are becoming important building blocks for providing exciting ways to control light and to permit further miniaturization of optical devices. Planar photonic crystals find their application for example in extremely small lasers, filters, multiplexers, optical switches and microcavities [1–4]. For research purposes e-beam lithography is the most used technique for the fabrication of such integrated optical circuits, because of its high resolution capabilities. However, it is expensive (per sample) and, due to its serial writing process, it is slow and therefore not suitable for mass production. Optical lithography provides the fabrication process for large volume but is limited in resolution by optical diffraction. With deep ultraviolet (UV) lithography both the resolution required to fabricate the photonic crystal structures and the parallel writing process needed for mass production have become available [5].

In this work we present the first investigation of a silicon slab photonic crystal waveguide (PCW) structure, which is completely buried in a silicon dioxide cladding. Photonic crystal structures made from SOI (silicon on insulator) wafers are more promising for large-scale integration because advanced CMOS fabrication technology, i.e. deep UV-lithography, can be used. Photonic crystal waveguides are basic elements for building integrated optical circuits. They carry the light to and from the functional part of the photonic crystal structure (e.g. filter or resonator). The lower the losses in the PCW, the better the performance of the photonic crystal structure with the specific functionality. So far, low-loss guiding has been demonstrated in suspended membrane and low-index bottom cladding structures [3, 6]. Our waveguide structures, fully buried in a silicon dioxide cladding, are protected from the environment and therefore much more practical for many applications. However, the lower refractive index contrast between the slab and the cladding makes it more difficult to achieve low-loss guiding and is a challenge during the design process. In fact, three dimensional simulations are essential in order to precisely model the losses.

We investigate a design of a resonant microcavity inside the photonic crystal waveguide. Resonant microcavities in photonic crystals are of great interest because they exhibit highly localized optical fields and narrow transmission bands and therefore can serve as basic elements for switches, filters and small lasers. Much effort has been spent by different groups in design and fabrication in order to improve the quality (Q) factor of microcavities. Q factors of up to 7300 have been reported for 2D crystal cavities with direct in-plane transmission measurements [3].

We report the design, fabrication and measurement of the structures. Based on the measurements we discuss the losses in the photonic crystal waveguide and the quality factor of the resonant cavity.

2 Design and fabrication

First, we propose a straight photonic crystal waveguide with a W1 defect line (one row of missing holes) as a basic building block. The photonic crystal consists of a triangular array of cylindrical holes in a thin Si slab. The Si slab is completely buried in silicon dioxide. Second, we propose a design of in-plane resonant cavity, which is formed by two identical Bragg reflectors and is situated inside the photonic crystal waveguide (see Fig. 1). The design parameters of the Bragg reflectors are different to those of the rest of the photonic crystal, thus increasing the design options for the cavity. The cavity structure is designed so as to obtain a highly localized field inside the cavity and high in-plane transmission for a narrow frequency band. In order to achieve a high Q factor and high in-plane transmission, the radiation losses, i.e. the modal mismatch at the interface between the photonic crystal waveguide and the cavity structure, need to be minimized by engineering the hole dimensions and positions of the Bragg reflectors during the design process. Several methods have been suggested for optimizing the performance of photonic crystal microcavities, including tapering [7], Bloch-wave engineering [8] or radiation losses recycling [9]. All these methods require a very high accuracy and quality for the fabrication. Being at the limit of the possible resolution with deep UV-lithography, we have kept the design as simple as possible while accepting lower performance for the photonic crystal cavity. The holes forming the Bragg reflectors are all equally spaced and have the same dimensions. A microcavity with four holes on both sides and a microcavity with five holes on both sides have been fabricated and measured.

The photonic crystal structures are fabricated by LETI (Laboratoire d'Electronique de Technologie de l'Information, France) using deep UV-lithography at a wavelength of 193 nm. After the lithography process, the patterns in the photoresist are transferred into the silicon layer of the SOI wafer using dry etching technology. As a final step, the etched structures in the silicon are then covered with an oxide layer.

3 Reflections and loss calculations

Measurements are performed with an optical setup that includes a tunable laser source. An aspheric lens is used to inject TE-polarized light (in-plane polarization) into a 10 μm-wide, 238 nm thick Silicon layer buried in silicon dioxide. The light is guided via a taper, which reduces the waveguide width to 0.5 μm, to the photonic crystal waveguide. In the case of the W1 waveguide the light is directly transmitted, whereas in the case of the microcavity the light couples into the resonant cavity for a narrow frequency band, where it is highly localized

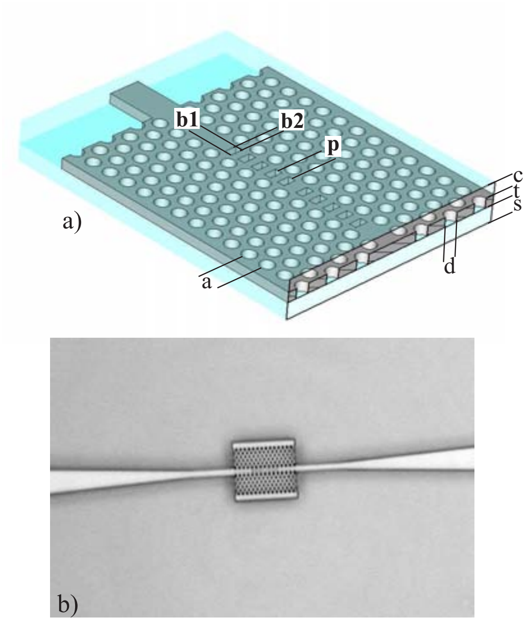

Figure 1: a) In-plane photonic crystal microcavity structure buried in silicon dioxide (PhC period a=490 nm, hole diameter d=350 nm, core thickness t=238 nm, bottom oxide thickness $s \approx 2000$ nm, upper cladding thickness $c \approx 700$ nm). The microcavity inside the photonic crystal waveguide is formed by two five-hole Bragg reflectors (hole dimensions $b1$=325 nm and $b2$=180 nm, period p=373 nm). b) Optical microscope image of the fabricated waveguide structure showing the tapered sections guiding the light to and from the photonic crystal microcavity.

and eventually transmitted. Using a second, identical taper the transmitted light is then guided to the exit of the device, where it is collected by a microscope objective and focused onto an InGaAs detector for measurements. The tunable laser source allows us to measure the transmission spectrum ranging from 1440 to 1590 nm.

The measured transmission spectra contain a dominant periodic Fabry-Pérot interference pattern (see Fig. 2), which corresponds to the total length of the waveguide system and is due to the reflections at the smooth waveguide end-facets. To obtain the approximate transmission efficiency of the photonic crystal waveguide and the resonant microcavity, we first remove numerically the Fabry-Pérot interference pattern from the measurement data by filtering the peak corresponding to the total waveguide length in the Fourier transformed spectrum. Second, we divide the transmission spectra by the spectrum of a straight reference waveguide for normalization. The reference waveguide has a width of 10 μm and a thickness of 238 nm, which corresponds exactly to the PC waveguide without tapered and photonic crystal sections. This eliminates extrinsic effects of the end

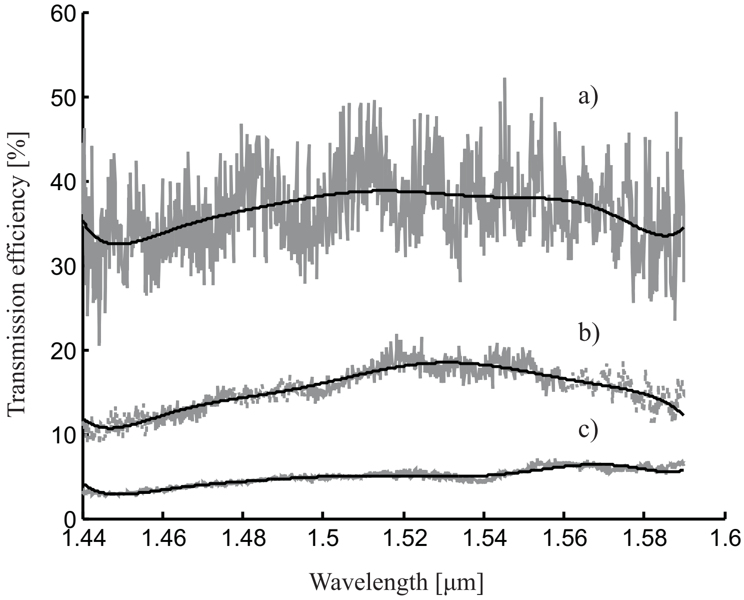

Figure 2: Filtered (black) and non-filtered (gray) normalized transmission spectra of three W1 waveguide samples of different lengths: a) 41a b) 81a and c) 161a, with a=490 nm. The oscillations in the nonfiltered transmission spectra are due to the reflections at the end-facets forming the periodic Fabry-Pérot interference pattern.

injection and most of the spectral response of the measurement optics.

In Fig. 2 we show the filtered and non-filtered normalized transmission spectra of three W1 waveguide samples of different lengths (41a, 81a and 161a, with a=490 nm). They exhibit an even transmission spectrum over the whole measurement range from 1440 nm to 1590 nm with a variation of ±10%. In the case of the shortest PCW (41a) about 35% of the light that is coupled from free space into the input end-face of the 10 μm-wide waveguide is transmitted. As mentioned above, the lower refractive index contrast between the slab and the cladding makes it more difficult to achieve low loss guiding. The computed dispersion diagram, shown in Fig. 3, illustrates the more limited possibilities for low loss guiding below the light line due to the oxide cladding. As comparison, the light line for an air cladding is indicated as well. The different guided defect modes, shown in Fig. 3, are represented by solid black lines. We observe that the present design does not posses a suitable propagating mode in the measurement range that is below the light line. Therefore, the longer the PCW the more light is leaking vertically. In fact, the contrast in the Fabry-Pérot interference pattern of the non-filtered transmission spectra is proportional to the averaged transmission efficiency (filtered value), indicating the loss induced by the PCW. In order to calculate the propagation losses we compare the different transmission efficiencies depending on the different lengths of the photonic crystal waveguides using the cutback method [10]. We obtained a propagation loss of 150 dB/mm. The transmission measurements have been repeated several times in order to confirm the obtained propagation loss value. Accordingly, the error is estimated to ±30dB/mm. In comparison, we have performed three dimensional simulations using a finite integration time domain (FITD) algorithm [11]. They have shown a propagation loss of 100 dB/mm, indicating that there are some extra losses in the real system, coming from e.g. surface roughness. By adequately changing the design of the PCW, such as the silicon slab thickness and the PC waveguide width, it is possible to shift the propagating mode into the limited region below the light line (see Fig. 3), which would allow non-radiative vertical guiding, i.e. a significant reduction in vertical loss. Improvements in fabrication such as higher accuracy in dimensions and smoother sidewalls will result in a reduction of the scattering losses. In addition, based on the propagation loss we estimate the losses at the interface between the conventional waveguide and the photonic crystal waveguide to be about 35%. These losses can be reduced by varying the width of the conventional waveguide [12] or by introducing a taper system [13] for a better mode matching.

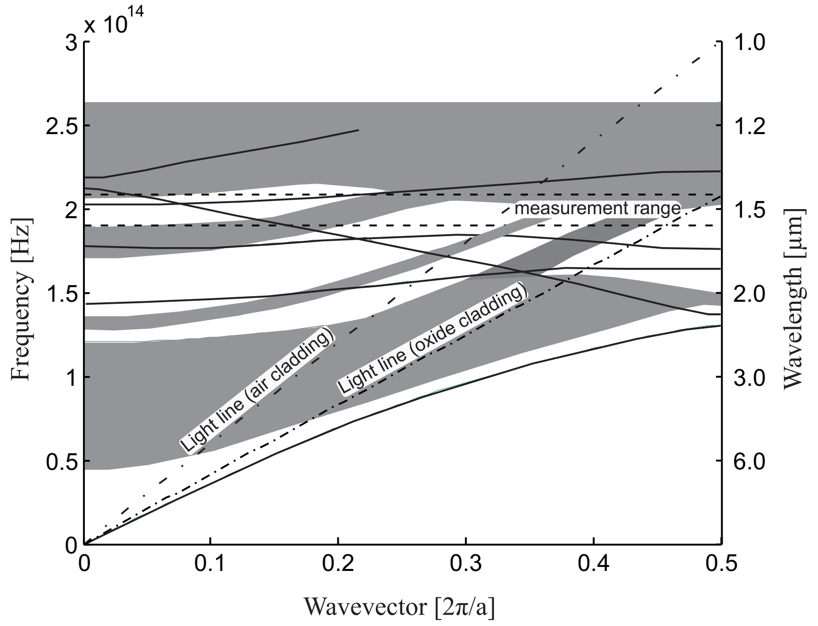

Figure 3: Dispersion diagram for TE-like guided modes in the W1 PC waveguide obtained by a fully three dimensional calculation based on a plane-wave expansion method. The defect modes are represented by solid black lines. The dark gray regions correspond to modes of the photonic crystal, which are states that can propagate through the crystal. The modes above the light line will leak energy into the cladding (leaky modes).

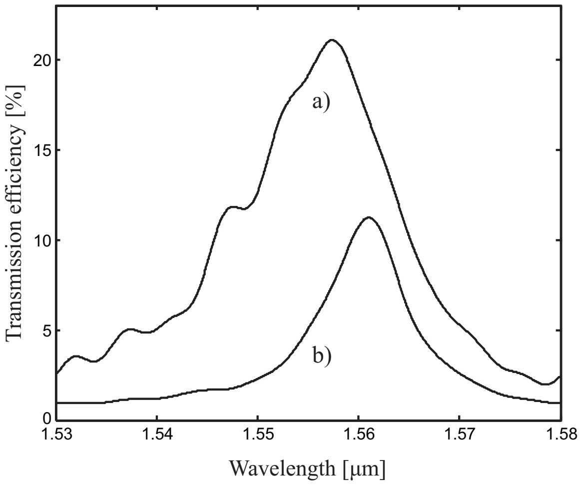

Figure 4: Measured transmission spectrum of a four-hole reflector cavity (a) and a five-hole reflector cavity (b). The raw measurement data has been filtered to remove the Fabry-Pérot interference.

In Fig. 4 we show the measured spectral response of two different in-plane resonant cavities inside the W1 PCW: One cavity with Bragg reflectors formed by four holes on both sides of the cavity and one cavity with Bragg reflectors formed by five holes on both sides of the cavity (Fig. 1). For the four-hole cavity we observe a transmission peak at λ ~1557 nm and an approximate maximum transmission efficiency at resonance of 21%. The measured quality factor Q~ $\lambda/\Delta\lambda_{FWHM}$ is equal to 100. The weak modulation on the left part of the spectrum is likely due to fabrication-induced non-uniformities in the cavity structure. Such modulations have also been observed in our three-dimensional simulations when varying the hole dimensions and positions of the Bragg reflectors inside the PCW. The transmission spectrum of the five-hole cavity is much narrower and more Lorentzian-like than the spectrum of the four-hole cavity. We observe an approximate maximum transmission efficiency of about 11% at a slightly higher peak wavelength (1562 nm) induced by a small increase in the effective cavity length due to the presence of the additional Bragg holes. The measured quality factor Q~ $\lambda/\Delta\lambda_{FWHM}$ is equal to 200. Thus, by adding one hole to the Bragg reflectors on both sides of the microcavity we can increase the quality by a factor of two, whereas the transmission efficiency is reduced by approximately that same factor.

In Fig. 5 we show the corresponding 3D simulated transmission efficiencies of the two different microcavities using the 3D finite integration time domain (FITD) algorithm [11]. The quality factor for the four-hole cavity is 240 and for the five-hole cavity is 440. The maximum transmission efficiencies are 41%

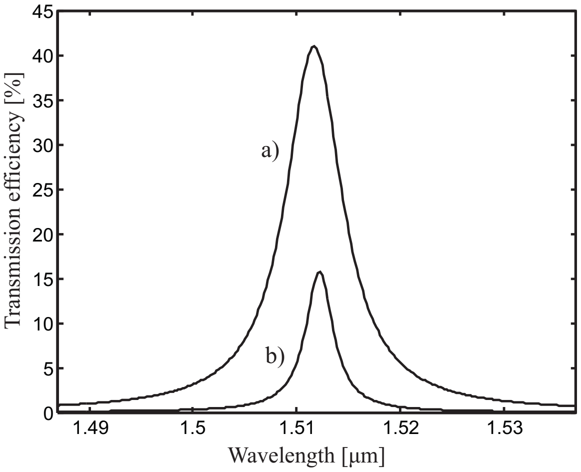

Figure 5: Simulated transmission efficiency of a four-hole reflector cavity (a) and a five-hole reflector cavity (b).

and 17% respectively. Compared to the measurements, the simulated values are about two times better. Additionally, we note the asymmetry and the higher resonant wavelengths in the measured transmission spectra. The observed differences between Fig. 4 and Fig. 5 are due to variations between the fabricated structure and the ideal simulated structure. Small defects, like variations in the hole dimensions or sidewall roughness, also induce higher losses, which cause a reduction in transmission and in the quality factor. However, despite the difference in the absolute values, the ratio between the two quality factors and the two maximum transmission efficiencies observed in the measured spectrum is in very good agreement with that of the simulated spectra. Our simulations have shown that by adding one hole to the reflectors on both sides of the microcavity, the reflectivity increases by 10%. Therefore, on the one hand the quality factor increases and on the other hand the transmission efficiency decreases because more light is either reflected back to the input end-face or scattered into the cladding.

Based on the loss calculation of the W1 waveguides, we can evaluate the losses induced by the microcavity. The losses attributed to the four-hole cavity and the five-hole cavity are in the order of 25% and 38%, respectively. These losses include scattered light and light that is reflected back to the input end-facet. With a modified design for the PC waveguide providing a propagating mode below the oxide cladding light line, the losses induced by the microcavity can as well be reduced. The quality factor of the microcavity can be improved by further increasing the reflectivity of these mirrors. However, the reflectors must be designed such as to allow efficient coupling between the photonic crystal waveguide mode and the resonant cavity mode. As mentioned earlier, this can be achieved by using different design methods.

4 Conclusion

We have investigated a W1 photonic crystal waveguide and a design of an in-plane resonant cavity completely buried in silicon oxide and fabricated by deep UV-lithography. On the one hand, the buried photonic crystal structure is well protected and therefore very promising for applications. On the other hand, the oxide cladding makes it more difficult to achieve low loss guiding. By changing the silicon slab thickness and the PC waveguide width it should be possible to achieve low loss guiding with a propagating mode below the light line. We have presented transmission measurements for PCW and cavities in silicon dioxide. For the W1 waveguide, a loss of 150 dB/mm has been measured. The quality factor for the resonant microcavities was measured to be about 100 for the four-hole cavity and about 200 for the five-hole cavity. The transmission measurements for the microcavities are in good agreement with the 3D FITD simulations. Further improvements to the maximum transmission efficiency and the quality factor of the resonant cavities can be achieved by optimizing the design of the photonic crystal waveguide and of the reflectors forming the microcavity.

Beside design optimization, our future investigations will focus on the strong localization of the optical field in a microcavity, which is sensitive to small perturbations and can lead to significant changes in the transmission properties. We have performed first experiments that will be shown elsewhere confirming that frequency tuning and modulation of the output-signal is possible with the presented resonant microcavities.

References

[1] A. Mekis, J. C. Chen, I. Kurland, S. Fan, P. R. Villeneuve, J. D. Joannopoulos, “High Transmission through Sharp Bends in Photonic Crystal Waveguides,” Physical Review Letters **77**, 3787–3789 (1996).

[2] S. Fan, P. Villeneuve, J. D. Joannopoulos, “Channel drop filters in photonic crystals,” Optics Express **3**, 4–11 (1998).

[3] M. Notomi, A. Shinya, S. Mitsugi, E. Kuramochi, and H.-Y. Ryu, “Waveguides, resonators and their coupled elements in photonic crystal slabs,” Optics Express **12**, 1551–1561 (2004).

[4] M. Loncar, T. Yoshie, A. Scherer, “Low threshold photonic crystal laser,” Applied Physics Letters **81**, 2680–2682 (2002).

[5] W. Bogaerts, D. Taillaert, B. Luyssaert, P. Dumon, J. Van Campenhout, P. Bienstman, D. Van Thourhout, R. Baets, “Basic structures for photonic integrated circuits in Silicon-on-insulator,” Optics Express **12**, 1583–1591 (2004).

[6] S. McNab, N. Moll, and Y. A. Vlasov, “Ultra-low loss photonic integrated circuit with membrane-type photonic crystal waveguides,” Optics Express **11**, 2927–2939 (2003).

[7] M. Palamaru, Ph. Lalanne, “Photonic crystal waveguides : Out-of-plane losses and adiabatic modal conversion,” Applied Physics Letters **78**, 1466–1468 (2001).

[8] Ph. Lalanne, Jean Paul Hugonin, “Bloch-wave enginieering for high Q’s, small V’s microcavities,” IEEE Journal of Quantum Electronics **39**, 1430–1438 (2003).

[9] Ph. Lalanne, S. Mias, J. P. Hugonin, “Two physical mechanisms for boosting the quality factor to cavity volume ratio of photonic crystal microcavities,” Optics Express **12**, 458–467 (2004).

[10] M. Notomi, A. Shinya, K. Yamada, J. Takahashi, C. Takahashi, I. Yolohama, “Structural tuning of guiding modes of line-defect waveguides of silicon-on-insulator photonic crystal slabs,” IEEE Journal of Quantum Electronics **38**, 736–742 (2002).

[11] T. Weiland, “Time Domain Electromagnetic Field Computation with Finite Difference Methods,” International Journal of Numerical Modelling **9**, 295–319 (1996).

[12] W. Kuang, J. D. O'Brien, "Reducing the out-of-plane radiation loss of photonic crystal waveguides on high-index substrates," Optics Letters **29**, 860–862 (2004).

[13] A. Talneau, M. Mulot, S. Anand, Ph. Lalanne, "Compound cavity measurement of transmissionand reflection of a tapered single-line Photonic-Crystal waveguide," Applied Physics Letters **82**, 2577–2579 (2003).

Observation of amplitude and phase in ridge and photonic crystal waveguides operating at 1.55 μm by use of heterodyne scanning near-field optical microscopy

P. Tortora
Institute of Microtechnology, University of Neuchâtel,
Rue A.-L. Breguet 2, CH-2000 Neuchâtel, Switzerland

M. Abashin
Dept. of Elect. and Computer Engineering, University of California, San Diego
9500 Gilman Drive, La Jolla, California 92093-0407

I. Märki, W. Nakagawa, L. Vaccaro, M. Salt, and H. P. Herzig
Institute of Microtechnology, University of Neuchâtel,
Rue A.-L. Breguet 2, CH-2000 Neuchâtel, Switzerland

U. Levy and Y. Fainman
Dept. of Elect. and Computer Engineering, University of California, San Diego
9500 Gilman Drive, La Jolla, California 92093-0407

Abstract

We apply heterodyne scanning near-field optical microscopy (SNOM) to observe with subwavelength resolution the amplitude and phase of optical fields propagating in several microfabricated waveguide devices operating around 1.55 μm wavelength. Good agreement between the SNOM measurements and predicted optical mode propagation characteristics in standard ridge waveguides demonstrates the validity of the method. In-situ observation of the subwavelength-scale distribution and propagation of optical fields in straight and 90° bend photonic crystal waveguides facilitates a more detailed understanding of the optical performance characteristics of these devices, as well as illustrates the usefulness of the technique for investigating nanostructured photonic devices.

OSICS codes: 040.2840, 120.5050, 180.5810, 230.7370.

Observation of amplitude and phase in ridge and photonic crystal waveguides operating at 1.55 μm by use of heterodyne scanning near-field optical microscopy

Photonic nanostructures, and in particular photonic crystals (PCs), provide a number of possibilities for developing novel devices based on near-field optical phenomena, as well as for monolithic integration of large-scale photonic systems [1–3]. However, as many of these devices depend on the subwavelength-scale localization of optical fields, traditional far-field characterization techniques are incapable of fully capturing the propagation characteristics of light in such structures. Scanning near-field optical microscopy [4, 5] (SNOM) provides the ability to observe directly the optical fields propagating in a photonic structure with sub-wavelength resolution, and has been applied to investigate photonic crystal resonators and various other devices [6, 7]. In heterodyne SNOM, light collected by the scanning probe is combined with a frequency shifted reference beam to enable simultaneous measurement of the local amplitude and phase of the probed field [8–10]. This technique has been used to characterize several devices, including periodically structured waveguides [11] and structured optical fibers [12], demonstrating the usefulness of SNOM for the detailed characterization of optical field propagation inside microstructured waveguides. In this letter, we apply this technique to investigate microfabricated ridge and PC waveguides and demonstrate the measurements of the phase and amplitude of the propagating fields in silicon-based photonic devices at the 1.55 μm wavelength [13]. The obtained results are in good agreement with predicted values, illustrating the viability of the technique as a method for investigating the complex amplitude of optical fields as they propagate inside the waveguides, and could have a significant impact on the understanding and development of nanostructured optical devices.

In the present set-up, the source is a semiconductor cw laser operating in a wavelength band around 1.55 μm. The cantilevered tapered fiber probe has an aperture of 200 nm and is scanned in tapping mode. This scanning technique reduces lateral interaction forces and is particularly advantageous for the investigation of silicon membranes or other fragile samples having abrupt topographical changes.

First, we characterize a standard ridge waveguide. This device is fabricated using an SOI wafer, with an approximately 290 nm thick silicon guiding layer on a 1 μm thick oxide layer. The waveguide structure consists of 10 μm wide input and output sections, a 0.5 μm wide section at the center, and linearly tapered sections in between to connect them. The oxide separation layer under the thin central section of the waveguide is undercut, resulting in an air-bridge structure.

The detected topography, amplitude, and phase for 1.55 μm light with polarization orthogonal to the substrate plane propagating in a 25 μm long segment of the wide section of the waveguide are shown in Fig.1. Comparison of the amplitude map (Fig.1b) with the topography (Fig.1a) clearly shows a good confinement of the light in the waveguide region. The phase map (Fig.1c) confirms

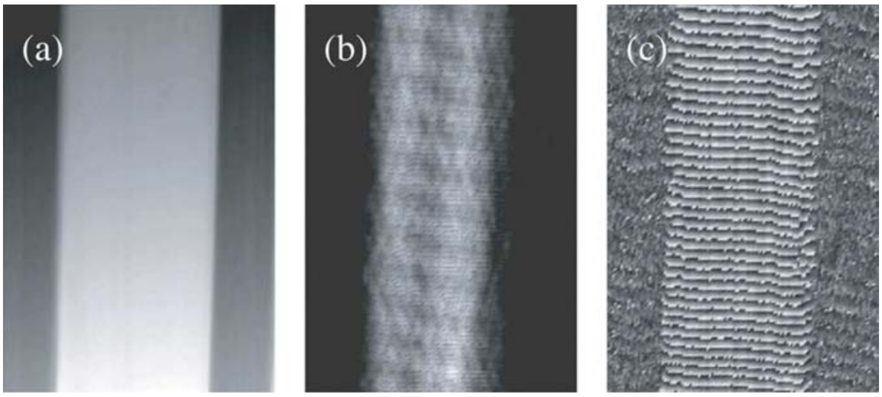

Figure 1: SNOM images of a 25 μm long segment of the wide (10 μm width) section of the tapered ridge waveguide showing: (a) topography; (b) amplitude; (c) phase measurements.

the same observation and shows a planar phase front, indicating that most of the light propagates in the fundamental mode. The Fourier transform of the measured complex amplitude along the propagation direction shows the strongest frequency component-corresponding to the dominant propagating mode-to have an effective wavelength of approximately 0.57 μm, very close to the predicted value of 0.61 μm for the fundamental TM-like mode.

In Fig.2, we report measurements performed on the narrow air-bridge section of the waveguide. The topography (Fig.2a) shows that part of the ridge and the initial part of the output taper are included in the scan. The amplitude (Fig.2b) and phase (Fig.2c) images show that the light is once again well confined in the waveguide. The spacing of the phase fronts in the taper section (top portion of Fig.2c) can be seen to be different from in the air-bridge section. The periodic oscillations in the amplitude of Fig.2b are due to a Fabry-Pérot standing wave pattern in the waveguide. The Fourier transform of the complex amplitude data for the narrow waveguide section (excluding the taper) shows that the effective wavelength of the propagating mode is 0.77 μm. Numerical simulation of the waveguide design yields 0.76 μm for the effective wavelength. The excellent agreement between the predicted and measured optical propagation characteristics demonstrates the capability of this heterodyne SNOM to characterize photonic devices operating in the 1.55 μm wavelength regime.

Next, we apply the heterodyne SNOM to the characterization of PC waveguides. The PC lattice consists of a square array of microfabricated cylindrical holes in a thin silicon membrane surrounded by air. The design parameters of the PC structure are lattice constant $a = 496$ nm, hole radius $r = 190$ nm and slab

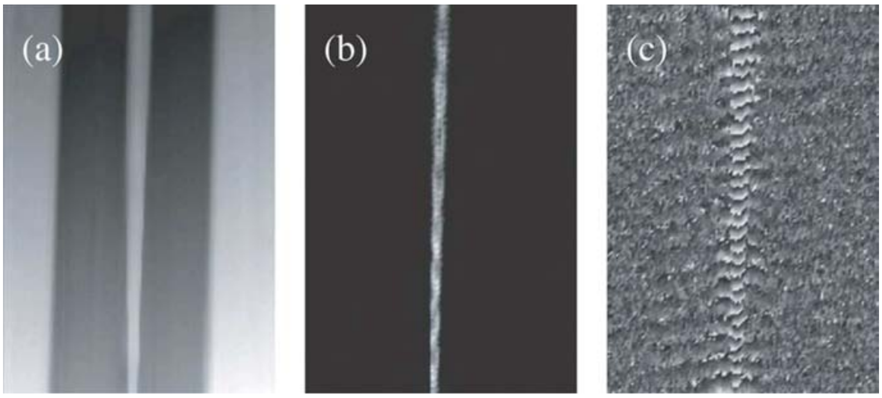

Figure 2: SNOM images of a 25 μm long segment of the tapered and air-bridge (0.5 μm width) sections of the ridge waveguide device showing: (a) topography; (b) amplitude; (c) phase measurements.

thickness $t = 290$ nm. These values are chosen to give rise to a TE-like (in-plane polarization) photonic band gap for wavelengths around 1.5 μm. The waveguide is formed by eliminating a single row of holes such that the propagating modes are confined within the defect. Two different PC devices are studied, a straight waveguide and a 90° bend. To facilitate injection of light into the waveguide, tapered ridge waveguides identical to the previous example are used.

The straight waveguide device, shown in Fig.1a, has a length of 30 mm. In previous work using this device, high transmission efficiency was measured in the wavelength range of 1530 to 1590 nm, efficient coupling from the ridge waveguide to the PC waveguide was observed, and the propagation loss in the PC waveguide was estimated to be on the order of 25 dB/mm [14, 15]. Using the heterodyne SNOM, we observe over an area of 14 μm square the amplitude and phase of light with wavelength 1560 nm propagating through the structure, as shown in Figs.1b and 1c, respectively. In the amplitude image we observe a confined propagating mode along the defect guide. A weak signal can be detected in the photonic crystal region around the defect guide indicating that a small amount of light is leaking into the photonic crystal. The phase image clearly shows a distinct phase front corresponding to the propagating mode inside the defect guide. The horizontal wavefront profile indicates that most of the light is propagating in the first defect mode having an even transverse symmetry, this being expected according to the modal analysis discussion in Ref. [15].

The last example is a PC waveguide with a 90° bend, as shown in Fig.4a. The measured amplitude and phase of light with wavelength 1550 nm propagating in the waveguide are shown in Figs.4b and 4c, respectively. Good confinement of the

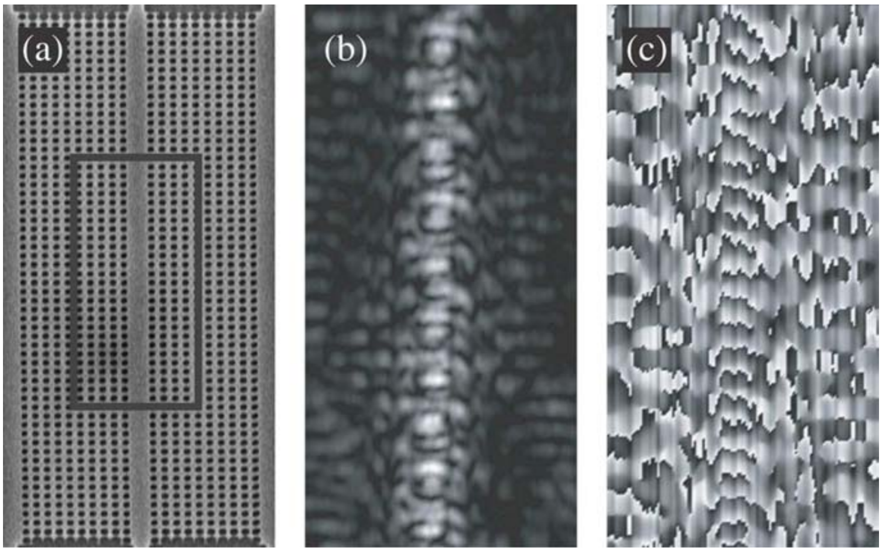

Figure 3: Straight PC waveguide: (a) top-view SEM image of the device (the square outline indicates the approximate SNOM measurement area); (b) SNOM amplitude measurement of the propagating mode in the waveguide over an area of 7 μm× 14 μm; (c) SNOM phase measurement.

light in the waveguide channel is observed in both straight waveguide segments. In addition, in the input arm of the device (propagating up from the bottom of the figure), the dominant mode corresponds to the first defect mode having an even transverse symmetry, while the more complex variations in the transverse field profile in the output arm suggest a superposition of multiple modes having even and odd transverse symmetry. Simulations have shown that coupling to higher order modes in the PC corner occurs due to the broken symmetry at the corner [15]. Finally, in the region of the waveguide bend, significant penetration of the light into the photonic crystal lattice is observed. A significantly higher amplitude signal is detected by the SNOM in this region due to two mechanisms: first, the corner region acts as a resonant cavity, resulting in a significantly higher field amplitude inside; and second there is significantly greater leakage or scattering of light from the vicinity of the corner, as compared with the straight waveguides. These preliminary measurements on the PC waveguides demonstrate the capabilities of the technique, however, a more complete investigation of the optical propagation characteristics in such structures requires further study.

We have demonstrated the direct observation of the amplitude and phase of an optical field propagating in ridge and PC SOI-based waveguides for wavelengths around 1.55 μm using heterodyne SNOM. These results are consistent

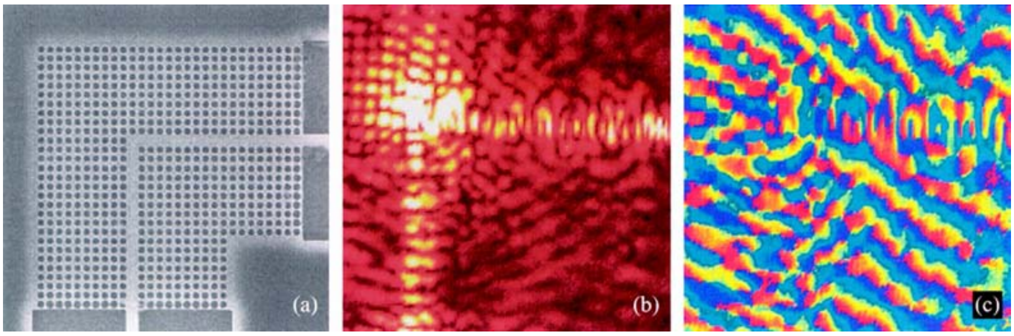

Figure 4: Images of the PC waveguide 90° bend structure: (a) SEM; (b) SNOM amplitude; (c) SNOM phase.

with predicted values from previous numerical or far-field experimental studies. These results also show the usefulness of the heterodyne SNOM as an investigative and diagnostic tool in the study of optical propagation in nanostructures, in particular in cases where subwavelength-scale and near-field effects are important. In the future, this technique can be applied to a wide range of PC and other nanostructure-based photonic devices, facilitating the improved understanding of nanoscale optical phenomena and the design and optimization of nanostructured photonic devices and systems.

The authors acknowledge assistance from R. Rotitski and K. Tetz (Departement of Electrical and Computer Engineering, University of California, San Diego) in adapting the SNOM system for the purposes of these measurements and thank F. Schädelin, S. Gautsch, U. Staufer, and N. F. de Rooij (Institute of Microtechnology, University of Neuchâtel) for the fabrication of the waveguide and photonic crystal samples. The authors also acknowledge the support of the NSF, DARPA, and the AFOSR, as well as the Swiss National Science Foundation.

References

[1] S. G. Johnson, A. Mekis, S. Fan, and J. D. Joannopoulos, “Molding the flow of light,” Computing in Science and Engineering **3**, 38–47 (2001).

[2] S. Noda, M. Imada, M. Okano, S. Ogawa, M. Mochizuki, and A. Chutinan, “Semiconductor three-dimensional and two-dimensional photonic crystals and devices,” J. Q. Electr. **38**, 726–735 (2002).

[3] M. Notomi, A. Shinya, S. Mitsugi, E. Kuramochi, and H.-Y. Ryu, “Waveguides, resonators and their coupled elements in photonic crystal slabs,” Optics Express **12**, 1551–1561 (2004).

[4] U. Dürig, D. W. Pohl, and F. Rohner, “U. Dürig, D. W. Pohl, and F. Rohner,” J. Appl. Phys. **59**, 3318–3327 (1986).

[5] H. Heinzelmann and D. W. Pohl, “Scanning near-field opti-. cal microscopy (SNOM),” Appl. Phys. A **59**, 89–101 (1994).

[6] K. Okamoto, M. Loncar, T. Yoshie, A. Scherer, Y. Qiu, and P. Gogna, “Near-field scanning optical microscopy of photonic crystal nanocavities,” Appl. Phys. Lett. **82**, 1676–1678 (2003).

[7] P. Kramper, M. Kafesaki, C. M. Soukoulis, A. Birner, F. Muller, U. Gosele, R. B. Wehrspohn, J. Mlynek, and V. Sandoghdar, “Near-field visualization of light confinement in a photonic crystal microresonator,” Opt. Lett. **29**, 174–176 (2004).

[8] M. L. M. Balistreri, J. P. Korterik, L. Kuipers, and N. F. van Hulst, “Local observations of phase singularities in optical fields in waveguide structures,” Phys. Rev. Lett. **85**, 294–297 (2000).

[9] A. Nesci, R. Dändliker, and H. P. Herzig, “Quantitative amplitude and phase measurement by use of a heterodyne scanning near-field optical microscope,” Opt. Lett. **26**, 208–210 (2001).

[10] S. I. Bozhevolnyi, and B. Vohnsen, “Near-field imaging of optical phase and its singularities,” Opt. Comm. **212**, 217–223 (2002).

[11] E. Flück, M. Hammer, A.M. Otter, J. P. Korterik, L. Kuipers, and N. F. van Hulst, “Amplitude and phase evolution of optical fields inside periodic photonic structures,” J. Lightwave Technol. **21**, 1384–1393 (2003).

Observation of amplitude and phase in ridge and photonic crystal waveguides operating at 1.55 μm by use of heterodyne scanning near-field optical microscopy

[12] J. C. Gates, C. W. J. Hillman, J. C. Baggett, K. Furusawa, T. M. Monro, and W. S. Brocklesby, “Structure and propagation of modes of large mode area holey fibers,” Opt. Express **12**, 847–852 (2004).

[13] A. Nesci, and Y. Fainman, “Complex amplitude of an ultrashort pulse with femtosecond resolution in a waveguide using a coherent NSOM at 1550 nm,” in Wave Optics and Photonic Devices for Optical Information Processing II, P. Ambs and F. R. Beyette, Jr., eds., Proc. SPIE **5181**, 62–69 (2003).

[14] I. Märki, M. Salt and H. P. Herzig, “Practical and theoretical modal analysis of photonic crystal waveguides,” Journal of Applied Physics **95**, 7–11 (2004).

[15] I. Märki, M. Salt, R. Stanley, U. Staufer, H. P. Herzig, “Characterization of photonic crystal waveguides based on Fabry-Pérot interferenc,” J. Appl. Phys. **96**, 6966–6969 (2004).

Near-field characterization of propagating optical modes in photonic crystal waveguides

Maxim Abashin
Dept. of Elect. and Computer Engineering, University of California, San Diego
9500 Gilman Drive, La Jolla, California 92093-0407

Pierpasquale Tortora and Iwan Märki
Institute of Microtechnology, University of Neuchâtel,
Rue A.-L. Breguet 2, CH-2000 Neuchâtel, Switzerland

Uriel Levy
Dept. of Elect. and Computer Engineering, University of California, San Diego
9500 Gilman Drive, La Jolla, California 92093-0407

Wataru Nakagawa, Luciana Vaccaro, and Hans Peter Herzig
Institute of Microtechnology, University of Neuchâtel,
Rue A.-L. Breguet 2, CH-2000 Neuchâtel, Switzerland

Yeshaiahu Fainman
Dept. of Elect. and Computer Engineering, University of California, San Diego
9500 Gilman Drive, La Jolla, California 92093-0407

Abstract

We analyze the propagating optical modes in a Silicon membrane photonic crystal waveguide, based on subwavelength-resolution amplitude and phase measurements of the optical fields using a heterodyne near-field scanning optical microscope (H-NSOM). Fourier analysis of the experimentally obtained optical amplitude and phase data permits identification of the propagating waveguide modes, including the direction of propagation (in contrast to intensity-only measurement techniques). This analysis reveals the presence of two superposed propagating modes in the waveguide. The characteristics of each mode are determined and found to be consistent with theoretical predictions within the limits of fabrication tolerances. An analysis of the relative amplitudes of these two modes as a function of wavelength show periodic oscillation with a period of approximately 3.3 nm. The coupling efficiency between the ridge waveguide and the photonic crystal waveguide is also estimated and found to be consistent with the internal propagating mode characteristics. The combination of high-sensitivity amplitude and phase measurements, subwavelength spatial resolution, and appropriate interpretive techniques permits the in-situ observation of the optical properties of the device with an unprecedented level of detail, and facilitates the characterization and optimization of nanostructure-based photonic devices and systems.

OSICS codes: (230.7370) Waveguides; (180.5810) Scanning microscopy.

1 Introduction

Since the first demonstrations of the near-field scanning optical microscope (NSOM) in 1984 [1, 2], the technique has proven to be an important tool for subwavelength resolution observation of various optical field configurations [3–5], including evanescent and other non-propagating fields [6–10]. A more recent innovation, the heterodyne NSOM (H-NSOM) [11], permits the near-field measurement of both amplitude and phase, providing previously inaccessible information about the optical fields under investigation. This technique has been applied to a large number of studies, in particular involving subwavelength-scale structures, localized optical field phenomena, and photonic crystals (PhCs) in the visible range [9, 12, 14].

With the recent rapid developments in optical fiber communications and semiconductor-based photonic devices and systems, there is a clear need for H-NSOM tools operating in the near infrared wavelength range. Although H-NSOM has only recently been adapted to this wavelength band, several interesting applications and results have already been reported [15–19]. In particular, for photonic devices based on subwavelength-scale features, such as photonic crystal structures, this technique is an indispensable diagnostic tool. Typically, characterization of such devices is carried out in the far field, by measuring the spectral response of the light that emerges from the structure. Instead, by measuring the optical fields as they propagate inside the device-with subwavelength resolution and with amplitude and phase information-H-NSOM provides significant additional information about the optical properties of the device [18, 19], and greatly facilitates both understanding the operation of the device and improving its performance. Furthermore, as manufacturing technology advances and photonic systems achieve higher degrees of complexity and integration, localized in-situ characterization of optical fields will become increasingly useful and necessary.

In a previous letter [20], we demonstrated the feasibility of measuring the amplitude and the phase of the propagating optical field in ridge and Silicon membrane PhC waveguides operating around 1550 nm wavelength using the H-NSOM technique. In this paper, we focus on a single example-a straight square-lattice Silicon membrane PhC waveguide-and perform a significantly more detailed analysis of the optical propagation characteristics of the device based on H-NSOM measurements. A detailed description of the H-NSOM tool (based on Nanonics MultiView 2000$^{\mathrm{TM}}$ System) that was used for these measurements is given in [16]. By comparing measurement results obtained for a range of optical wavelengths around 1550 nm, we determine a number of important characteristics concerning the propagating modes in the waveguide, including the number of propagating modes, their effective wavelength, their relative amplitudes, the position of the band edge, and the approximate input coupling efficiency as a function of wavelength. This information supports a much better understanding of the propagation of light within such a structure, enabling a detailed comparison of the experimental results with theoretical predictions. Overall, this investigation demonstrates the range of information provided by high-quality H-NSOM measurements, in many cases yielding insight that is unattainable using far-field optical characterization techniques.

In the next section we provide a brief description of the fabricated PhC waveguide sample and describe its expected properties from the calculated dispersion diagram. In section III we present experimentally obtained results validating the existence and the position of the PhC band edge. Section IV presents measurements of the complex amplitude for the propagating modes in the PhC waveguide, and the subsequent spectral analysis to determine the mode propagation properties. Section V is devoted to the measurement of input coupling loss at the interface of a single mode ridge waveguide and the PhC waveguide. Section VI concludes the manuscript.

2 Description of the PhC waveguide

The optical micrograph in Fig.1a shows the layout of the fabricated device, consisting of a pair of ridge waveguides coupled to the edges of a PhC waveguide. A square mesh PhC lattice with a period of 496 nm, air holes of radius 190 nm, and a membrane thickness of 290 nm (see Fig.1b) is used to create a W1 PhC waveguide by removing a single row of air holes (here W1 stands for PhC waveguide with one missing row of holes). The total length of the W1 PhC waveguide is about 25 microns. The device is fabricated in a silicon on insulator (SOI) wafer using electron beam lithography of PMMA resist for patterning, followed by reactive ion etching to transfer the pattern into the SOI substrate. The oxide layer below the PhC structure was removed using a buffered hydrofluoric acid vapor etch, thereby creating a PhC membrane. With this configuration a symmetric mode in the vertical direction can be obtained, and the radiation loss is reduced significantly.

To facilitate the injection of light into the device, two tapered ridge waveguides are coupled to the input and the output facets of the W1 PhC waveguide (See Fig.1). These tapered waveguides perform adiabatic mode conversion from 10-μm width to 500 nm width to allow single mode propagation and to better match the mode profile of the W1 PhC waveguide. Nevertheless, some loss is to be expected at the boundary between the ridge waveguide and the W1 PhC waveguide, due to mode mismatch. This issue will be further addressed in section 5.

The expected dispersion diagram for the TE-like modes of this PhC structure was numerically determined using a fully three-dimensional calculation based on

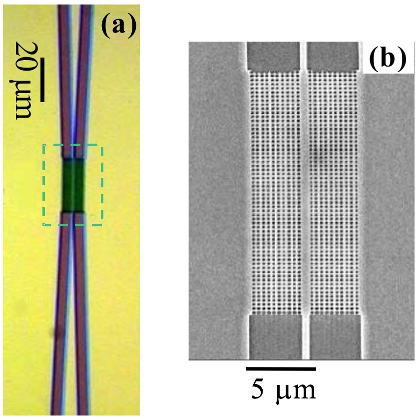

Figure 1: Description of the W1 PhC waveguide device: (a) optical micrograph showing the layout of the device, including the tapered waveguide and the W1 PhC waveguide. (b) Scanning electron micrograph (SEM) image of the region inside the dashed rectangle in (a). The W1 PhC waveguide is clearly observed.

a plane-wave expansion method [21]. The results of this analysis are summarized in Fig. 2: Solid black lines represent the guided defect modes (labeled e_1, e_2, e_3, and e_4). The dark gray shaded regions in Fig.2 represent modes that can propagate through the crystal. The light line is introduced in Fig.2 to define the boundary between the leaky and the propagating modes: modes above the light line leak energy whereas modes lying below the light line are confined in the membrane. The blue shaded region in Fig.2 shows the approximate measurement region.

The dispersion diagram of Fig.2 shows that in the measurement wavelength range we expect to excite two modes, labeled e_1 and e_2. The cutoff frequency for mode e_1 occurs at a normalized frequency of about 0.325, corresponding to a wavelength of about 1525 nm. The mode e_2 exists for the entire frequency range under study. However, for wavelengths shorter than about 1525 nm, the e_2 mode lies in the dark gray region, where PhC states are allowed, leading to leaking of the light from the waveguide into the PhC structure. In the following section we investigate experimentally these theoretical predictions.

3 Characterization of PC band edge

We first investigate the guided modes of the W1 PhC waveguide at a wavelength of 1560 nm, where we expect the light to be strongly guided in the waveguide channel. The H-NSOM system is used to measure amplitude and phase images

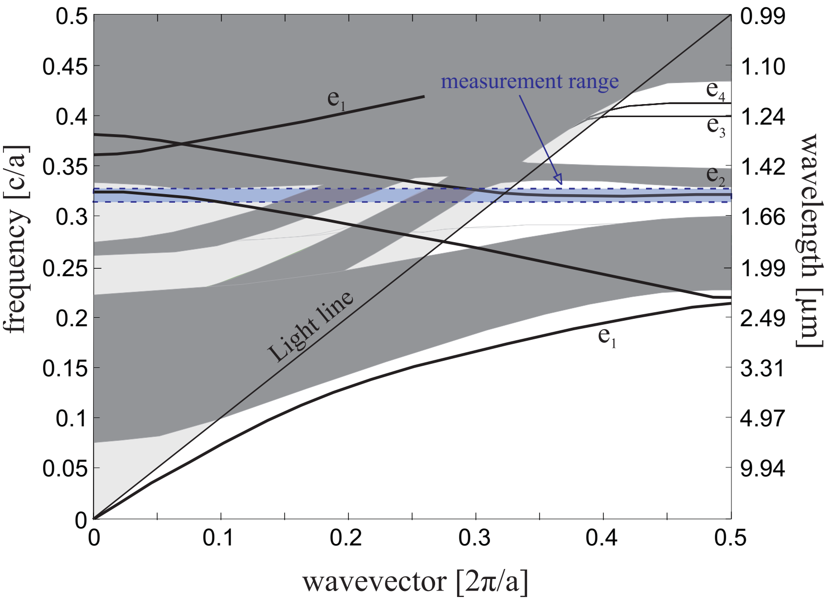

Figure 2: Calculated dispersion diagram for TE-like guided modes in the photonic crystal waveguide. Solid black lines represent the guided defect modes: e_1, e_2, e_3, and e_4. The dark gray shaded regions show modes that can propagate through the crystal. The light line defines the boundary between the leaky and the propagating modes. The blue shaded region shows the approximate measurement region centered at the wavelength of 1.5 μm.

of the W1 PhC waveguide following the procedures described in Ref. [9]: the light from a fiber-coupled tunable laser is split into two arms in a Mach Zehnder interferometric arrangement. One arm has a tapered fiber that is used to couple light into the cleaved edge of the fabricated device. An NSOM tip is introduced into the evanescent field just above the W1 PhC waveguide shown in Fig.1b. The optical field coupled into the NSOM tip is mixed with the light in the reference arm of the Mach-Zehnder interferometer and introduced into a photodetector followed by signal processing [9]. The NSOM tip is used to scan an area of 7×7 μm and the detected images are used to reconstruct the time-domain propagation of light, as shown in Fig.3. The results of Fig.3 show that the propagating light is well confined to the waveguide channel and has a predominantly stationary mode configuration. The movie was generated by adding for each frame a time-dependent phase to the measured phase, and taking the real part of the resulting complex amplitude. Such time-domain reconstruction of the optical field is only possible if amplitude and phase data are available.

We also investigate the excitation of modes well within the PBG and close to the edge of the PBG. As expected, at an optical frequency close to the edge of the

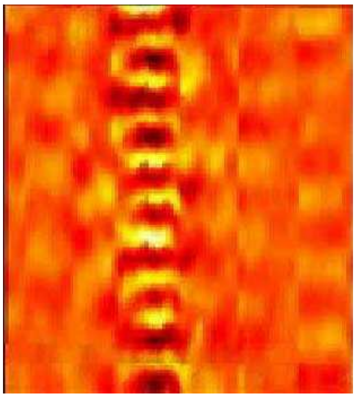

Figure 3: Optical field at wavelength of 1560 nm propagating in the W1 PhC waveguide as calculated from the measured complex amplitude. Scanning range is 7 by 7 microns.

PBG (corresponding to a wavelength of 1520.0 nm) the optical field is not strongly guided, as is clearly seen from the detected amplitude and phase images shown in Figs.4a and 4, respectively. In contrast, for a wavelength of 1560.0 nm (well within the PBG), the amplitude and phase images of Figs.4 and4, respectively, reveal well-guided optical propagation. The amplitude image (Fig.4) shows that the light is localized to the waveguide channel, and the phase image (Fig.4) shows planar phase fronts.

4 Photonic crystal waveguide modes

Next we perform detailed experimental measurements and analysis of the spectral modes propagating in W1 PhC waveguide, and compare these results with theoretical predictions.

4.1 NSOM measurement of waveguide spectral characteristics

The spectral measurement of the optical fields propagating in the W1 PhC waveguide is performed over optical frequencies within the bandgap, corresponding to a wavelength range of 1556.6 nm-1559.8 nm. Fig.5 shows nine representative images of the amplitude and phase data obtained using the H-NSOM at different wavelengths in this range (note that the amplitude and phase color keys are similar to those of Fig.4). It is evident from the results shown in Fig.5 that the propagating mode characteristics depend strongly on the wavelength. For example, at wavelength 1556.6 nm, the transverse profile of the propagating mode

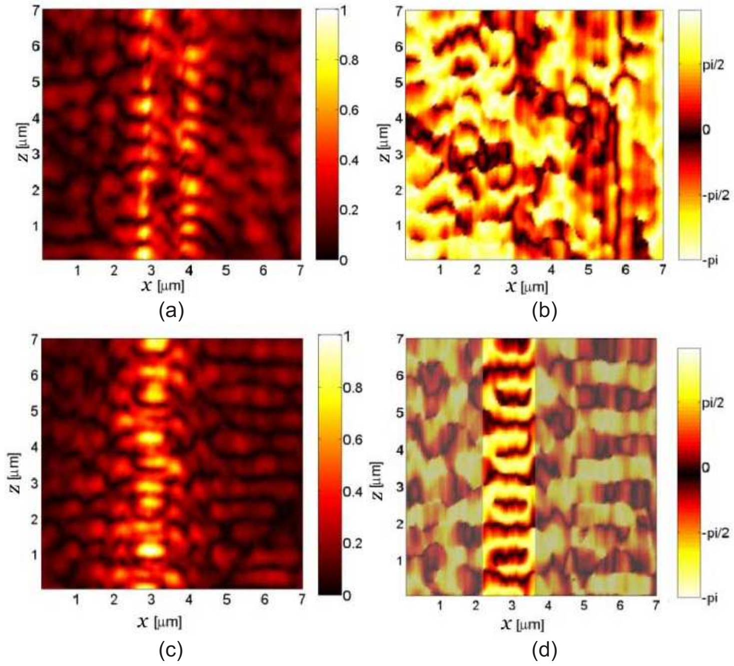

Figure 4: Images of measured amplitude and phase of the optical fields propagating in the W1 PhC waveguide at wavelengths of 1520 nm (a, b, respectively) and 1560 nm (c, d, respecitvely). Below the band edge (1520 nm) the propagating modes are not strongly confined to the waveguide channel, whereas modes within the bandgap of the PhC (1560 nm) demonstrate strong confinement of light in the waveguide channel (c) and planar phase fronts (d) in the waveguide region.

appears to be that of the fundamental mode-the amplitude has a single lobe with even transverse symmetry, and the phase fronts within the waveguide channel are flat along the transverse direction and uniformly spaced. Similar characteristics are observed again at wavelength 1559.8 nm. However, at a wavelength of 1558.2 nm (i.e., halfway between these two values), a very different profile with odd transverse symmetry is observed. Moreover, at intervening wavelengths (e.g. wavelengths between 1558.2 nm and 1559.8 nm) we see a gradual transition between the dominant even and odd mode structures. These results reveal a periodic variation of the propagating mode characteristics with respect to the optical frequency.

Next we exploit the unique advantage of the H-NSOM technique that provides the 2D complex amplitude information of the optical field for an operating device. Specifically, we perform a spectral analysis of the propagating modes at each excitation wavelength, thereby quantifying the modal power spectral density.

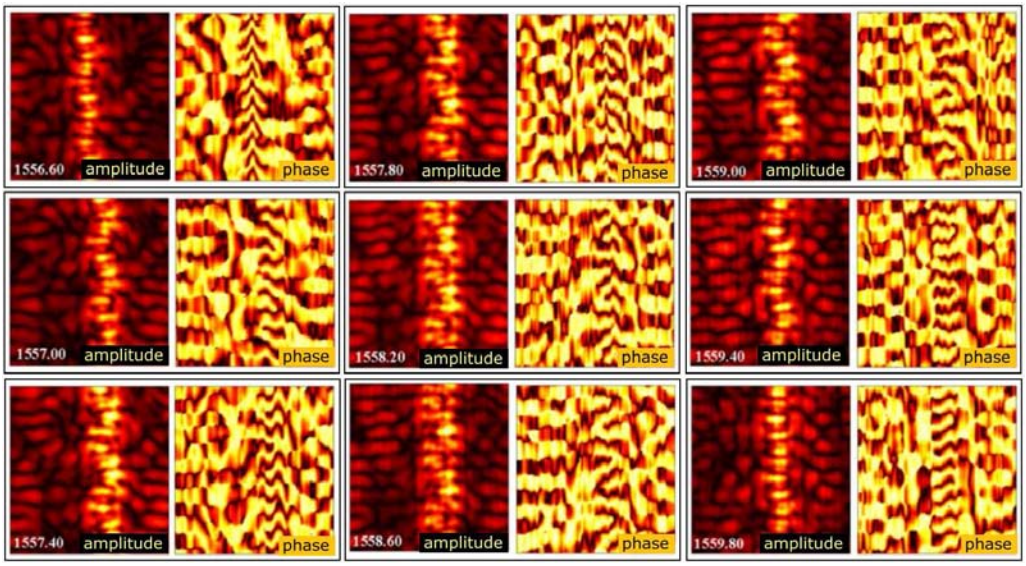

Figure 5: A sequence of amplitude and phase images of the guided modes in a W1 PhC waveguide measured for a sequence of wavelengths from 1556.6 nm to 1559.8 nm in increments of 0.4 nm. The images are obtained by scanning the H-NSOM tip over an area of 7×7 micrometers above the W1 PhC waveguide.

4.2 Complex-amplitude Fourier analysis

Detailed mode characteristics can be discerned by performing a Fourier analysis of the detected H-NSOM complex amplitude measurements. The ability to perform a Fourier transform operation on the measured near field complex amplitude data is clearly a significant advantage unique to the H-NSOM method in comparison to other existing techniques. For example, the available phase information allows us to calculate the propagation constant for each mode and to distinguish between forward and backward propagating fields. Since the light in the W1 PhC waveguide propagates along a specific direction, we can perform a one-dimensional Fourier transform along the propagation direction (i.e. the z-axis) to reveal the spatial frequency content of the complex amplitude. Fig.6 shows images of the resulting magnitude of the 1D Fourier transform applied to the complex amplitude of the optical field determined from the NSOM data, with the x-axis remaining in the spatial domain, and the z-axis replaced by the corresponding spatial frequency in the z-direction. The spectral images for wavelengths 1556.6 nm and 1558.2 are shown in Fig.6a and 6b, respectively. The peaks observed in these images are associated with the various modes propagating along the z-axis.

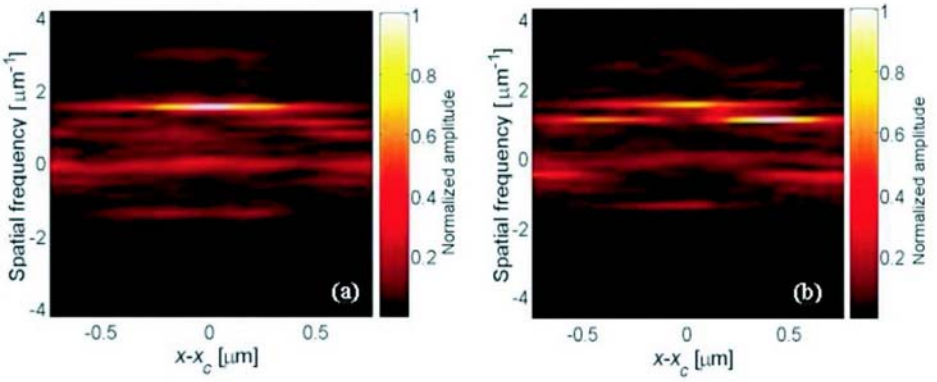

Figure 6: Spectral content of the optical field propagating in the z-direction when the guided optical field is excited in the W1 PhC waveguide at optical frequencies corresponding to (a) the dominant even mode at a wavelength of 1556.6 nm, and (b) superposition of even and odd modes at a wavelength of 1558.2 nm.

Fig.6a shows that for excitation of the guided mode at a wavelength of 1556.6 nm there is one dominant peak located in the center of the waveguide along the x-axis. For the longer wavelength of 1558.2 nm (Fig.6b), we still observe this peak, but also two additional peaks (centered at positive and negative x-coordinates) appear at a slightly lower spatial frequency. This result implies the propagation of two modes. By observing Fig.2, it is reasonable to believe that these two modes are e1 and e_2. Indeed, this expectation is confirmed in section IVc. Moreover, by integrating these 1D Fourier transform results along the transverse direction (i.e. along the x-axis) we obtain the average modal power content of the guided optical fields, shown in Fig.7. For wavelength 1556.6 nm, Fig.7a shows a single dominant peak indicating predominantly single-mode propagation in the W1 PhC waveguide. This peak corresponds to an effective wavelength of $\lambda_{eff}^{(1)} \approx 0.67$ with a corresponding effective refractive index of $n_{eff}^{(1)} \approx 2.34$. Note also that there is a smaller peak at the symmetric position on the negative side of the spectrum, which corresponds to the equivalent counter-propagating (i.e. reflected) mode. In contrast to commonly used NSOM intensity measurements, where forward propagating and backward propagating modes cannot be distinguished, the complex amplitude measurements permit the determination of not only the spatial frequency of the modes, but also their direction of propagation. For wavelength 1558.2 nm, Fig.7b shows two dominant peaks on the positive side of the spectrum indicating the existence of two forward propagating modes in the W1 PhC waveguide. These peaks correspond to modes with effective wavelengths of $\lambda_{eff}^{(1)} \approx 0.67$ and $\lambda_{eff}^{(2)} \approx 0.93$, having effective refractive indices of $n_{eff}^{(1)} \approx 2.34$

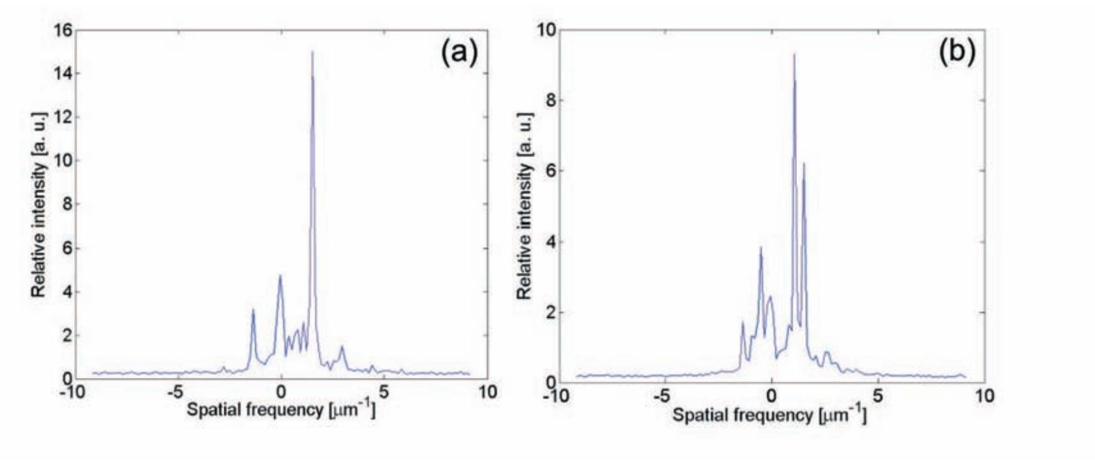

Figure 7: Spatial spectral content of the light propagating in the W1 PhC waveguide observed using H-NSOM: (a) λ=1556.6 nm; (b) λ=1558.2 nm.

and $n_{eff}^{(2)} \approx 1.68$, respectively. This result also clearly explains that the modal images shown in Fig.5 for this wavelength result from the superposition of two co-propagating modes with different propagation constants.

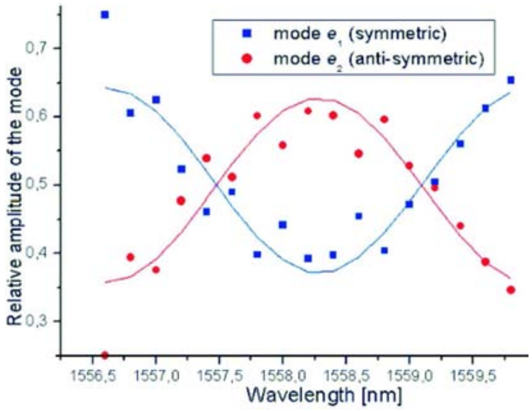

Figure 8: Fourier spectrum amplitudes vs. excitation wavelength for the two forward-propagating modes observed in the W1 PhC waveguide.

Finally, we perform a Fourier analysis for the NSOM measurements spanning the entire wavelength range shown in Fig.5 in order to obtain the amplitude of each of the above-mentioned modes as a function of wavelength. These results are summarized in Fig.8 and clearly indicate a gradual transition from single mode propagation towards dual mode propagation, and back to single mode propagation. Evidently, changing the wavelength can enhance or suppress the appearance of the second, anti-symmetric mode in a periodic fashion. Applying a sinusoidal curve fit to the obtained experimental results yields a wavelength offset of 1557.5 nm and a period of 3.3 nm.

A possible explanation for this periodic behavior is Fabry-Pérot interference of propagating and counter-propagating modes. However, the interference period corresponds to a cavity length of about 150 μm and we are unable to identify such a cavity in our device (the end facet of the waveguide is located further away from the PhC sample). Further investigation is required in order to fully understand the source of this periodic characteristic.

4.3 Comparison with theoretical modal analysis

Next we use the slope of the dispersion diagram in Fig.2 to estimate the theoretically predicted value of the propagation constants for the two expected modes. We find effective wavelength values of $\lambda_1 = 0.57$ μm and of $\lambda_2 = 0.7$ μm for the two modes relevant to our study (modes e_1 and e_2 respectively). The theoretically predicted effective wavelengths for the e_1 and e_2 modes are 15% and 25% lower than those measured in our experiments. We attribute these differences to fabrication inaccuracies and the dispersive nature of the modes. In particular, mode e_2 is highly dispersive (see Fig.2) and therefore any small variation in the fabrication conditions and/or environmental and material parameters may have a strong effect on the characteristics of this specific mode.

From our plane wave simulation results we learn that the first mode e_1 is symmetric (laterally even) and has a wave vector and field distribution not very different from the fundamental mode of a ridge waveguide (Fig.9a). The second mode e_2 is an anti-symmetric (laterally odd) mode and has strong dispersion (Fig.9b).

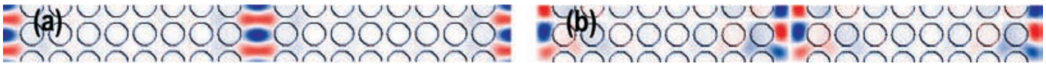

Figure 9: Plane wave expansion simulation showing mode patterns within the PhC waveguide. The modes were calculated using an approximate supercell-based model of the ideal structure. The two lowest-order eigenmodes are shown: (a) even mode e_1; (b) odd mode e_2.

To investigate how these two modes propagate within the PhC we performed a simulation using the finite-integral time domain method (CST Microwave Studio 5). The simulation results are shown in Fig.10. By controlling the source illumination profile we select the propagating modes within the W1 PhC waveguide. Fig.10a shows the propagation of the even mode, e_1. This simulation result is very similar to the experimental measurements results shown in Fig.5 for

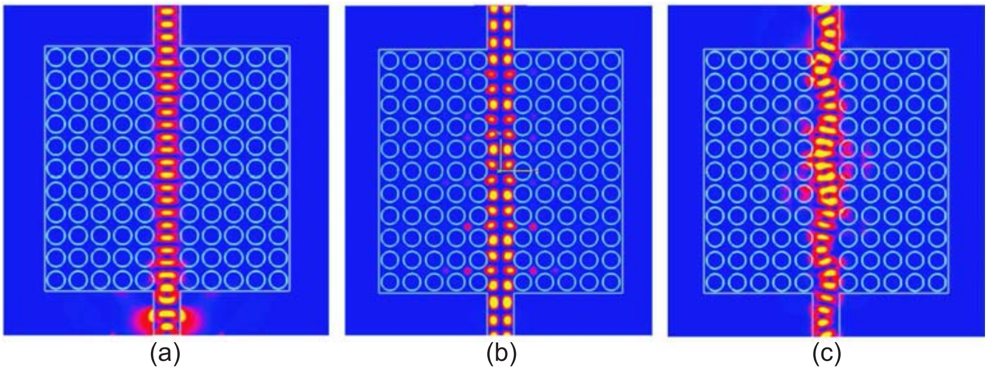

Figure 10: Finite integral time domain simulations showing the propagation of: (a) even mode, (b) odd mode and (c) superposition of the even and the odd mode.

wavelengths of 1556.6 nm and 1559.8 nm. Fig.10b shows the propagation of the odd mode and Fig.10c shows the superposition of the two modes. The "snake-like" pattern is due to the beating of the two modes having differing propagation constants. Qualitatively, the calculated field distribution is consistent with the measurements shown in Fig.5 (e.g., at a wavelength of 1559.40 nm).

5 Estimation of coupling loss

As a final example of the application of H-NSOM to investigate the detailed optical properties of the PhC waveguide, we estimate the input coupling loss of the device. Specifically, we perform a scan over a region that includes the boundary between the input ridge waveguide and the W1 PhC waveguide. Fig.11 shows a typical scan of the measured amplitude profile clearly demonstrating a significant drop in the field amplitude.

We calculate the coupling loss between the ridge waveguide and the W1 PhC waveguide by integrating the intensity in the transverse direction over the extent of the waveguide. Since the measured amplitude is not constant along the propagation direction, we estimate an average value of integration for each region. Fig.12 shows a typical variation of the intensity of the guided light along the propagation direction z. The two horizontal lines correspond to the averaged values of intensity for each of the two sections: the ridge and the W1 PhC waveguide. Although the reflection from the ridge to PhC waveguide junction has been shown to be small in far-field measurements [22], our Fourier analysis shows that the integrated intensity of the backward-propagating modes in the ridge waveguide is approximately 50–60% that of the forward-propagating modes, corresponding

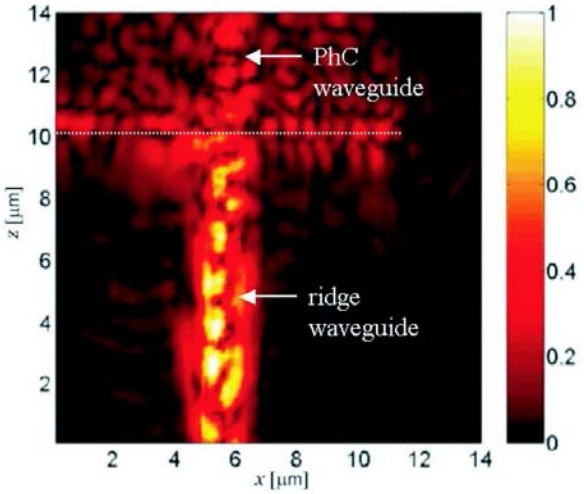

Figure 11: Near-field amplitude measurement in the area of the input coupling interface between the ridge and the W1 PhC waveguides for wavelength 1553.5 nm. The dotted line indicated the interface between the ridge waveguide (below the line) and the photonic crystal waveguide (above the line).

to roughly 2 dB of reflection loss. This result can be attributed to the input coupling method (a tapered fiber as opposed to the microscope objective used in [22]) possibly leading to the launching of higher order modes. The data in Fig.11 obtained for the wavelength of 1553.5 nm, shows a 7.1 dB drop of the intensity from the ridge to the W1 PhC waveguide. We believe that the additional loss is the result of out-of-plane radiation in the junction.

By performing such an analysis for measurements over a range of wavelengths, we obtain coupling loss dependence versus wavelength (see Fig.13). From the results of Fig.13 we observe that the coupling loss is also a periodic function of wavelength, with values of coupling loss varying between 2.7 dB to 7.1 dB and an average value of 4.8 dB. The period is approximately equal to the period observed in the analysis of the waveguide propagating modes (see Fig.5). The coupling loss can be fitted using a sinusoidal function with a period of 3.1 nm and wavelength offset of 1557.2 nm.

In general, in our measurements we find that the coupling loss is high when the ridge waveguide mode is mostly coupled to the symmetric PhC waveguide mode. This is somewhat counterintuitive, since we would expect the most efficient coupling to occur between the symmetric fundamental modes in the ridge and PhC waveguides. However, as seen in Fig.11, the light in the input ridge waveguide

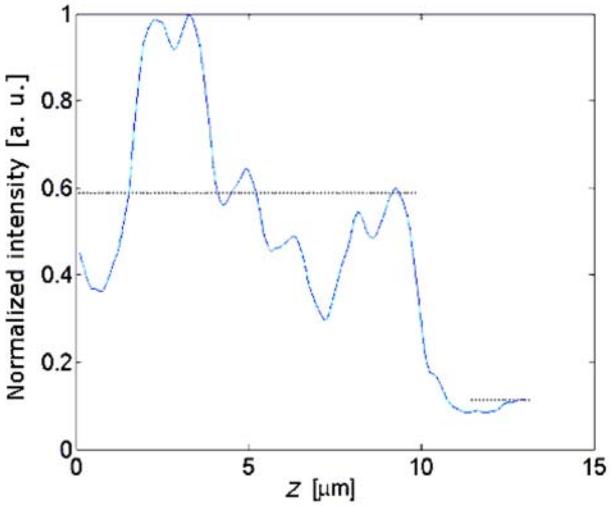

Figure 12: Aggregate intensity (integrated across the waveguide channel width) along the propagation direction for the distribution shown in Fig.11. The horizontal lines correspond to an average value of integrated intensity for the ridge waveguide (left) and the PhC waveguide (right).

does not appear to be predominantly in the fundamental mode. While not conclusive, this result indicates that the light injection from the tapered fiber into the ridge waveguide was most likely not optimal, and that the observed coupling behavior in our experiment will be more complex than the ideal case would suggest. In addition, the results presented in Fig.5 show that while the fundamental (even) mode seems to always be present in the waveguide, the second (odd) mode varies in strength as a function of the wavelength. Assuming there is no strong coupling between these two modes inside the PhC waveguide, since one mode is universally present and the second mode varies in amplitude, it is reasonable to expect that we should see the greatest transmission of energy through the waveguide when the second modes is at its apex and both modes are present. This expectation based on the observed mode characteristics inside the waveguide agrees with the observed characteristics at the input interface of the PhC waveguide. Once again, although there is insufficient information to draw a firm conclusion, these results reveal an agreement between near-field measurements made on differing areas of the PhC waveguide. Moreover, this comparison highlights the advantages of the H-NSOM technique for investigating the properties of nanoscale photonic devices, and demonstrates its potential for providing new and useful insight into these characteristics.

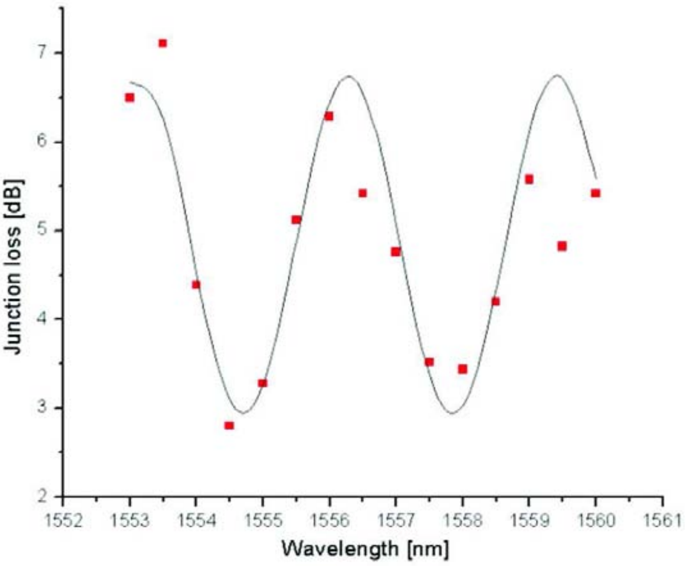

Figure 13: Experimentally obtained values for coupling loss at the coupling interface between the ridge and the W1 PhC waveguides for different input wavelengths.

6 Conclusions

We have analyzed the optical modes propagating in a Silicon-membrane photonic crystal waveguide, based on subwavelength-resolution amplitude and phase measurements of the optical fields using a heterodyne near-field scanning optical microscope (H-NSOM). Fourier analysis of the experimentally obtained optical amplitude and phase data allowed the identification of the propagating modes of the waveguide, including the direction of propagation (in contrast to intensity-only measurement techniques). This analysis revealed the presence of two superposed propagating modes in the waveguide. The propagation characteristics of these two modes were found to be in reasonable agreement with theoretical predictions within the limits of fabrication tolerances-the strongly dispersive waveguide modes mean that the exact propagation characteristics are extremely sensitive to a variety of parameters, including the material refractive index, membrane thickness, hole diameter and shape, and other fabrication defects. An analysis of the relative amplitudes of these two modes as a function of wavelength shows a periodic variation. Finally, by scanning the input region of the PhC waveguide, an estimation of the coupling efficiency between the ridge waveguide and the photonic crystal waveguide was made. The coupling efficiency was also found to have a periodic nature as a function of wavelength, with a period very close to the period measured for the internal propagating mode characteristics.

These results demonstrate that the characterization technique based on H-NSOM provides a wealth of information concerning the optical fields propagating in the device under study. In particular, the combination of the high-sensitivity amplitude and phase measurements, subwavelength resolution, and appropriate analytical and interpretive techniques permit the in-situ observation of the optical field properties with an unprecedented level of detail. Consequently, as nanostructure-based photonic devices and systems continue to grow in complexity and scale, the H-NSOM technique will likely prove to be an invaluable tool in observing the local optical fields in such devices, understanding the optical interactions between integrated components, and optimizing the performance of photonic systems based on this technology.

7 Acknowledgments

The authors would like to acknowledge M. Salt for the realization of the photonic crystal waveguide, and F. Schädelin, S. Gautsch, U. Staufer, and N. F. de Rooij (IMT, UniNE) for its fabrication. The authors also thank R. Rokitski and K. Tetz for their assistance in setting up and debugging the H-NSOM system. This research was supported in part by DARPA, National Science Foundation, AFOSR and the Swiss National Science Foundation.

References

[1] A. Lewis, M. Isaacson, A. Harootunian and A. Murray, “Development of a 500 Å spatial resolution light microscope : I. light is efficiently transmitted through $\lambda/16$ diameter apertures,” Ultramicroscopy **13**, 227–231 (1984).

[2] D.W. Pohl, W. Denk and M. Lanz, “Optical stethoscopy: Image recording with resolution l/20,” Appl. Phys. Lett. **44**, 651–653 (1984).

[3] M. L. M. Balistreri H. Gersen, J. P. Korterik, L. Kuipers, N. F. van Hulst, “Tracking femtosecond laser pulses in space and time,” Science **294**, 1080–1082 (2001).

[4] K. Okamoto, M. Loncar, T. Yoshie, A. Scherer, Y. Qiu, and P. Gogna, “Near-field scanning optical microscopy of photonic crystal nanocavities,” Appl. Phys. Lett. **82**, 1676–1678 (2003).

[5] P. Kramper, M. Kafesaki, C. M. Soukoulis, A. Birner, F. Muller, U. Gosele, R. B. Wehrspohn, J. Mlynek, and V. Sandoghdar, “Near-field visualization of light confinement in a photonic crystal microresonator,” Opt. Lett. **29**, 174–176 (2004).

[6] A. Bouhelier, M. R. Beversluis, and L. Novotny, “Near-field scattering of longitudinal fields,” Appl. Phys. Lett. **82**, 4596–4598 (2003).

[7] A. Bouhelier, M. R. Beversluis, and L. Novotny, “Characterization of nanoplasmonic structures by locally excited photoluminescence,” Appl. Phys. Lett. **83**, 5041–5043 (2003).

[8] S. Gotzinger, S. Demmerer, O. Benson, and V. Sandoghdar, “Mapping and manipulating whispering gallery modes of a microsphere resonator with a near-field probe,” J. Microscopy **202**, 117–121 (2000).

[9] I. Bozhevolnyi, V.S. Volkov, T. Søndergaard, A. Boltasseva, P.I. Borel and M. Kristensen, “Near-field imaging of light propagation in photonic crystal waveguides: Explicit role of Bloch harmonics,” Phys. Rev. B **66**, 235204 1–9 (2002).

[10] V.S. Volkov, I. Bozhevolnyi, P.I. Borel, L. H. Frandsen, and M. Kristensen, “Near-field characterization of low-loss photonic crystal waveguides,” Phys. Rev. B **72**, 035118 1–7 (2005).

[11] M. L. M. Balistreri, J. P. Korterik, L. Kuipers, and N. F. van Hulst, “Local observations of phase singularities in optical fields in waveguide structures,” Phys. Rev. Lett. **85**, 294–297 (2000).

[12] A. Nesci, R. Dändliker, and H. P. Herzig, "Quantitative amplitude and phase measurement by use of a heterodyne scanning near-field optical microscope," Opt. Lett. **26**, 208–210 (2001).

[13] S. I. Bozhevolnyi, and B. Vohnsen, "Near-field imaging of optical phase and its singularities," Opt. Comm. **212**, 217–223 (2002).

[14] R. Engelen, Tim Karle, Henkjan Gersen, Jeroen Korterik, Thomas Krauss, Laurens Kuipers, Niek van Hulst, "Local probing of Bloch mode dispersion in a photonic crystal waveguide," Optics Express, **13**, 4457–4464 (2005).

[15] E. Flück, M. Hammer, A.M. Otter, J. P. Korterik, L. Kuipers, and N. F. van Hulst, "Amplitude and phase evolution of optical fields inside periodic photonic structures," J. Lightwave Technol. **21**, 1384–1393 (2003).

[16] A. Nesci, and Y. Fainman, "Complex amplitude of an ultrashort pulse with femtosecond resolution in a waveguide using a coherent NSOM at 1550 nm," in Wave Optics and Photonic Devices for Optical Information Processing II, P. Ambs and F. R. Beyette, Jr., eds., Proc. SPIE **5181**, 62–69 (2003).

[17] J. C. Gates, C. W. J. Hillman, J. C. Baggett, K. Furusawa, T. M. Monro, and W. S. Brocklesby, "Structure and propagation of modes of large mode area holey fibers," Opt. Express **12**, 847–852 (2004).

[18] H. Gersen, T. J. Karle, R. J. P. Engelen, W. Bogaerts, J. P. Korterik, N. F. van Hulst, T. F. Krauss, and L. Kuipers, "Real-Space Observation of Ultraslow Light in Photonic Crystal Waveguides," Phys. Rev. Lett. **94**, 073903 1–4 (2005).

[19] H. Gersen, T. J. Karle, R. J. P. Engelen, W. Bogaerts, J. P. Korterik, N. F. van Hulst, T. F. Krauss, and L. Kuipers, "Direct Observation of Bloch Harmonics and Negative Phase Velocity in Photonic Crystal Waveguides," Phys. Rev. Lett. **94**, 123901 1–4 (2005).

[20] P. Tortora, M. Abashin, I. Märki, W. Nakagawa, L. Vaccaro, U. Levy, M. Salt, H. P. Herzig and Y. Fainman, "Observation of amplitude and phase in ridge and photonic crystal waveguides operating at 1.55 μm using heterodyne scanning near-field optical microscopy," Opt. Lett. **30**, 2885–2887 (2005).

[21] S. G. Johnson and J. D. Joannopoulos, "Block-iterative frequency-domain methods for Maxwell's equations in a planewave basis," Optics Express **8**, 173–190 (2001).

[22] I. Märki, M. Salt, R. Stanley, U. Staufer, H. P. Herzig, "Characterization of photonic crystal waveguides based on Fabry-Pérot interferenc," J. Appl. Phys. **96**, 6966–6969 (2004).

Optically tunable microcavity in a planar photonic crystal silicon waveguide buried in oxide

Iwan Märki, Martin Salt, and Hans Peter Herzig
University of Neuchâtel, Institute of Microtechnology,
Rue A.-L. Breguet 2, CH-2000 Neuchâtel, Switzerland

Ross Stanley
Centre Suisse d'Electronique et de Microtechnique (CSEM), SA,
Rue Jaquet-Droz 1,CH-2007 Neuchâtel, Switzerland

L. El Melhaoui, P. Lyan, and J. M. Fedeli
Laboratoire d'Electronique de Technologie de l'Information,
Commissariat à l'Energie Atomique (CEA)-Grenoble,
17 rue des Martyrs, 38 054 Grenoble Cedex 9, France

Abstract

We present all-optical tuning and switching of a microcavity inside a two-dimensional photonic crystal waveguide. The photonic crystal structure is fabricated in SOI using CMOS processing techniques based on deep ultraviolet lithography and is completely buried in a silicon dioxide cladding providing protection from the environment. By focusing a laser onto the microcavity region, both a thermal and a plasma dispersion effect are generated allowing tuning and fast modulation of the in-plane transmission. By means of the temporal characteristics of the in-plane transmission we experimentally identify the slower thermal and the very fast plasma dispersion effect with their modulation bandwidth being in the order of several 100 kHz and up to GHz, respectively.

OSICS codes: 230.1150, 230.5750.

The ability to control light propagation on a wavelength scale using silicon planar photonic crystal structures is well known. Planar photonic crystal waveguides, bends and microcavities are considered basic building blocks for applications such as microlasers, filters, multiplexers and optical switches [1–4]. It is possible to tune or switch photonic crystal devices in various ways such as temperature [5], refractive index change using liquid crystals [6], free charge carrier density [7] or non linear material effects [8]. Active photonic crystal devices allow further miniaturization of integrated optical circuits with active functionality. High-Q microcavities in planar photonic crystals exhibit highly localised fields and narrow transmission bands [9]. Even a small perturbation of the localized field can change the transmission properties of the microcavity. The relatively weak non linear properties of silicon can be used in these structures for low-power modulation and switching [10–12].

Until now most of the work done on tuning and modulating silicon photonic crystal devices has been based on an electrically controlled thermo optical effect. In this work, we present an optically tuneable microcavity inside a photonic crystal waveguide. We experimentally show that tuning the resonant wavelength and modulating the transmission signal is possible by using a laser focused onto the microcavity region, generating both thermal and plasma dispersion effects. As silicon membranes are delicate to the environment, our waveguide structures are fully buried in a silicon dioxide cladding being protected and more practical for many applications, notwithstanding the smaller refractive index contrast.

The design of the in-plane resonant cavity is shown in Fig. 1. The photonic crystal consists of a triangular array of cylindrical holes in a thin Si layer. The silicon slab is completely buried in a silicon dioxide cladding and therefore protected from the environment. The in-plane resonant cavity is formed by two identical one-dimensional Bragg reflectors inside the photonic crystal waveguide and has a length of about 330 nm. The cavity structure is designed so as to obtain a highly localized optical field inside the cavity and high in-plane transmission for a narrow frequency band. For fabrication reasons, we have kept the design as simple as possible while accepting lower performance for the cavity. Thus, the holes of the one-dimensional Bragg reflectors are all equally spaced and have the same dimensions. The designed photonic crystal microcavity structure is fabricated by LETI (Laboratoire d'Electronique de Technologie de l'Information, France) using deep ultraviolet lithography at a wavelength of 193 nm. After the lithography process, the patterns in the photoresist are transferred into the silicon layer of an SOI wafer using HBr dry etching technology via a silicon dioxide hard mask. As a final step, the etched structures in the silicon are then covered with an oxide layer.

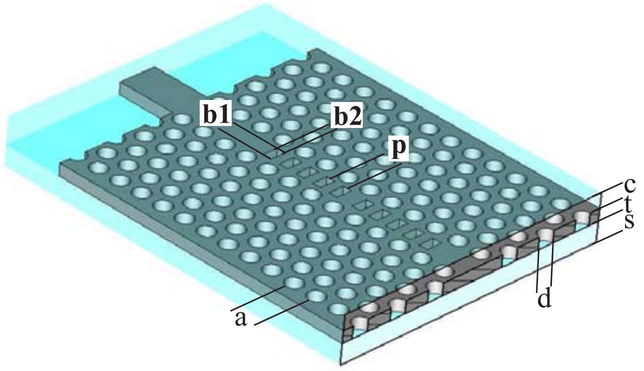

Figure 1: In-plane photonic crystal microcavity structure buried in silicon dioxide (PhC period a=490 nm, hole diameter d=350 nm, core thickness t=238 nm, bottom oxide thickness $s \approx 2000$ nm, upper cladding thickness $c \approx 700$ nm). The microcavity inside the photonic crystal waveguide is formed by two five-hole Bragg reflectors (hole dimensions $b1$=325 nm and $b2$=180 nm, period p=373 nm).

The transmission measurements are performed using a tunable laser source. By means of an aspheric lens, TE-polarized light (in-plane polarization) is injected into a 10 μm-wide silicon waveguide. The light is guided through a taper, which reduces the waveguide width to 0.5 μm, to the photonic crystal waveguide. For a narrow frequency band the light propagating in the photonic crystal waveguide couples into the resonant cavity, where it is highly localized and eventually transmitted. Using a second, identical taper the transmitted light is then guided to the exit of the device, where it is collected by a microscope objective and focused onto an InGaAs detector for measurements.

The measured transmission spectrum of the microcavity exhibits a resonance peak at a wavelength of 1.561 μm with an approximate maximum transmission efficiency of 11%. The quality factor is in the order of 200. Further transmission and loss properties of the microcavity have been discussed in Ref. [13].

At the transmission resonance the spectral frequency response of the microcavity is sensitive to the smallest perturbations of the region around the localized field. In order to induce a perturbation a laser with a wavelength of $\lambda = 532$ nm and a maximum power of 30 mW is focused onto the center of the microcavity. The light is strongly absorbed ($\sim$ 30%) by the Silicon core of the waveguide, whereas the upper and lower oxide cladding are transparent for the control laser wavelength. Figure 2 shows the measured transmission spectra through the microcavity without [curve (1)] and with [curve (3)] the control laser turned on. The raw measurement data have been numerically smoothed so as to remove the periodic Fabry-Pérot interference (compare with inset in Fig. 2), which is due to the reflection at the input and output waveguide end-facets. The resonant wavelength is red-shifted by 3 nm and the transmission is attenuated by approximately 10% due to thermo and plasma dispersion effects.

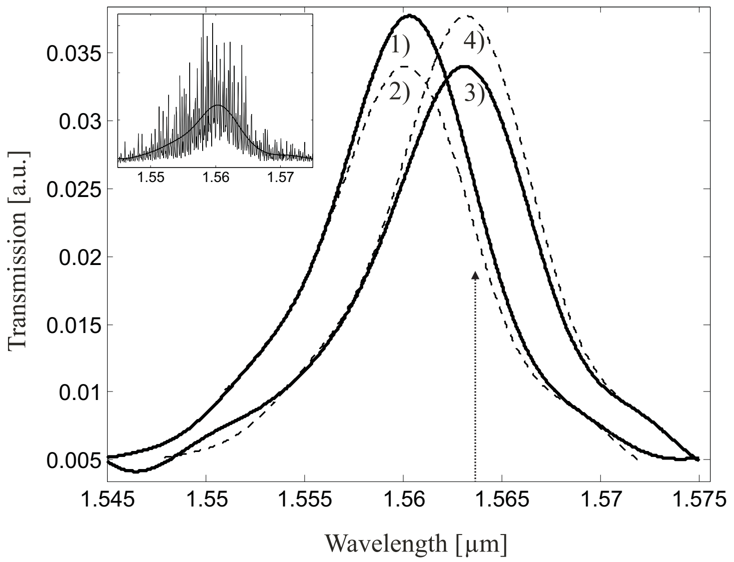

Figure 2: Measured transmission spectra through the photonic crystal microcavity without (1) and with (3) the control laser illumination (λ = 532 nm). The dotted curves (2) and (4) approximately indicate the change induced by the plasma dispersion and thermo optical effects, respectively. Arrow indicates the fixed wavelength for the temporal response measurements. The inset depicts the unfiltered transmission spectrum with the periodic Fabry-Pérot interference oscillations.

To distinguish the different physical effects we observe the temporal response of the transmission signal when applying a square modulation pulse of 12 μs to the control laser, shown in Fig. 3. A wavelength of $\lambda = 1.564$ μm slightly above the resonant wavelength (the peak wavelength of the thermally shifted transmission spectrum, see Fig. 2) was chosen for the transmitted light in order to conveniently observe both the thermo and plasma dispersion effects in the modulated transmission signal. The switching time of the control laser is in the order of a 100 ns. Coinciding with the switching-on of the control laser, we observe a small negative peak (position (2) in Fig. 3), which is due to the fast plasma dispersion effect inducing a small negative index change and an increase in the absorption coefficient. Following, the transmission efficiency increases with a rise time of about 5 ms as a result of the slower thermo optical effect (position (3)), which induces a positive index change shifting the resonant wavelength towards the wavelength of the transmission signal. At the switching-off of the probing laser a small positive peak is observed (position (4)) which is due to the recombination of the free carriers increasing slightly the refractive index and reducing the absorption coefficient. Sequentially, the transmission properties return to the initial state with thermal relaxation. For a better understanding of the present effects the consecutive change in the transmission properties can be indicated in Fig. 2 according to the observed temporal response. The arrow marks the fixed wavelength of l = 1.564 μm. The dotted curve (2) corresponding to the position (2) in Fig. 3 approximately indicates the change induced by the plasma dispersion effect alone where as the dotted curve (4) corresponding to the position (4) in Fig. 3 approximately indicates the change proper to the thermo optical effect.

From these measurements, the size of the thermo and plasma dispersion effects can be estimated. Three-dimensional simulations show that a change of Δn = +0.05 in the refractive index of the silicon layer gives the required redshift. For silicon, dn/dT is 1.86 $\pm 0.08 \times 10^{-4}$ /K at 1.55 μm [14] indicating a local temperature rise of 270 °C due to the thermo optical effect. The observed attenuation of approximately 10% is due to the presence of free carriers generated by the plasma dispersion effect. Assuming an approximate effective cavity length of Q$\times L_{cavity}$, the absorption coefficient is in the order of 15 cm^{-1}. Based on the Drude model [15], the induced charge density is estimated to be of ΔN$\approx 10^{18} cm^{-3}$ causing a refractive index change of about Δn = -0.0007, being more than one order of magnitude smaller than the thermo optically induced index change. This explains the observed redshift in the transmission spectrum.

Furthermore, from Fig. 3, we estimate the thermo optical maximum modulation frequency to be in the order of 200 kHz. Below this frequency a modulation depth of about 30% can be achieved (see Fig. 2). The plasma dispersion effect allows much greater modulation frequencies. We have measured the transmitted signal modulated at 50 MHz working above the thermal maximum modulation frequency. For the modulation of the control laser an electro optical resonant modulator was used, limiting the maximum modulation frequency to 50 MHz. In this case, the modulation depth is reduced to about 10% due to the weaker plasma dispersion effect and due to the diminished modulation depth of the control laser. A relaxation time for free carriers in a different light-confining structure on silicon has been measured to be in the order of 500 ps [11, 16]. Therefore, modulation frequencies in the GHz range should be possible.

A higher Q factor and transmission efficiency would allow a reduction in the power of the control laser and an increase in the maximum modulation frequency, improving the performance of the photonic crystal optical modulator. The differing temporal response of the thermal and plasma dispersion effects should allow in a limited range simultaneous tuning and high-speed modulation increasing the

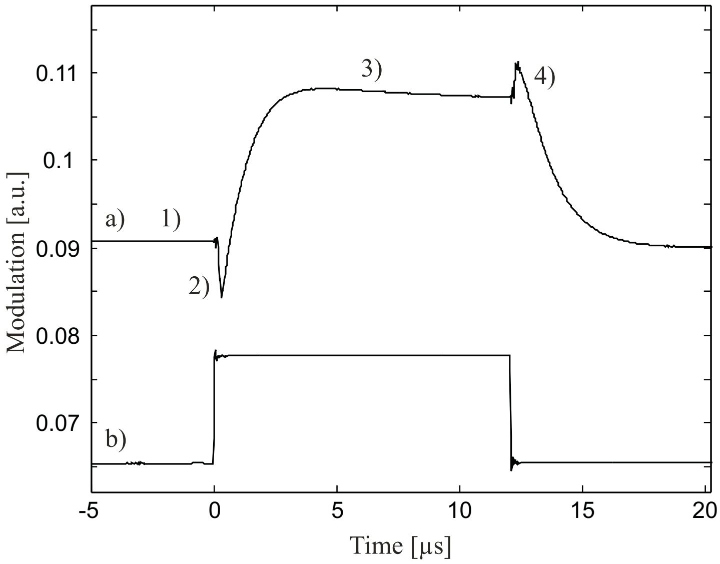

Figure 3: (a) Measured temporal response of the transmission signal with its switching characteristics (position (1) to (4)). The slight decrease of the signal in position (3) is most likely due to secondary thermal effects induced in the bulk silicon. (b) Square modulation pulse applied to the control laser.

functionality. Based on the plasma dispersion effect dense integration of several structures not suffering from the thermal cross-talk encountered in present-day integrated optical devices becomes possible. With current technology one could envision the integration of the control laser source onto the same chip, by stacking a wafer-based laser aligned with a wafer-based waveguide. Alternatively, the integration of the optical tuning and modulation method into a completely planar solution using a different wavelength for the control laser (slightly different to the wavelength of the transmission signal) could be realized with two intersecting resonant cavities. This configuration would enable modulation due to the free-carrier induced change of the refractive index based on two-photon absorption.

In conclusion, we have demonstrated that high-speed optical switching and resonant wavelength tuning on the sub-wavelength scale is achievable with a relatively simple technique. The induced thermal and plasma dispersion effects have been clearly identified by means of the temporal characteristics of the transmission signal. These results indicate that an improved design based on the presented device could serve as a basic component of high-speed all-optical integrated circuits based on silicon photonic crystal structures with applications in, for example, high bandwidth data routing.

References

[1] A. Mekis, J. C. Chen, I. Kurland, S. Fan, P. R. Villeneuve, J. D. Joannopoulos, “High Transmission through Sharp Bends in Photonic Crystal Waveguides,” Physical Review Letters **77**, 3787–3789 (1996).

[2] S. Noda, M. Imada, M. Okano, S. Ogawa, M. Mochizuki, and A. Chutinan, “Semiconductor three-dimensional and two-dimensional photonic crystals and devices,” Journal of Quantum Electronics **38**, 726–735 (2002).

[3] M. Loncar, T. Yoshie, A. Scherer, “Low threshold photonic crystal laser,” Applied Physics Letters **81**, 2680–2682 (2002).

[4] M. Notomi, A. Shinya, S. Mitsugi, E. Kuramochi, and H.-Y. Ryu, “Waveguides, resonators and their coupled elements in photonic crystal slabs,” Optics Express **12**, 1551–1561 (2004).

[5] E. A. Camargo, H. M. H. Chong and R. M. De La Rue, “2D Photonic crystal thermo-optic switch based on AlGaAs/GaAs epitaxial structure,” Optics Express **12**, 588–592 (2004).

[6] Ch. Schuller, F. Klopf, J. P. Reithmaier, M. Kamp, and A. Forchel, “Tunable photonic crystals fabricated in III-V semiconductor slab waveguides using infiltrated liquid crystals,” Applied Physics Letters **82**, 2767–2769 (2003).

[7] S. W. Leonard H. M. van Driel, J. Schilling and R. B. Wehrsporn, “Ultrafast band-edge tuning of a two-dimensional silicon photonic crystal via free-carrier injection,” Physical Review **B 66**, 161102 (2002).

[8] Locatelli, D. Modotto, D. Paloschi and C. De Angelis, “All optical switching in ultrashort photonic crystal couplers,” Optics Communications **237**, 97–102 (2004).

[9] Y. Akahane, T. Asano, B.-S. Song and S. Noda, “High-Q photonic nanocavity in a two-dimensional photonic crystal,” Nature **425**, 944–947 (2003).

[10] V. R. Almeida, C. A. Barrios, R. R. Panepucci and M. Lipson, “All-Optical control of light on a Silicon chip,” Nature **31**, 1081–1084 (2004).

[11] V. R. Almeida and M. Lipson, “Optical bistability on a Silicon chip,” Optics Letters **29**, 2387–2389 (2004).

[12] P. E. Barclay, K. Srinivasan and O. Painter, “Nonlinear response of silicon photonic crystal micresonators excited via an integrated waveguide and fiber taper,” Optics Express **13**, 801–820 (2005).

[13] I. Märki, M. Salt, H. P. Herzig, R. Stanley, L. E. Melhaoui, P. L. and JM. Fedeli, “Characterization of buried photonic crystal waveguides and microcavities fabricated by deep ultraviolet lithography,” Journal of Applied Physics **98**, 013103 (2005).

[14] G. Cocorullo and I. Rendina, “Thermo-optical modulation at 1.5 μm in silicon etalon,” Electronics Letters **28**, 83–85 (1992).

[15] R.A. Soref and B. R. Bennet, “Electrooptical effects in silicon,” IEEE Journal of Quantum Electronics **23**, 123–129 (1987).

[16] M. Lipson, “Overcoming the limitations of microelectronics using Si nanophotonics: solving the coupling, modulation and switching challenges,” Nanotechnology **15**, 622 (2004).

Tuning the resonance of a photonic crystal microcavity with an AFM probe

Iwan Märki, Martin Salt, and Hans Peter Herzig
University of Neuchâtel, Institute of Microtechnology,
Rue A.-L. Breguet 2, CH-2000 Neuchâtel, Switzerland

Abstract

We present theoretical and experimental results on switching and tuning of a two-dimensional photonic crystal resonant microcavity by means of a silicon AFM tip, probing the highly localized optical field in the vicinity of the cavity. On-off switching and modulation of the transmission signal in the kHz range is achieved by bringing an AFM tip onto the center of the microcavity, inducing a damping effect on the transmission resonance. Tuning of the resonant wavelength in the order of several nanometers becomes possible by inserting the AFM tip into one of the holes of the Bragg mirror forming the microcavity in the propagation direction.

OSICS codes: 250.5300, 230.3990, 230.5750.

1 Introduction

Photonic crystals are periodic structures with lattice dimensions of the order of the wavelength of light and they offer the ability to control light propagation on a wavelength scale [1–3]. One of the most promising realizations of photonic crystals is the well known two-dimensional planar photonic crystal slab, which confines the light by means of a photonic band gap in-plane and through index guiding in the vertical direction. These structures provide the possibility of creating miniaturized photonic components for integrated optical circuits [4–6]. An area of great interest in the process of realizing photonic integration is the use of photonic microcavities in two-dimensional photonic crystal waveguides for particular waveguide functions, such as small filters, microlasers, multiplexers, optical switches and high-resolution sensors [7–9]. Photonic microcavities can confine light in very small volumes ($\sim \lambda^3$) and exhibit high spectral resolution. Therefore, they could be key components for a variety of applications. The cavity Q factor per modal volume, Q/V, is one of the characteristic quantities that determine the strength of various interactions within the cavity. In recent years the optimization of such microcavities with increased factors has been the subject of intense research [10–12]. One of the difficulties associated with such photonic crystal cavity structures is to match their resonance frequency with those of interest in a given application. This is especially a concern since already small fabrication induced variations and irregularities cause a change in the optical properties of the cavity structure. The ability to tune or modulate the optical properties of such devices increases their functionality and opens up new possibilities for a variety of applications for integrated optics. In this paper, we present theoretical and first experimental results on tuning and switching the optical properties of a photonic crystal microcavity by means of a mechanical actuation method. A Silicon AFM tip is used to probe the localized optical field in the vicinity of the cavity achieving damping and tuning of the transmission resonance as theoretically predicted by A.F. Koenderink et al. in a similar configuration [13]. The theoretical and experimental results suggest a stand-alone MEMS solution to create a chip-based device with switching and tuning functionalities.

2 Design

The design geometry of the in-plane resonant cavity we have chosen is shown in Fig. 1. The photonic crystal consists of a triangular array of cylindrical holes (period 520 nm and hole radius 182 nm) in a thin Si layer (thickness 205 nm) for lateral light confinement. The in-plane resonant cavity is formed by two identical one-dimensional Bragg reflectors embedded in the photonic crystal waveguide and has a length of 400 nm (distance between the two Bragg reflectors) confining the light to an effective volume of approximately 200×500×500 nm at resonant wavelength. The design parameters of the Bragg reflectors (hole width 350 nm, hole length 150 nm, Bragg period 380 nm) are different to those of the rest of the photonic crystal. This increases the design options for the cavity and allows more efficient coupling into and out off the cavity than the surrounding triangular photonic crystal arrangement. The entire structure is surrounded by air and is thus a membrane.

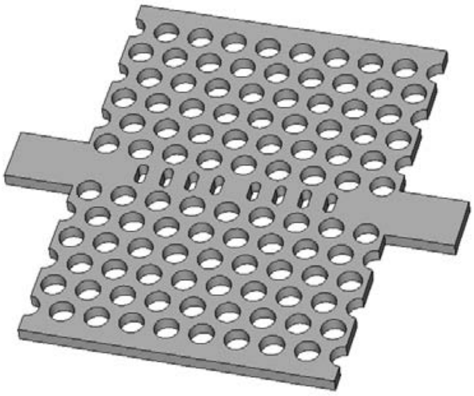

Figure 1: In-plane photonic crystal microcavity membrane consisting of a triangular array of cylindrical holes (period 520 nm and hole radius 182 nm) in a thin Si membrane layer (thickness 205 nm) surrounded by air.

The cavity structure is designed so as to obtain a highly localized field inside the cavity and high in-plane transmission for a narrow frequency band. In order to achieve a high Q factor and high in-plane transmission, the radiation losses (i.e. the modal mismatch at the interface between the photonic crystal waveguide and the cavity structure) need to be minimized by engineering the hole dimensions and positions of the Bragg reflectors during the design process. Several methods have been suggested for optimizing the performance of photonic crystal microcavities, including tapering, [14] Bloch-wave engineering [15] or radiation loss recycling [16]. All these methods require a very high accuracy and quality for the fabrication. For example, Noda et. al. have realized high-Q photonic crystal microcavities with Q factors up to 100,000 by optimizing the position of the air holes at both edges of the cavity [8]. Limited by the fabrication tolerances, we have kept our design as simple as possible while accepting lower performance for the cavity. Thus, the holes of the one-dimensional Bragg reflectors are all equally spaced and have the same dimensions (350 nm×150 nm).

The device has been fabricated in-house at the IMT-Samlab (University of Neuchâtel) using e-beam lithography [17]. The microcavity structure is written into a PMMA layer and then RIE and DRIE is used to transfer the structure from the PMMA layer into the Silicon. Lastly, buffered hydrofluoric acid vapour (BHF) etching removes the silicon dioxide layer underneath the Silicon slab forming a free-standing silicon membrane.

To measure the sample a butt-coupling setup was used. By means of a tapered fiber, TE-polarized light (in-plane polarization) from a tunable laser source (1440 nm to 1590 nm) is injected into a 10 μm-wide silicon layer (thickness t=205 nm). A lateral taper is used to reduce the waveguide width to the 0.5 μm width of the photonic crystal waveguide. For a narrow frequency band the light propagating in the photonic crystal waveguide couples into the resonant cavity, where it is highly localized and then transmitted. Using a second, identical taper the transmitted light is then guided to the exit of the device, where it is collected by a microscope objective and focused onto an InGaAs detector.

3 Passive transmission measurements

We have fabricated and measured several samples with the designed microcavities, exhibiting Q-factors between 300 and 750 for resonant wavelengths between 1.47 and 1.52 μm. In Fig. 2(a) we present one of the measured transmission spectra of the photonic crystal microcavity. For this sample, the measured transmission spectrum exhibits a resonance peak at the wavelength of 1.47 μm and a Q-factor of approximately 750. The dominant periodic Fabry-Pérot interference pattern contained within the measured spectrum corresponds to the total length of the waveguide system (approximately 2 mm) and is due to the Fresnel reflections at the smooth waveguide end-facets. Our three dimensional simulations have shown that about 38% of the light is reflected at the silicon/air interface of each end-facet.

The calculated transmission spectrum using a three dimensional finite integral time domain technique [18] is shown in Fig. 2(b). In the inset the field distribution at the transmission resonance peak illustrates the strong light confinement within the cavity. The measured Q-factor is about half of the predicted value by the calculation. Such differences are due to variations between the fabricated structure and the ideal simulated structure. Small defects, like variations in the hole dimensions or sidewall roughness, also induce higher losses, which cause a reduction in transmission and in the quality factor. Further improvements to the quality factor of the resonant cavity can be achieved by optimizing the design of the photonic crystal waveguide and the reflectors forming the microcavity.

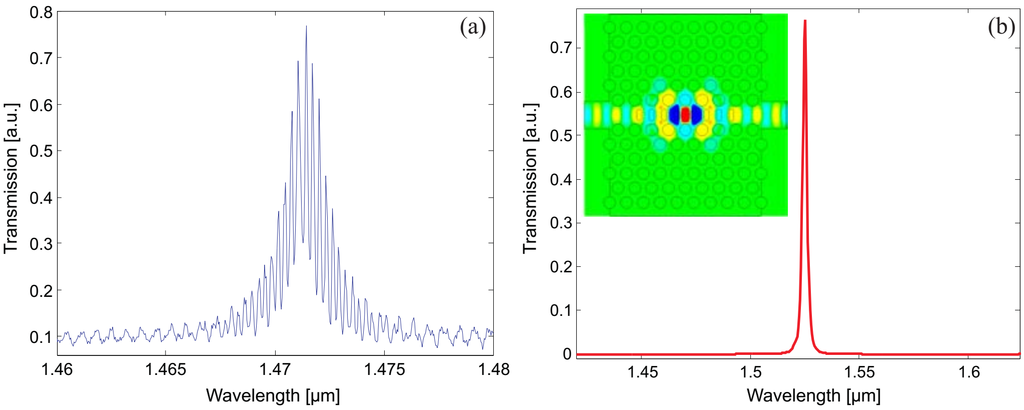

Figure 2: (a) Measured transmission spectrum of a photonic crystal cavity structure in a membrane surrounded by air with a Q factor of approximately 750. The characteristic Fabry-Pérot interference pattern at resonance is mainly due to end-facet reflections corresponding to a total waveguide length of 2 mm where as off resonance the interference pattern (2 times longer peak separation) is mainly due to end-facet to cavity reflections corresponding to an optical path of 1 mm (cavity structure is situated in the middle of the waveguide). (b) Calculated transmission spectrum of the ideal photonic crystal cavity structure with a Q factor in the order of 1500. The inset shows the calculated field distribution (magnetic field perpendicular to the photonic crystal membrane) at the resonance wavelength.

4 Tuning and switching

The highly localized field within the resonant microcavity is very sensitive to any perturbation. By a local change in the structure or the environment of the cavity one can influence the optical transmission properties. Ideally, such a change should be reversible so that we can realize an active, tunable device on a very small scale. Various ways to tune or switch photonic crystal devices have been demonstrated recently. One of the most common ways is temperature tuning induced by the temperature dependence of the refractive index of the material [19, 20]. However, with this method it is difficult to locally restrict the tuning effect on a chip. Both, theoretical [21] and experimental [22, 23] work has demonstrated the possibility of infiltrating photonic structures with liquid crystals and achieve the desired modulation by electromagnetically rotating the director field of the liquid crystal or thermally inducing a phase transition in the liquid crystal. Tunable spectral filtering of a planar photonic crystal has been demonstrated by means of a nanofluidic delivery structure using fluids with different refractive indices [24]. Electro-optical switching has been presented using a PN junction to inject free charge carriers and induce electro-absorption [25].

Further, all-optical switching has been demonstrated by different groups [26–29] with time responses varying from ms to fs depending on the mechanism and materials used. First results on mechanically tunable photonic crystal structures point out their great potential for multifunctional integrated optical devices [30–32]. One of the objectives of today's on-going research is to increase the tuning and switching performances and to achieve applicability for tuneable photonic crystal devices. Here, we present theoretical and experimental results on tuning and switching the optical properties of a photonic crystal microcavity based on the mechanical perturbation of the optical field.

Because the photonic crystal structure is a free-standing membrane, it allows direct access to the cavity and therefore direct mechanical intervention becomes possible. Our mechanical actuation method consists in bringing a silicon tip into the vicinity of the microcavity in order to induce a change in the optical environment. This can be achieved by introducing an AFM into the measurement setup and by probing the photonic crystal cavity region, as indicated in Fig. 3.

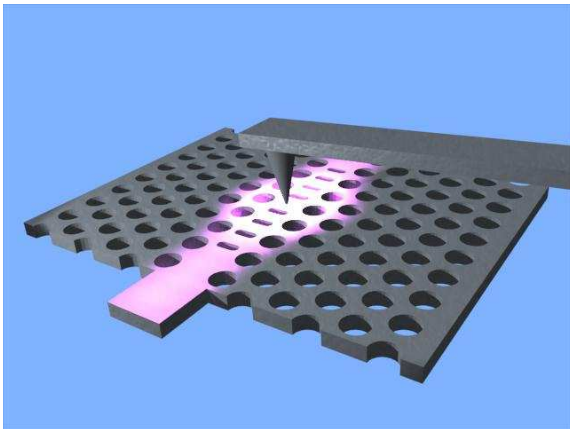

Figure 3: Silicon AFM tip positioned above the cavity center perturbing the confined optical field in order to induce on-off switching.

In a first configuration, we bring an AFM tip onto the center of the cavity perturbing the optical field. As shown in the field distribution at the resonance wavelength in Fig. 2, the optical field is highly localized in the center of the cavity and therefore very sensitive to any changes in the environment. In Fig. 4(a) we show the simulated changes in the in-plane transmission properties of the microcavity when approaching the silicon tip to the surface of the membrane (three tip-surface distances) using the 3-D finite integral time domain technique. The tip used in the simulation is shaped like a polygon based pyramid and has a tip radius of curvature of 30 nm. The simulations predict that the closer the Silicon tip to the surface of the photonic structure the stronger is the damping effect on the transmission efficiency. Virtually complete damping of the transmitted signal can be achieved when the tip is positioned on the surface of the membrane. Thus, by moving this small silicon tip over a distance as small as 500 nm, on-off switching becomes possible. In the inset of Fig. 4(a), the absolute value of the calculated field distribution illustrates how a part of the optical field confined within the cavity is coupled into the probing silicon tip inducing the observed damping in the transmission efficiency and reducing the Q factor of the cavity. Our simulations show that due to the presence of the probing tip approximately 15% of the light is coupled into the tip, approximately 35% is reflected back to the input waveguide and the rest is radiated to free space. The induced damping strength depends not only on the distance between the tip and the membrane surface but also on the tip size and on the exact lateral position of the tip in respect to the cavity structure and the strength of the optical field. A theoretical study addressing the effects of the lateral and vertical position of the tip in more detail has been presented by A. F. Koenderink et. al. [13].

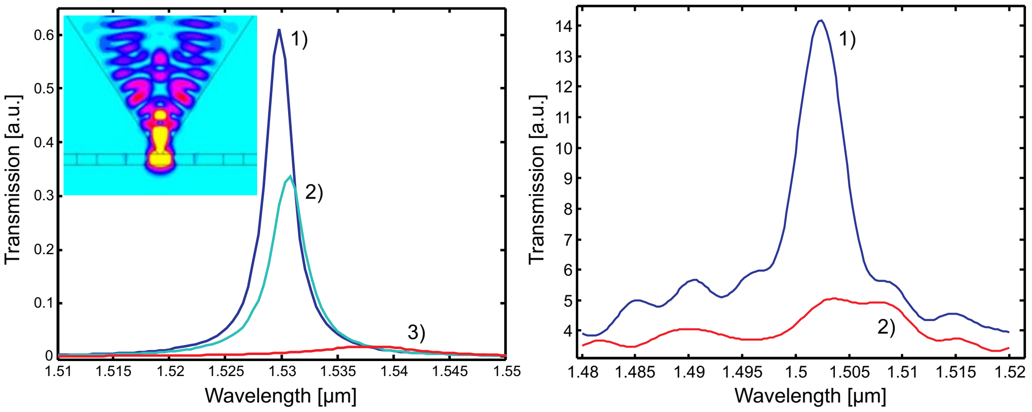

Figure 4: (a) Simulated changes in the transmission properties of a resonant microcavity structure when probing the center of the cavity by a silicon tip. The closer the silicon tip is to the surface of the membrane (tip-surface distance: 1) 500 nm, 2) 375 nm, 3) 0 nm) the stronger is the damping effect on the transmission efficiency. The inset shows the absolute value of the calculated field distribution in the x-y plane through the center of the resonant cavity with the probing AFM tip. (b) Measured changes in the transmission properties of resonant microcavity structure when probing the center of the cavity by a silicon tip. 1) Measured transmission spectrum without the probing AFM tip. 2) Measured transmission spectrum with the AFM tip positioned on the center of the cavity using the static force mode.

In Fig. 4(b) we show the experimental measurements using an AFM in the static force mode (contact mode) to probe the cavity center. Unlike the simulations, it was difficult to control the position of the AFM tip in an intermediate state limiting the experimental measurements to the two positions where the tip is not probing the cavity (curve (1)) and where the tip is in contact with the cavity surface (curve (2)). The tip used in the experiment is shaped like a polygon based pyramid with a half-cone angle in the order of 15° to 25° and has an initial tip radius of curvature of approximately 10 nm. By scanning the photonic crystal structure the surface is measured and the cavity center slowly approached reducing consecutively the scanning area. After positioning the tip onto the center of the microcavity, the tip radius of curvature is expected to be slightly increased due to abrasion (estimated increased radius of curvature ~30 nm). The raw measurement data have been numerically filtered so as to remove the periodic Fabry-Pérot interference. The damping effect that has been predicted by the three dimensional simulations can be observed in the measurements when positioning the AFM tip onto the center of the cavity. In addition, comparable to the simulations, the measurements show a similar reduction in the quality factor and a similar slight red-shift in the resonance wavelength induced by the AFM tip while damping the transmission efficiency.

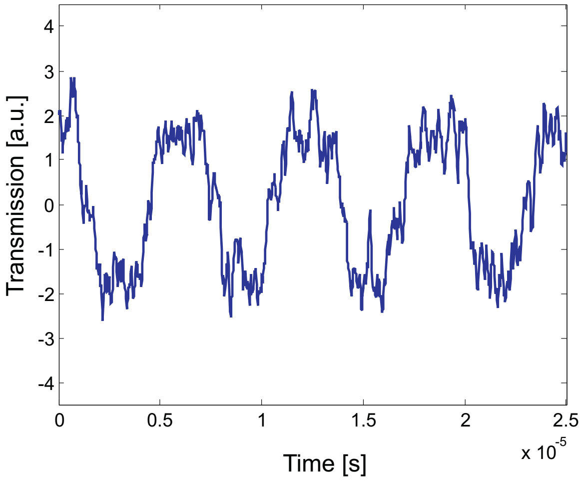

Figure 5: Measured transmitted signal modulated at ~180 kHz by the AFM tip in the dynamic mode with the corresponding resonance frequency of the cantilever. The observed parasitic, small amplitude oscillations are most probably due to mechanical vibrations perturbing the cantilever modulation.

When using the AFM in the dynamic force mode the cantilever with the AFM tip is vibrated near its resonance frequency with constant vibration amplitude, thus experiencing only intermittent contact with the surface. In consequence, when positioning the tip onto the center of the microcavity the damping effect is modulated and a modulation of the transmission signal is achieved. In Fig. 5, the modulated in-plane transmission signal with its frequency corresponding to the resonance frequency of the cantilever has been measured. In our case the resonance frequency is in the order of 180 kHz. The mechanically controlled modulation frequency of the optical signal depends on the resonance characteristics of the cantilever. For example, by reducing the geometry of the cantilever its resonance frequency can be increased and the optical signal could be modulated with higher speed, reaching the MHz regime.

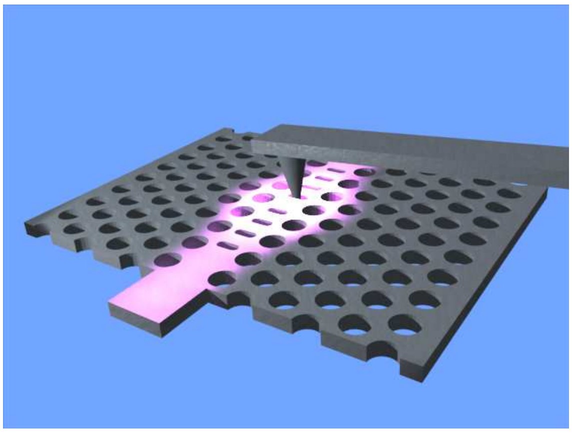

Figure 6: Silicon AFM tip inserted into one of the holes of the Bragg mirror forming the cavity in order to induce wavelength tuning.

In a second configuration, the AFM tip is inserted into one of the Bragg mirror holes at the edge of the cavity, as indicated in Fig. 6. In our simulations we observe that as the Silicon tip enters the air hole, the resonant wavelength of the microcavity is red-shifted without significantly lowering the quality factor and the transmission efficiency (see Fig. 7(a)). At maximum insertion the calculated transmission spectrum exhibits a red shift of over 10 nm. By inserting the silicon tip the optical field confined within the microcavity sees the hole in the silicon slab being filled with silicon, which changes the effective cavity length and reduces the Bragg mirror reflectivity, thus inducing the observed shift in the resonant wavelength. In the inset of Fig. 7(a), the absolute value of the calculated field distribution illustrates how the optical field is confined within the inserted silicon tip without inducing significant vertical loss. Contrary to the first configuration where the probing silicon tip above the center of the cavity induces vertical losses, the optical field mainly remains vertically confined within the silicon membrane. Thus, tuning of the cavity becomes possible. Analog to the probing of the cavity center, we achieve a significant change in the transmission properties with a very small mechanical movement of the probing silicon tip.

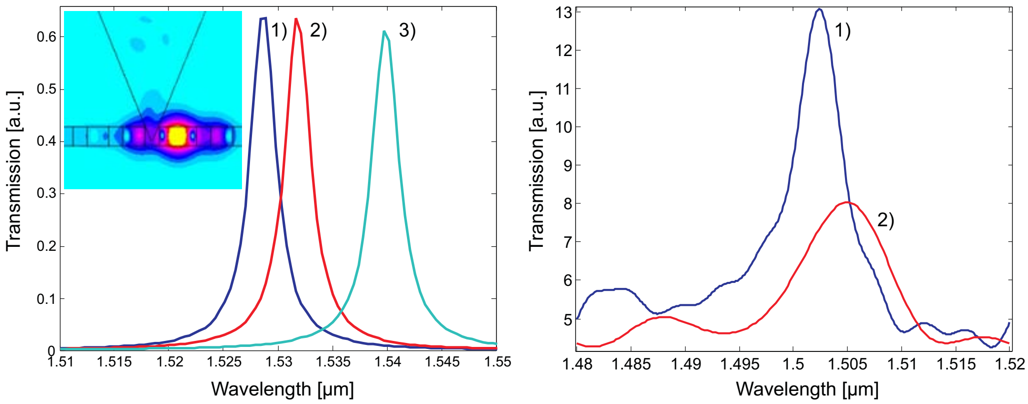

Figure 7: (a) Simulated changes in the transmission properties of a resonant microcavity structure when inserting a silicon tip into one of the Bragg mirror holes at the etch of the cavity. The tuning strength depends on the silicon tip position (tip - membrane surface distance: 1) 0 nm, 2) -100 nm and 3) -200 nm). The inset shows the absolute value of the calculated field distribution in the x-z plane through the center of the photonic crystal waveguide with the probing AFM tip. (b) Measured changes in the transmission properties of the resonant microcavity structure when inserting a silicon tip into one of the Bragg mirror holes. 1) Measured transmission spectrum without AFM tip. 2) Measured transmission spectrum with an AFM tip inserted into one of the Bragg mirror holes using the static force mode.

Figure 7(b) shows the measured transmission spectra for the two positions where the tip is not probing the hole (curve (1)) and where the tip is inserted into a hole (curve (2)) using the AFM in the static force mode. As predicted by the three dimensional simulations we observe a slight induced red-shift, which is of the order of 2.5 nm. However, contrary to the simulations the measurements present a lowered transmission efficiency and quality factor indicating the presence of scattering losses when the AFM tip is inserted into the air hole. Small variations between the experimental and the ideal simulated configuration can cause the observed differences in the transmission properties. For example, small defects in the fabricated structure, such as variations in the hole dimensions or sidewall roughness, can cause a different field distribution around the cavity, which may induce higher losses in the presence of the inserted AFM tip [13]. In addition, during the experiment it was difficult to determine how well the AFM tip was centered in respect to the air hole and how far the tip was inserted. The losses may also be increased due to mechanical stress in the silicon membrane induced by the probing AFM tip. Nevertheless, compared to the measurements of the first configuration the induced losses are significantly smaller, confirming the predicted tuning effect. In order to fully understand the observed results of the second configuration, we intend to carry out further tuning measurements using different types of AFM tips in the near future.

5 Conclusion

In conclusion, we have shown by simulations and first time measurements that a silicon AFM tip can be used to mechanically perturb the optical environment of a photonic crystal resonant microcavity in order to induce a change in its transmission properties. On-off switching is achieved by probing the center of the microcavity with the AFM tip, inducing vertical losses and a damping effect in the transmission efficiency. In the AFM's dynamic force mode the transmission signal has been modulated at a frequency of 180 kHz corresponding to the resonance frequency of the cantilever. By inserting the tip into one of the holes of the Bragg mirror forming the microcavity we have shown that resonant wavelength tuning becomes possible with limited losses. These results suggest a stand-alone MEMS solution to create a chip-based on-off switch or tunable filter. Furthermore, one could attempt to integrate more than one silicon tip to combine filter and tuning functionalities on one device. By separately controlling the position of the different tips a programmable integrated optical circuit with higher integration density and functionality could be achieved.

6 Acknowledgments

The authors would like to acknowledge S.Gautsch and U. Staufer for the fabrication of the samples by e-beam lithography in the labs of IMT-Samlab. We gratefully acknowledge R. Stanley from the Swiss Center of Electronics and Microtechnology (CSEM) for useful discussions. This work is funded under a joint projects program between the Swiss Center of Electronics and Microtechnology and the IMT-Uni Neuchâtel.

References

[1] E. Yablonovitch, “Photonic band-gap structures,” Journal of Optical Society of America **B 10**, 283–295, (1993).

[2] J. D. Joannopoulos, R. D. Maede, J. N. Winn, *Photonic Crystals*, Princeton University Press, Princeton, (1995).

[3] S. G. Johnson, S. Fan, P. R. Villeneuve, J. D. Joannopoulos, L. A. Kolodziejski, “Guided modes in photonic-crystal slabs,” Physical Review **B 60**, 5751–5780, (1999).

[4] A. Mekis, J. C. Chen, I. Kurland, S. Fan, P. R. Villeneuve, J. D. Joannopoulos, “High Transmission through Sharp Bends in Photonic Crystal Waveguides,” Physical Review Letters **77**, 3787–3789 (1996).

[5] M. Notomi, A. Shinya, S. Mitsugi, E. Kuramochi, and H.-Y. Ryu, “Waveguides, resonators and their coupled elements in photonic crystal slabs,” Optics Express **12**, 1551–1561 (2004).

[6] I. Märki, M. Salt and H. P. Herzig, “Practical and theoretical modal analysis of photonic crystal waveguides,” Journal of Applied Physics **95**, 7–11 (2004).

[7] S. Fan, P. R. Villeneuve, J. D. Joannopoulos, “Channel drop filters in photonic crystals,” Optics Express **3**, 4–11, (1998).

[8] S. Noda, A. Chutinan, M. Imada, “Trapping and emission of photons by a single defect in a photonic bandgap structure,” Nature **407**, 608–610, (2000).

[9] M. Loncar, T. Yoshie, A. Scherer, “Low threshold photonic crystal laser,” Applied Physics Letters **81**, 2680–2682 (2002).

[10] J. Vuckovic, M. Loncar, H. Mabuchi, A. Scherer, “Design of photonic crystal microcavities for cavity QED,” Physical Review **E 65**, 016608, (2001).

[11] K. Srinivasan, O. Painter, “Momentum space design of high-Q photonic crystal optical cavities,” Optics Express **10**, 670–684, (2002).

[12] Y. Akahane, T. Asano, B-S Song, S. Noda, “Fine-tuned high-Q photonic-crystal nanocavity,” Optics Express **13**, 1202–1214, (2005).

[13] A. F. Koenderink, M. Kafesaki, B. C. Buchler, V. Sandoghdar, “Controlling the Resonance of Photonic Crystal Microcavity by a Near-Field Probe,” Physical Review Letters **95**, 153904 (2005).

[14] Y. Akahane, T. Asano, B.-S. Song and S. Noda, "High-Q photonic nanocavity in a two-dimensional photonic crystal," Nature **425**, 944–947 (2003).

[15] Ph. Lalanne, Jean Paul Hugonin, "Bloch-wave enginieering for high Q's, small V's microcavities," IEEE Journal of Quantum Electronics **39**, 1430–1438 (2003).

[16] Ph. Lalanne, S. Mias, J. P. Hugonin, "Two physical mechanisms for boosting the quality factor to cavity volume ratio of photonic crystal microcavities," Optics Express **12**, 458–467 (2004).

[17] C. C. Cheng and A. Scherer, "Fabrication of photonic band-gap crystals," Journal of Vacuum and Science & Technology B **13**, 2696–2700 (1995).

[18] T. Weiland, "Time Domain Electromagnetic Field Computation with Finite Difference Methods," International Journal of Numerical Modelling **9**, 295–319 (1996).

[19] E. A. Camargo, H. M. H. Chong and R. M. De La Rue, "2D Photonic crystal thermo-optic switch based on AlGaAs/GaAs epitaxial structure," Optics Express **12**, 588–592 (2004).

[20] B. Wild, R. Ferrini, R. Houdré, M. Mulot, S. Anand, C. J. M. Smith, "Temperature tuning of the optical properties of planar photonic crystal microcavities," Applied Physics Letters **84**, 846–848, (2004).

[21] D. M. Pustai, A. Sharkawy, S. Shi, D. W. Prather, "Tunable photonic crystal microcavities," Applied Opitcs **41**, 5574–5579, (2002).

[22] Ch. Schuller, F. Klopf, J. P. Reithmaier, M. Kamp, and A. Forchel, "Tunable photonic crystals fabricated in III-V semiconductor slab waveguides using infiltrated liquid crystals," Applied Physics Letters **82**, 2767–2769 (2003).

[23] S. M. Weiss, H. Ouyang, J Zhang, Ph. M. Fauchet, "Electrical and thermal modulation of silicon photonic bandgap microcavities containing liquid crystals," Optics Express **13**, 1090–1097, (2005).

[24] D. Erickson, T. Rockwood, T. Emery, A. Scherer, D. Psaltis, "Nanofluidic tuning of photonic crystal circuits," Opt. Lett. **31**, 59–61, (2006).

[25] A. Sharkawy, S. Shi, D. W. Prather, "Electro-optical switching using coupled photonic crystal waveguides," Optics Express **10**, 1048–1059, (2002).

[26] S. W. Leonard H. M. van Driel, J. Schilling and R. B. Wehrsporn, “Ultrafast band-edge tuning of a two-dimensional silicon photonic crystal via free-carrier injection,” Physical Review **B 66**, 161102 (2002).

[27] F. Raineri, C. Cojocaru, R. Rai, P. Monnier, A. Levenson, C. Seassal, X. Letartre, P. Viktorovitch, “Tuning a two-dimensional photonic crystal resonance via optical carrier injection,” Optics Letters **30**, 64–66, (2005).

[28] P. E. Barclay, K. Srinivasan and O. Painter, “Nonlinear response of silicon photonic crystal micresonators excited via an integrated waveguide and fiber taper,” Optics Express **13**, 801–820 (2005).

[29] I. Märki, M. Salt, H. P. Herzig, R. Stanley, L. El Melhaoui, P. Lyan, J. M. Fedeli, “Optically tunable microcavity in a planar photonic crystal silicon waveguide buried in oxide,” Optics Letters **31**, 011604, (2006).

[30] W. Park, J.-B. Lee, “Mechanically tunable photonic crystal structure,” Applied Physics Letters **85**, 4845–4547, (2004).

[31] S. Iwamoto, S. Ishida, Y. Arakawa, M. Tokushima, A. Gomyo, H. Yamada, A. Higo, H. Toshiyoshi, H. Fujita, “Observation of micromechanically controlled tuning of photonic line-defect waveguide,” Applied Physics Letters **88**, 011104 (2006).

[32] T. Takahata, K. Hoshino, K. Matsumoto, I. Shimoyama, “Photonic crystal tuned by cantilever,” 18th IEEE International Conference on Micro Electro Mechanical Systems, Miami, Florida, USA, January 30 - February 3, 2005.

Measuring Optical Phase Singularities at Subwavelength Resolution

René Dändliker, Iwan Märki, Martin Salt, and Antonello Nesci*
Institute of Microtechnology, University of Neuchâtel,
Rue A.-L. Breguet 2, CH-2000 Neuchâtel, Switzerland

Abstract

We will present experimental and theoretical studies of optical fields with sub-wavelength structures, in particular phase singularities and coherent detection methods with nano-metric resolution. An electromagnetic field is characterized by an amplitude, a phase and a polarization state. Therefore, experimental studies require coherent detection methods, which allow to measure amplitude and phase of the optical field with sub-wavelength resolution. We will present two instruments, a heterodyne scanning probe microscope (heterodyne SNOM) and a high resolution interference microscope (HRIM). We will review some earlier work using the heterodyne SNOM, in particular the measurement of phase singularities produced by a 1 mm pitch grating with 10 nm spatial sampling. Using the HRIM we have investigated the intensity and phase distributions (with singularities) in the focal region of microlenses. The measurements are compared with the results calculated by rigorous diffraction theory.

DOI: 10.1088/1464-4258/6/5/009
Keywords: scanning optical probe microscopy, interference microscopy, subwave-length features, nano-optics, phase measurements, singularities, micro-lenses

---

*Present address: Nanophotonics and Metrology Laboratory, Swiss Federal Institute of Technology Lausanne (EPFL), CH-1015 Lausanne, Switzerland

1 Introduction

Optical fields are characterized by an amplitude, a phase and a polarization state. Coherent light diffracted by microstructures produces sub-wavelength features and can give birth to phase dislocations, also called phase singularities. Phase singularities are isolated points where the amplitude of the field is zero. In classical microscopy the objects are in general illuminated by incoherent light, and therefore only the intensity is measured. That is probably the reason why historically most investigations (including discussions on resolution, imaging properties, etc) are based on the intensity distribution. For phase measurements coherent illumination and interference of the object wave with a reference wave is needed, like in interference microscopy. In the neighbourhood of phase singularities the phase varies rapidly at a sub-wavelength scale. To investigate these phase variations and to localize the position of the phase singularities with high precision, we use two different instruments with sub-wavelength resolution: a heterodyne scanning probe microscope (heterodyne SNOM) [1] and a high resolution interference microscope (HRIM) [2].

In this paper we would like to give you a review of some earlier work with the heterodyne SNOM [3] and some new results obtained with the HRIM. We present measurements of phase singularities with 10 nm spatial sampling and compare them with theoretical results obtained from rigorous diffraction calculations. We made measurements of amplitude and phase with the heterodyne SNOM in the optical field diffracted by periodic microstructures, in particular a holographically recorded 1 μm pitch grating. We have also investigated the 3D intensity and phase distributions in the focal region of microlenses using the HRIM. The measurements are compared with the theoretical results obtained with a 2D model.

2 Heterodyne scanning probe microscope (heterodyne SNOM)

We have developed a coherent scanning near-field optical microscope (SNOM) with heterodyne detection for accurate phase measurements [1]. The concept of heterodyne interferometry is to introduce a small frequency shift Δf between two interfering beams. Due to this, the interference of the two beams produces an intensity modulation at the beat frequency $\Delta f = f_1 - f_2$, which is then detected. The set-up of the SNOM with heterodyne detection is shown in Fig. 1.

The laser is a 150 mW frequency doubled Nd:YAG diode-pumped solid-state laser ($\lambda = 532$ nm). After separation by a beam splitter (BS), the object and reference beams are shifted in frequency by two acousto-optic modulators (AOM),

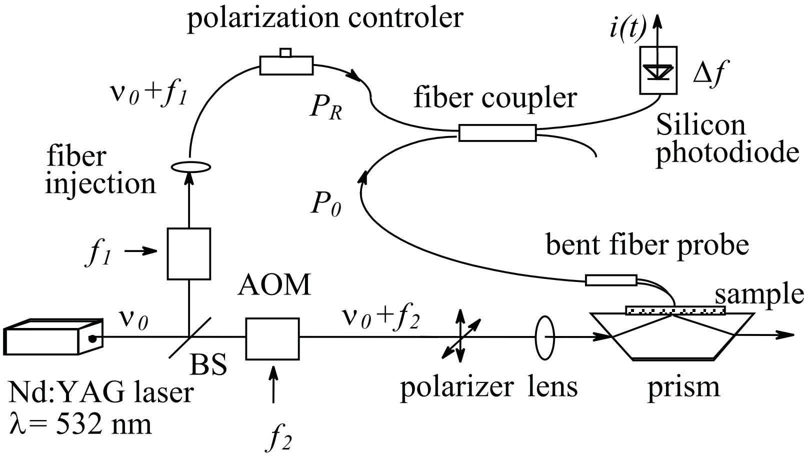

Figure 1: Heterodyne scanning probe microscope [1].

driven at $f_1 = 40.07$ MHz and $f_2 = 40.00$ MHz, respectively. By approaching a commercial AFM cantilever fibre probe close to the surface, the field is perturbed, resulting in propagation in the fibre. The reference and object beams are combined in the fibre coupler, producing the beat signal at 70 kHz, detected by a standard Silicon photodiode. A polarization controller is used to get maximum interference. During the measurement, the polarization is stable. Using synchronous detection of the heterodyne signal with a lock-in amplifier, we get two electronic output signals from which the amplitude and the phase of the optical field can be deduced. Besides the fact that coherent detection allows the optical field phase to be determined, we also get an increased dynamic range. This is because the amplitude of the electrical signal is proportional to the amplitude of the optical field, rather than to the intensity. In addition, we can always get shot-noise-limited detection, even with a photodiode, if PR is chosen to be sufficiently large to overcome the electronic noise.

The illumination system for the samples is shown in Fig. 2. The illumination system and the sample are mounted on an x-y-z piezo-electric translation stage (100 μm × 100 μm × 20 μm range), which allows accurate translation steps (2 nm resolution in z-direction). The fibre tip is mounted independently from this translation system. The bent tip is used as a conventional AFM (Atomic Force Microscope) cantilever and is brought close to the surface. Once the tip approach is done, the AFM feedback (contact mode) is switched off and the scan (in XY or XZ planes) is accomplished by the x-y-z stage. Most SNOM measurements are done at constant height (or constant intensity) in the X-Y plane (parallel to the surface) above the samples. However, the optical field diffracted by a structure

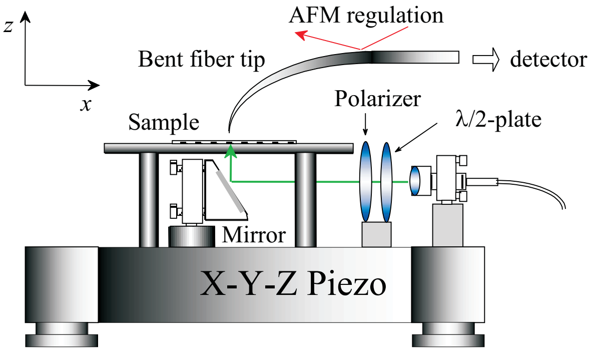

Figure 2: Experimental set-up for the illumination of the sample and the fibre tip probe [3].

depends strongly on the z-position, normal to the surface. Therefore, we have performed scans above the structures in the X-Z plane, perpendicular to the surface.

3 Phase singularities generated by a 1 μm grating

The sample is a 1 μm pitch quasi-binary shape grating of about 0.7 μm depth, holographically recorded in photo-resist. We use a dielectric fibre tip to collect the field information. The small coupling between the dielectric tip and the dielectric grating gives a negligible contribution to the total electric field. Using the set-up of Fig. 2, measurements of the TE-mode amplitude and phase in the X-Z plane have been performed. Results of the phase measurements are shown in Fig. 3 together with the theoretical phase distribution calculated with a Fourier Modal Method (FMM). The phases in Fig. 3 are represented by contour plots (iso-phase lines). The distance between two "bold" lines is λ (and thus corresponds to 2π). The measured phase distribution shown in the left Fig. 3 is a zoom into a larger field, which has been acquired by scanning in the x-direction at constant height with a step of $\Delta x = 25$ nm, starting at $z = 10$ μm and moving down in $\Delta z = 50$ nm steps for further x-line scans. The total scan size was $x = 5$ μm by $z = 10$ μm and the number of pixels is 200×200. With an integration time of 30 ms/pixel, the total image was acquired in 20 min. The circle indicates a phase singularity, an isolated point where the amplitude is zero and the phase is not determined [4]. Comparison with the theoretical calculations (right Fig. 3) shows a very good agreement, at least for the field measured more than 0.5 μm above the grating.

The evolution of the optical phase in time can be simulated by an additional linearly increasing phase of the reference wave. In Fig. 4 we present another

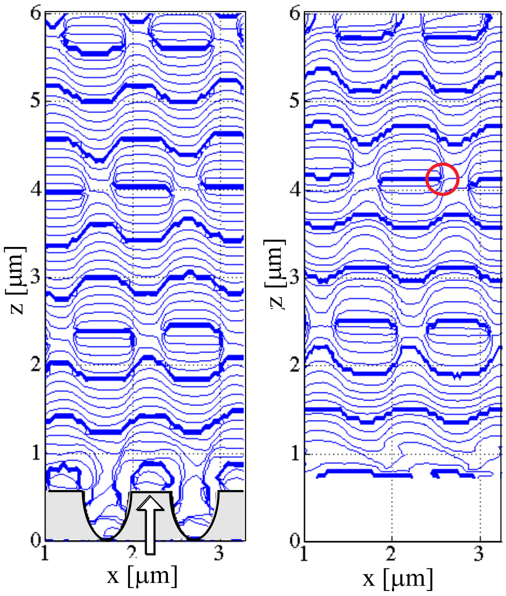

Figure 3: Left: calculated phase distribution with the Fourier Modal Method. Right: measured phase. The circle encloses one phase singularity [3].

measurement of the phase around two adjacent singularities using the following approach: the reference phase increases from left to right in steps of 90°. The spatial sampling of the measurements is 10 nm in the x-direction and 20 nm in the z-direction. We observe that the measured phase distribution changes its shape, but the phase singularities do not change their position. As the wave propagates in z-direction, the phase distribution turns around the two phase singularities in opposite direction, which means that they have opposite topological charge.

Figure 5 shows another measurement, but similar to a cross-section of Fig. 4 at $z = 1.18$ μm. By crossing the phase singularity, the amplitude makes a transition through zero (Fig. 5(a)) and the phase jump is always π (Fig. 5(b)). In this figure, we demonstrate that, at a phase singularity, the phase is not defined (because the signal vanishes in the noise) and the amplitude is really zero. In fact, we measured the zero amplitude, or more precisely, the zero optical power, down to $P_0 = 10^{-16}$ W (Fig. 5(a), with the marker “S”). The theoretical minimum detectable power at 50 Hz bandwidth is $P_{min} = 2.7 \times 10^{-17}$ W, limited by the shot noise. Thus the detected point is very close to the shot noise. The transition of the phase in Fig. 5(b) is measured within one step of ±10 nm. The measured phase jump is as sharp as one step (with a slope of $18^{o} nm^{-1}$).

From these measurements we see that although the amplitude falls practically down to zero at the singularity, the signal-to-noise ratio around the phase singularity (Fig. 5(b), markers A and B, separated by 20 nm) is sufficiently large

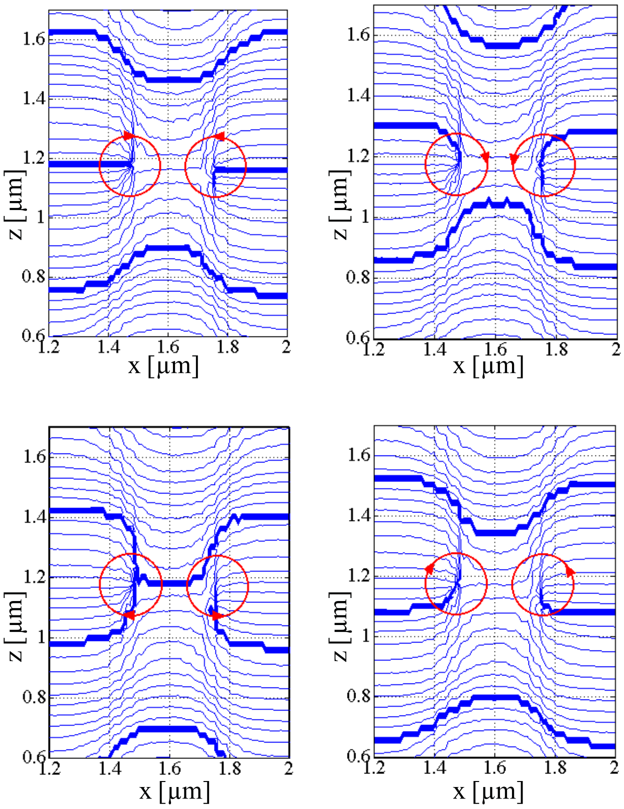

Figure 4: Phase measurement around two adjacent singularities separated by less than 300 nm. The scan step is 10 nm in x-direction and 20 nm in the z-direction. The additional reference phase increases from left to right in steps of 90°. The opposite sense of rotation indicates the opposite topological charge of the two singularities.

to locate the phase jump with high accuracy. In fact, in Fig. 5(b), the signal-to-noise ratios at the points A, S and B are $\mathrm{SNR_A}$= 26 dB, $\mathrm{SNR_S}$ = 6 dB and $\mathrm{SNR_B}$ = 21 dB, respectively, corresponding to the optical powers of $P_A = 10^{-14}$ W, $P_S = 10^{-16}$ W and $P_B = 3 \times 10^{-15}$ W. The resulting standard deviations for the phase measurement are $\delta\varphi_A = 3^{\circ}$, $\delta\varphi_S = 30^{\circ}$ and $\delta\varphi_B = 5^{\circ}$. Although the phase is not well measured at S, the transition is very well localized (within 10 to 20 nm) by the measurements at marks A and B in Fig. 5(b).

In previous papers we have also discussed the vectorial aspects of the electromagnetic field detection with fibre optical SNOM probes [3, 5]. We did observe some interesting polarization effects for the TM diffraction mode, which has an important longitudinal electric field component in this non-paraxial case, and our conclusion was that the longitudinal component of the electric field contributes nearly as much as the transverse component to the excitation of the propagating

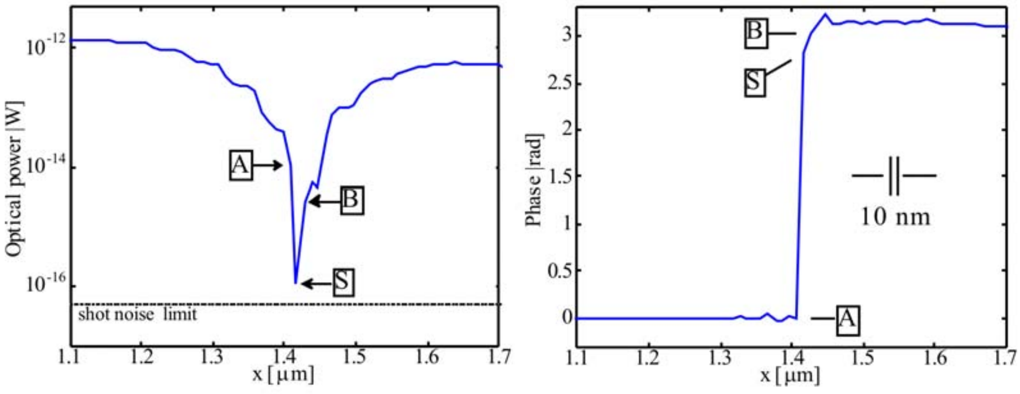

(a) (b)

Figure 5: Measured optical power and phase by crossing a phase singularity (S). The phase singularity is the special point where (a) the amplitude is zero, and (b) the phase jumps by π (with a quasi-infinite slope) [3].

mode in the fibre probe.

4 High resolution interference microscope

We have modified a classical interference microscope based on a Mach-Zehnder interferometer by adding a second magnification stage to obtain high spatial accuracy (see Fig. 6) [2]. The instrument is suitable for studying test structures in transmission. The typical overall magnification of the interference microscope is up to 1000, giving rise to a pixel size in the object field between 10 and 50 nm. The resolution of the far-field measurements is, of course, diffraction limited. The test structures are illuminated by a linearly polarized plane wave of wavelength λ = 488 nm. A piezo stage is used for precise z-positioning of the test element. 3D measurements are created via z-stepping of whole x-y areas, read consecutively using an area CCD. Thus, the different sections (x-y, x-z, y-z) can be observed by taking slices through the completed 3D data array. The phase information of the optical field is obtained by a classical 5 frames error-compensation algorithm [6]. By varying the phase difference between the two interfering beams in a known manner (phase shifts of $\pi/2$ introduced by PZT-mounted mirror) five intensity distributions are acquired and the original phase difference between the interfering beams can be calculated. The first studies in the field of high resolution interferometry were carried out by Tychinski [7]. He observed structures of the phase distribution inside a diffraction limited spot. Convincing explanations of the apparent superresolution phenomenon have been given only recently by Totzeck [8, 9]. With a high resolution interference microscope phase singularities can be observed [2]. Phase singularities can be observed in both the near- and far-field of optical microstructures. The phase jump at singularities is very sharp, which allows the determination of their position with sub-wavelength accuracy. However, since the electromagnetic field decreases to zero, the detected signal decreases in the vicinity of a singularity and the accurate location of two close singularities is therefore limited by the signal-to-noise ratio.

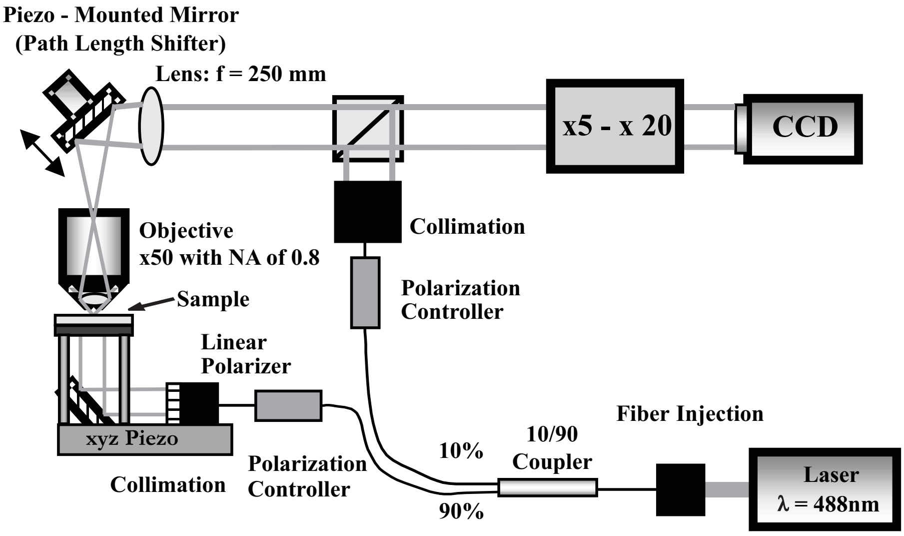

Figure 6: Schematic view of the high resolution interference microscope. Pixel size of CCD is about 10 μm.

5 Phase singularities in the focal region of microlenses

Micro optical elements play an important role in a large range of applications, notably in integrated optical systems. Today's technology allows the realization of a great variety of micro optical elements, and several simulation methods have been developed in order to model the interaction of light with such optical microstructures [10, 11]. The ability to image and compute the optical field of micro optical elements allows a better understanding of the optical phenomena that occur. In this article we discuss the simulation and measurement of the optical field in the focal region of a refractive microlens. Similar studies have already been presented [12–15], however, with limited experimental results. To the best of our knowledge, we present for the first time combined theoretical and three-dimensional experimental investigations. For this purpose, the Fourier modal method (FMM) based on rigorous diffraction theory [16] was applied and, by means of high resolution interference microscopy, the intensity and phase distribution of the optical field generated by a microlens was measured.

A common and well-known method for fabricating refractive microlenses is the resist melting technology or reflow technique [17]. This technology was used to fabricate the microlens arrays discussed in this paper. The presented investigations add more information about the behaviour of the optical field in the focal region of refractive microlenses with a diameter in the order of 30 μm and high numerical apertures (NA $\approx$ 0.4).

Based on a standard rigorous diffraction theory, we apply the rigorous eigenmode method (FMM) to the simulation of microlens arrays [16]. The rigorous eigenmode method is applicable to a wide range of periodic profiles but is limited by the dimensions and the period of the microstructure because of the increasing computational requirements. In order to observe the optical field in the focal region experimentally we analyse two-dimensional arrays of approximately hemispherical microlenses illuminated with a plane wave. For the simulation we perform two-dimensional calculations (transverse electric polarization). Three-dimensional calculations are not possible because of the computational requirements, which exceed by far the available capacities. For the two-dimensional calculations we use a periodic line of infinitely long cylindrical lenses [18] and we represent the lens surface as part of a perfect circle, which does not completely correspond to a real microlens fabricated by the resist melting technology, but is a good approximation for the studied microlenses. The precise form of a microlens, and hence its focal properties, is determined by the effects of surface tension, temperature, and the rate and manner of the temperature change during fabrication [19].

The presented microlenses have a diameter of $d = 30$ μm, a height of $h = 10$ μm and a focal length of $f \approx 35\mu$m (NA $\approx$ 0.4). The 2D array period is 33 μm. In Fig. 7(a) we present the measured intensity distribution. The lens is illuminated with a plane wave propagating in the z-direction (in the figure from top to bottom). The intensity distribution in the focal region is strongly modulated by diffraction due to the high numerical aperture. Comparing with the calculated intensity, shown in Fig. 7(b), and considering the differences between the 2D model and 3D lens, we observe a good correspondence in the diffraction pattern. However, we notice that the calculated intensity is stretched in the z-direction in comparison with the measured intensity. Further, in the calculated diffraction pattern we observe a dark region just above the focus, which is not

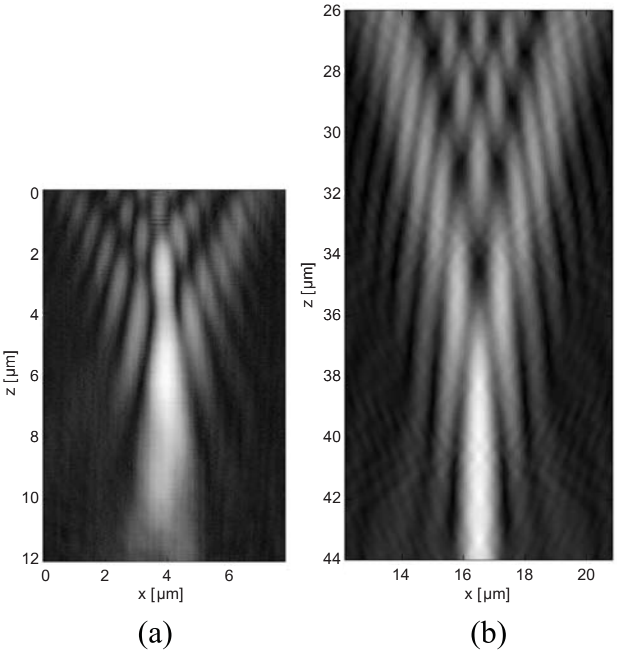

Figure 7: Intensity distribution in the focal region of a microlens ($d = 30$ μm, $f \approx 35\mu$m). (a) Measured with the HRIM ($\Delta z = 50$ nm: defined by the step size of the piezo stage, $\Delta x = 35$ nm: pixel size in the object field). The slight asymmetry may be due to a misalignment of the illumination. $z = 0$ indicates the starting plane of the measurements. Due to experimental limitations, the absolute distance between the starting plane and the lens is not known. (b) Calculated with the rigorous modal method (FMM). The z-axis represents the distance to the microlens.

present in the measurements. This may be due to the fact that the calculations generate a two-dimensional pattern whereas the measurements refer to a section of an axially symmetric 3D diffraction pattern [20]. Variations may also be caused by the difference between the shape of the real microlens and the shape of the simulated microlens. The diffraction contributions of the neighbouring lenses cannot be noticed because most of the energy is diffracted into lower orders [18].

The behaviour of the phase in the focal region of microlenses is illustrated in Fig. 8. The illumination of the microlens is again in the direction of the z-axis. The agreement between the measured (Fig. 8(a)) and the calculated (Fig. 8(b)) phase distribution allows good comparison, including the phase singularities (marked by circles). The noise in the measurements is due to the rapid changes of the intensity with position and the low intensities in regions outside the focus. There is also a contribution from relative movements caused by ex-

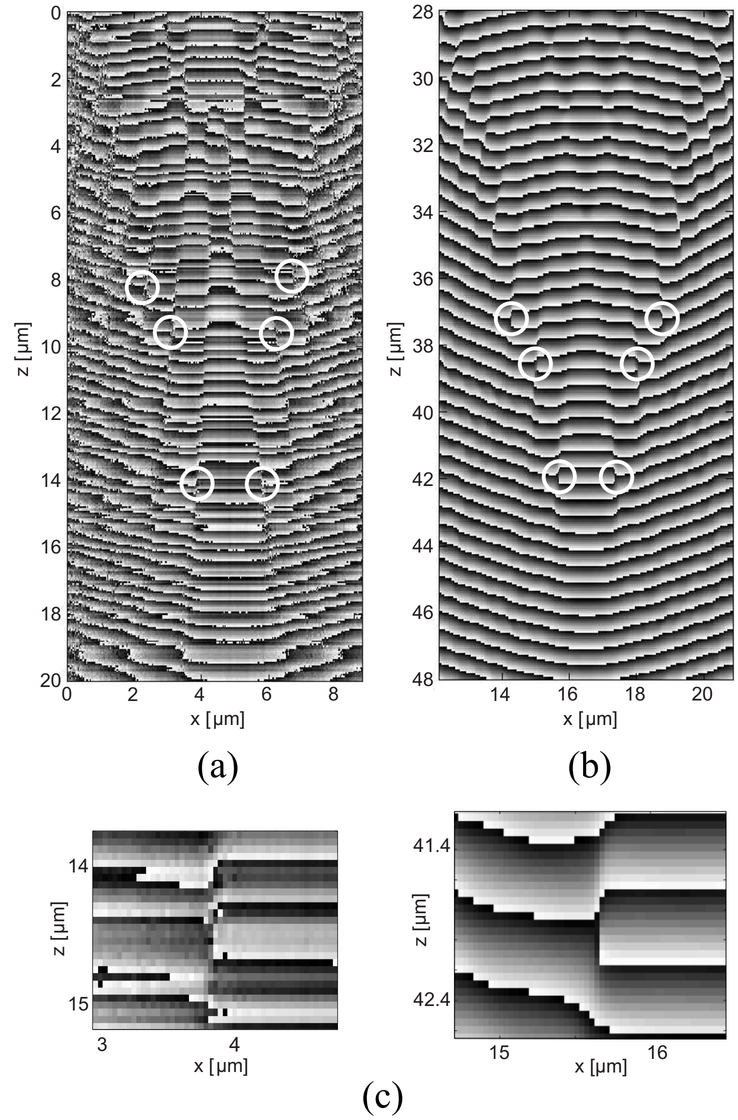

Figure 8: Phase distribution in the focal region of a microlens (d = 30 μm, f ≈35 mm). The grey scale range is between π (white) and $-\pi$ (black). (a) Measured with the HRIM (Δz = 50 nm : defined by the step size of the piezo stage, Δx = 35 nm: pixel size in the object field). $z = 0$ indicates the starting plane of the measurements. Due to experimental limitations, the absolute distance between the starting plane and the lens is not known. (b) Calculated with the rigorous modal method (FMM). The z-axis represents the distance to the microlens. (c) Enlargement of an encircled region containing one singularity (lower left singularity in 8(a) and ((b)).

ternal influences during the measurements. Approaching the focal region from the bottom towards the lens ($z \geq 15$ μm in the measured and $z \geq 43$ μm in the calculated phase distribution) the wavefronts are more smoothly curved than between the focus and the lens. In general, the closer to the microlens we get (going towards $z = 0$ μm), the more turbulent is the wavefront. Further, we observe that the wavefront changes the direction of its curvature starting at the centre of focus and growing progressively while approaching the microlens. This change of curvature direction starts at a specific point, which is situated between the first two phase singularities when approaching the focal region from the bottom. In a restricted region between these two singularities we can observe a planar wavefront. Additional singularities are encountered approaching further towards the microlens. They always occur in pairs in order to conserve the topology of the optical field [20].

One of the essential properties of a phase singularity in a two-dimensional section as presented in Fig. 8(c) is given by a phase change on a closed path around the singularity [20]:

$$\oint d\varphi = \pm 2\pi. \tag{1}$$

The total phase change of $\pm 2\pi$ remains unchanged if the closed path around the singularity is varied. By using the measurements, we calculate the phase on the path around the singularity. To prevent adjacent pixels from acquiring a difference in phase that exceeds p, phase unwrapping is used [21]. Fig. 9(a) and Fig. 9(b) show the unwrapped phase on two different paths around the measured singularity of Fig. 8(c) with the corresponding phase change of 2π. This property allows us to localize the singularity to within the region of 105 by 150 nm (Fig. 9(b)), which is less than the diffraction limit. To confirm the accuracy of locating the singularity, an additional curve (dashed line) is added to Fig. 9(b), showing the unwrapped phase on a closed path (laterally shifted by 105 nm) not enclosing the singularity. Fig. 9(c) shows the unwrapped phase on a path equivalent to the one in Fig. 9(a) around the singularity in the simulated field shown in Fig. 8(c). A good comparison between Fig. 9(a) and 9(c) can be drawn. Notwithstanding the present noise in the measured phase distribution due to low intensity in the vicinity of singularities, we are able to localize the phase singularity with sub-wavelength accuracy.

It is interesting to notice that the observed intensity diffraction pattern in Fig. 7 is most similar to the Pearcey pattern [20]. However, the measured and calculated phase distributions show a different behaviour inside the caustics. The Pearcey pattern presents pairs of singularities inside the caustics whereas we cannot observe such in the rigorously calculated intensity distribution. The measured phase distribution may contain singularities inside the caustics (for $z < 8$ μm),

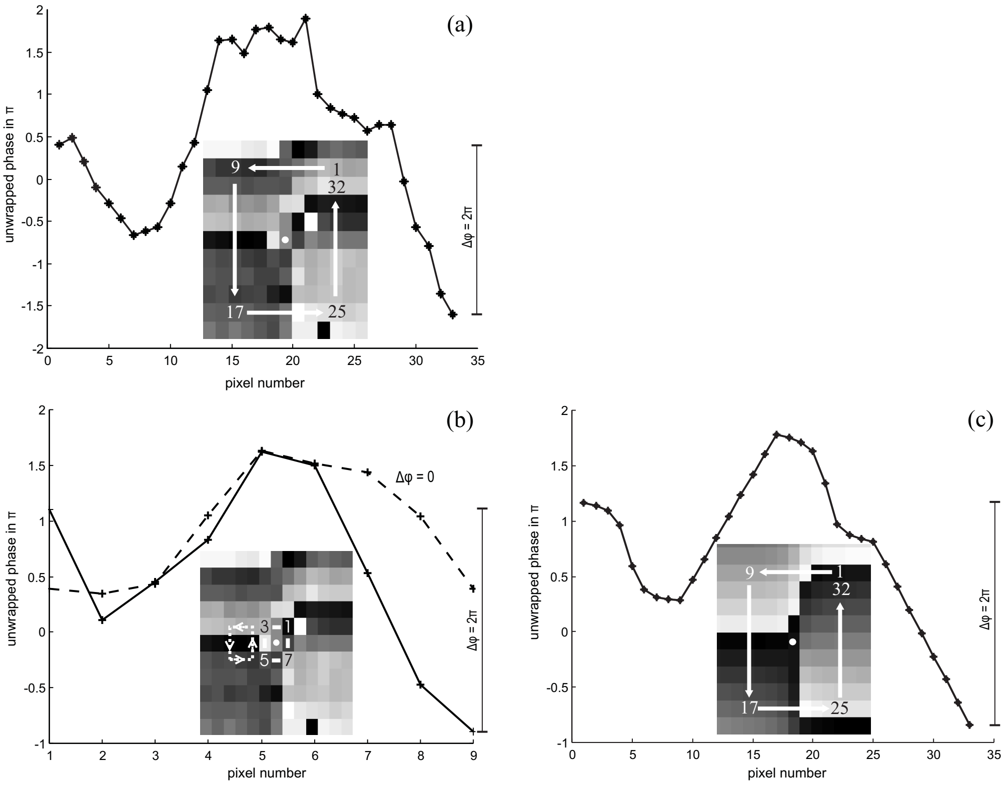

Figure 9: (a) Unwrapped phase on a closed path of 315 nm × 450 nm around the measured singularity shown in Fig. 8(c). (b) Unwrapped phase (solid line) on a closed path of 105 nm × 150 nm around the measured singularity shown in Fig. 8(c). On the same graph, the unwrapped phase (dashed line) of a laterally shifted (by 105 nm) contour not enclosing the singularity is included. In this case the phase change yields zero. (c) Unwrapped phase on a closed path of 315 nm × 450 nm around the singularity in the simulated field shown in Fig. 8(c). The insets show the path in the phase distribution. The values shown on the graph can vary by a multiple of 2π in comparison with the convention used in Fig. 8 due to the unwrapping of the phase.

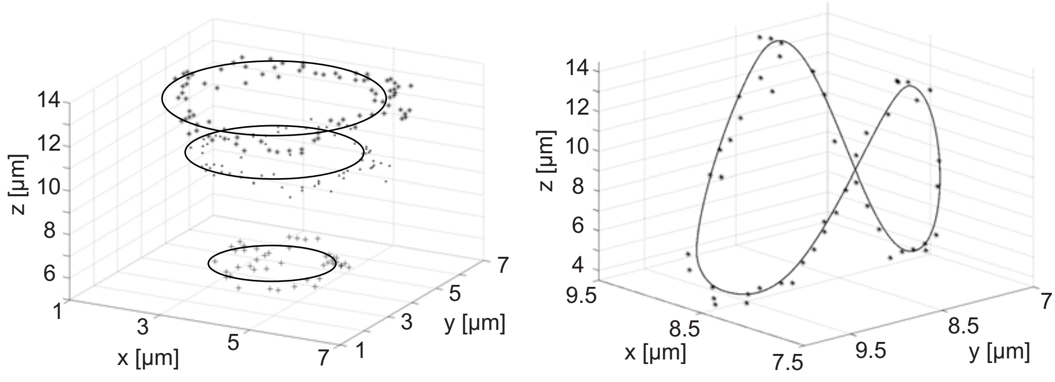

(a) (b)

Figure 10: (a) Singularity positions extracted from the 3D measurements for a microlens without astigmatism. (b) Singularity positions extracted from the 3D measurements for a microlens with astigmatic aberrations.

but they are not discernable with assurance due to the present noise. In addition, our calculations have shown that singularities inside the caustics are only present for lenses of significantly greater size than the ones studied in this paper. This finding is in accordance with recently published investigations by Nye [23].

Next, we investigated the measured phase singularities in three-dimensional space. In general, dislocations are curved lines in space. By scanning through the 3D measurements the positions of different pairs of singularity have been extracted. Enough singularity positions have been extracted in order to indicate the form of the dislocation lines. The phase singularities are situated on different concentric circles (Fig. 10(a)) forming circle dislocations according the Airy pattern, and because they are perpendicular to the direction of propagation they are of pure edge type [20].

The fact that the measured dislocations are circles perpendicular to the direction of propagation indicates that the investigated microlens has no serious astigmatic aberrations. In the presence of astigmatism, the dislocation circles are distorted out of the plane perpendicular to the optical axis. An example of such a distorted dislocation from a different microlens is presented in Fig. 10(b). The extracted singularity points forming the dislocation line are no longer situated in a plane perpendicular to the direction of propagation. This observation indicates astigmatic aberration for the investigated microlens. By observing dislocation lines in the focal region, we get information about the quality of the focal properties, which are key attributes in applications of microlenses.

6 Conclusion

We have presented two different instruments for phase measurements of optical fields with sub-wavelength resolution: a heterodyne scanning probe microscope (heterodyne SNOM) and a high resolution interference microscope (HRIM). In particular, we have used them to determine the existence and properties of phase singularities. For both instruments we have demonstrated subwavelength resolution for the phase measurements with a spatial sampling of the order of 10 nm and a corresponding resolution for the position of the phase singularities. Using the heterodyne SNOM we were able to measure the phase around two adjacent phase singularities separated by less than 300 nm at a wavelength of $\lambda = 532$ nm. We have also verified that the phase turns around these two phase singularities in opposite direction, which means that they have opposite topological charge, as expected by theory. By means of high resolution interference microscopy (HIRM) we have been able to image the intensity and the phase distribution in the focal region of microlenses. There is a good qualitative agreement between the measured optical intensity and phase distribution and the results of rigorous diffraction theory applied to a two-dimensional model. We have been able to observe the predicted phase singularities in the measurements. They are situated in the focal region and define characteristic points where the wavefront curvature changes its direction. Closer three-dimensional investigations of the phase distribution in the focal region show that phase singularities form closed lines in space in order to conserve the optical field topology. It confirms the presence of dislocation rings corresponding to the Airy ring in a focal pattern. The measurements for an astigmatic microlens show that the dislocation line is distorted along the optical axis indicating the aberrations of this focusing microlens. Comparing the two instruments, there is a significant difference concerning the vectorial aspect of the detected electric field: in the case of the high resolution interference microscope (HIRM) the non-paraxial field (large numerical aperture) produced by a microscopic object is transformed into a paraxial field at the observation plane of the microscope, therefore the electric field has only transverse components and the detected polarisation is selected by the polarisation of the reference wave, whereas the heterodyne SNOM probes directly the non-paraxial field with transverse and longitudinal components of the electric field vector [22]. In this latter case, the detected signal depends on the field conversion (vectorial transfer function of the tip) and the propagating mode in the fibre probe.

References

[1] A. Nesci, R. Dändliker, H. P. Herzig, "Measuring amplitude and phase distribution of fields generated by gratings with sub-wavelength resolution," Opt. Lett. **26**, 208–210 (2001).

[2] R. Dändliker, P. Blattner, C. Rockstuhl, H.P. Herzig, "Phase singularities generated by optical microstructures: Theory and experimental results," Proc. SPIE Vol. **4403**, 257–261 (2001).

[3] A. Nesci, R. Dändliker, M. Salt, H.P. Herzig, "Measuring amplitude and phase distribution of fields generated by gratings with sub-wavelength resolution," Opt. Commun. **205**, 229–238 (2002).

[4] J. F. Nye and M. V. Berry, "Dislocations in wave trains," Proc. Roy. Soc. Lond. **A336**, 165–190 (1974).

[5] L. Vaccaro, A. Nesci, R. Dändliker, H.P. Herzig, "Heterodyne scanning near-field optical microscope," Proc. SPIE Vol. **4829**, 637–638 (2002).

[6] P. Hariharan, B.F. Oreb, T. Eiju, "Digital phase-shifting interferometry: a simple error-compensating phase calculation algorithm," Appl. Opt. **26**, 2504 (1987).

[7] V.P. Tychinski, "On superresolution of phase objects," Opt. Commun. **74**, 41–45 (1989).

[8] M. Totzeck and H.J. Tiziani, "Interference microscopy of sub-lambda structures: A rigorous computation method and measurements," Opt. Commun. **136**, 61–74 (1995).

[9] M. Totzeck and H.J. Tiziani, "Phase singularities in 2D diffraction fields and interference microscopy," Opt. Commun. **138**, 365–382 (1997).

[10] K.-H. Brenner and W. Singer, "Light propagation through microlenses: a new simulation method," Appl. Opt. **32**, 26 (1993).

[11] Wang and A. Prata, "Lenslet analysis by rigorous vector diffraction theory," J. Opt. Soc. Am. A **12**, 1161 (1995).

[12] J.N. Walford, K. A. Nugent, A. Roberts, and R. E. Scholten, "High-resolution phase imaging of phase singularities in the focal region of a lens," Opt. Lett. **27**, 5 (2002).

[13] G.P. Karman, M.W. Beijersbergen, A. van Duijl, and J.P. Woerdman, “Creation and annihilation of phase singularities in a focal field,” Opt. Lett. **22**, 19 (1997).

[14] J.F. Nye, “Diffraction by a small unstopped lens,” J. Mod. Opt. **38**, 743–754 (1991).

[15] G.P. Karman et al., “Airy pattern reorganization and subwavelength structure in a focus,” J. Opt. Soc. Am. A **15**, 884–899 (1998).

[16] J. Turunen, “Diffraction theory of microrelief gratings,” in *Micro optics,* H.P. Herzig, ed. (Taylor & Francis, Inc, Bristol, 1997), pp. 31–52.

[17] M.C. Hutley, “Refractive Lenslet Arrays,” in Micro optics, H.P. Herzig, ed. (Taylor & Francis, Inc, Bristol, 1997), pp. 127–152.

[18] P. Blatter, H.P. Herzig, “Rigorous diffraction theory applied to microlenses,” J. of modern Optics **45**, 1395–1403 (1998).

[19] A. Schilling, R. Merz, Ch. Ossman, H.P. Herzig, “Surface profiles of reflow microlenses under the influence of surface tension and gravity,” Opt. Eng. **39**, 2171–2176 (2000).

[20] J.F. Nye, *Natural focusing and fine structure of light, caustics and wave dislocations*, (Bristol: Inst. of Physics Publishing, London, UK) 1999.

[21] J.M. Huntley, “Noise immune phase unwrapping algorithm,” Appl. Opt. **28**, 3268–3270 (1989).

[22] J.F. Nye, J.V. Hajnal, “The wave structure of monochromatic electromagnetic radiation,” Proc. R. Soc. Lond. A **409**, 21–36 (1987).

[23] J.F. Nye, “Evolution from a Frauenhofer to a Pearcey diffraction pattern,” J. Opt. A: Pure Appl. Opt. **5**, 495–502 (2003).

Acknowledgements

I would like to express my gratitude to all the people and institutions that have been involved and have supported me in accomplishing the presented work during the last four years.

- First of all, I would like to thank my thesis director Professor Hans Peter Herzig for having given me the opportunity to undertake my PhD thesis in his group. With his open and pleasant way he created a stimulating working environment permitting the development and exploration of new ideas in our research.

- I would like to thank Prof. R. Dändliker for awaking in me the interest for modern optics by his fascinating way of teaching and for encouraging me to start my master thesis in the applied optics group in Neuchâtel, which eventually led to my PhD thesis. As well, I thank him for introducing me into the art of writing scientific papers by his detailed revision of my first paper.

- As my direct supervisor of my master thesis and PhD thesis Dr. Martin Salt introduced me into many aspects of micro- and nano-optics. I thank him for his constructive and encouraging discussions, for his many revisions of my publications and for his humorful way of looking at some less humorful matter.

- I thank the Swiss Center of Electronics and Microtechnology (CSEM) for funding this research project under a joint projects program with the IMT. In particular, I would like to thank Dr. Ross Stanley of CSEM for contributing with stimulating and fruitful ideas during the several meetings. In addition, I thank the Laboratoire d'Electronique de Technologie de l'Information (LETI) where some of our samples have been fabricated thanks to the collaboration with CSEM.

- I thank Prof. Nico F. de Rooij, Prof. Urs Staufer and Dr. Sebastian Gautsch of the Sensors, Actuators and Microsystems Laboratory (SAMLAB) for putting much effort into the fabrication of the photonic crystal samples. By assisting some of the weekly meetings I had the occasion to have an insight into the challenges of nano-fabrication.

- Many thanks to Olivier Scherler for his colorful humor, friendship and the numerous times of patiently assisting me in installing, running and optimizing simulations on the «Number Cruncher», one of the rare decent computers of the group.

- I thank Dr. Wataru Nakagawa for many constructive discussions and for his detailed revisions of some of my publications. I thank him for introducing me into the American world of science and for letting me and my family «taste» some of the American way of life through which he has become a good friend of ours.

- I thank Pierpasquale Tortora and the group of Prof. Yeshaiahu Fainman with Uriel Levy and Maxim Abish of the University of California in San Diego for their fruitful collaboration in the near-field characterization of the photonic crystal samples.

- I would like to thank Sylvain Jaquet and Patrick Ruffieux for their agreeable friendship and for their encouragements and perseverance in taking me to go swim on a weekly basis.

- Guido Niederer and Pierre-Yves Baroni are thanked for sharing the office with me and for the pleasant atmosphere.

- I would like to thank Dr. Toralf Scharf for sharing endless ideas, for motivating discussions and his humorful personality, which I could enjoy in its original German version.

- For the friendly and open environment I would like to thank all the members of the applied optics group and more generally of the Institute of Microtechnology.

- Finally, most importantly I thank my dear Family, my wife Noemi and my children, Moira and Ezra, for their patience, love, encouragements and support during all the last years.